VOLUME 35 NOVEMBER 1957 NUMBER 11

Canadian Journal of Physics

Editor: H. E. DUCKWORTH

Associate Editors:

L. G. ELLIOTT, *Atomic Energy of Canada, Ltd., Chalk River*
J. S. FOSTER, *McGill University*
G. HERZBERG, *National Research Council of Canada*
L. LEPRINCE-RINGUET, *Ecole Polytechnique, Paris*
B. W. SARGENT, *Queen's University*
G. M. VOLKOFF, *University of British Columbia*
W. H. WATSON, *University of Toronto*
G. A. WOONTON, *McGill University*

Published by THE NATIONAL RESEARCH COUNCIL
OTTAWA CANADA

CANADIAN JOURNAL OF PHYSICS

(*Formerly Section A, Canadian Journal of Research*)

Under the authority of the Chairman of the Committee of the Privy Council on Scientific and Industrial Research, the National Research Council issues THE CANADIAN JOURNAL OF PHYSICS and five other journals devoted to the publication, in English or French, of the results of original scientific research. Matters of general policy concerning these journals are the responsibility of a joint Editorial Board consisting of: members representing the National Research Council of Canada; the Editors of the Journals; and members representing the Royal Society of Canada and four other scientific societies.

EDITORIAL BOARD

Representatives of the National Research Council

R. B. Miller, *University of Alberta*
H. G. Thode, *McMaster University*
D. L. Thomson, *McGill University*
W. H. Watson (Chairman), *University of Toronto*

Editors of the Journals

D. L. Bailey, *University of Toronto*
T. W. M. Cameron, *Macdonald College*
H. E. Duckworth, *McMaster University*
K. A. C. Elliott, *Montreal Neurological Institute*
Léo Marion, *National Research Council*
R. G. E. Murray, *University of Western Ontario*

Representatives of Societies

D. L. Bailey, *University of Toronto*
Royal Society of Canada
T. W. M. Cameron, *Macdonald College*
Royal Society of Canada
H. E. Duckworth, *McMaster University*
Royal Society of Canada
Canadian Association of Physicists
K. A. C. Elliott, *Montreal Neurological Institute*
Canadian Physiological Society
R. G. E. Murray, *University of Western Ontario*
Canadian Society of Microbiologists
H. G. Thode, *McMaster University*
Chemical Institute of Canada
T. Thorvaldson, *University of Saskatchewan*
Royal Society of Canada

Ex officio

Léo Marion (Editor-in-Chief), *National Research Council*
F. T. Rosser, Vice-President (Administration and Awards), *National Research Council*

Manuscripts for publication should be submitted to Dr. H. E. Duckworth, Editor, Canadian Journal of Physics, Hamilton College, McMaster University, Hamilton, Ontario.

(For instructions on preparation of copy, see **Notes to Contributors** (inside back cover).)

Proof, correspondence concerning proof, and orders for reprints should be sent to the Manager, Editorial Office (Research Journals), Division of Administration and Awards, National Research Council, Ottawa 2, Canada.

Subscriptions, renewals, requests for single or back numbers, and all remittances should be sent to Division of Administration and Awards, National Research Council, Ottawa 2, Canada. Remittances should be made payable to the Receiver General of Canada, credit National Research Council.

The journals published, frequency of publication, and prices are:

Canadian Journal of Biochemistry and Physiology	Monthly	$3.00 a year
Canadian Journal of Botany	Bimonthly	$4.00 a year
Canadian Journal of Chemistry	Monthly	$5.00 a year
Canadian Journal of Microbiology	Bimonthly	$3.00 a year
Canadian Journal of Physics	Monthly	$4.00 a year
Canadian Journal of Zoology	Bimonthly	$3.00 a year

The price of single numbers of all journals is 75 cents.

Canadian Journal of Physics

Issued by THE NATIONAL RESEARCH COUNCIL OF CANADA

VOLUME 35 NOVEMBER 1957 NUMBER 11

DIFFRACTION OF 3.2 CM. ELECTROMAGNETIC WAVES BY DIELECTRIC RODS

III. LUCITE 1½ IN. DIAMETER SEMICYLINDER, FIELDS VERY CLOSE TO SURFACE[1]

C. E. JORDAN[2] AND A. B. MCLAY

ABSTRACT

The diffraction fields near a long, semicylindrical, 1½ in. diameter rod of lucite, oriented in a nearly plane incident field of 3.2 cm. waves with plane surface towards or away from the source, have been reinvestigated in the region very close to the rod more thoroughly than previously (McLay and Subbarao 1956). The incident field was polarized parallel to the long axis of the semicylinder. In addition, the field near the rod when it was oriented with plane surface aligned with the axis of propagation and the field when the same rod was coated with thin aluminum foil and placed in turn in each of the three above-mentioned orientations have now been observed.

A number of features in the diffraction patterns of the uncoated lucite rod have been qualitatively accounted for as resulting from effects of weak radiation after one or more internal reflections, or from evanescent waves close to a part of the surface where internal incidence is at angles greater than critical, superposed on one or more of the incident, directly transmitted and externally reflected radiations. The patterns a little away from the surface of the uncoated rod and the whole patterns of the aluminum-coated one are quite simple relatively and provide evidence of marked near-field diffraction.

1. INTRODUCTION

Diffraction patterns of a lucite cylindrical rod of 1½ in. diameter and of the same rod machined to a semicylinder in a nearly parallel beam of 3.2 cm. microwaves, with electric vector parallel to the cylindrical axis, have been observed and reported earlier (McLay and Subbarao 1956). The semicylinder was oriented in turn with plane face toward and away from the source. Main features of the patterns were related to those expected on geometrical optics and interference considerations. In the particular case of the diffraction pattern of the semicylinder with plane face towards the source, a noticeable enhancement of the field was observed very closely behind the part of the cylindrical surface, on each side, that should totally reflect internally the incident radiation, and was commented on. This feature was not present in the same region behind the same part of the surface of the full cylinder, where total internal reflection is impossible. A more detailed examination of this region of the field was indicated.

[1]Manuscript received July 29, 1957.
Contribution from the Department of Physics, McMaster University, Hamilton, Ont.
[2]Present address: Raytheon Manufacturing Co., Waltham, Mass., U.S.A.

A reinvestigation of the fields in greater detail very close to the semicylindrical rod has been carried out for both orientations mentioned above. Measurements have also been made of the fields on both sides and behind the same semicylindrical rod with plane face aligned parallel to the incident beam direction. Diffraction fields for this semicylinder have also been observed when it was covered with tight-fitting aluminum foil-wrap, to simulate a conducting rod, of diameter larger than $1\frac{1}{2}$ in. by a factor negligible compared to the wavelength. The same three orientations were used as for the uncoated rod.

2. APPARATUS ARRANGEMENT

The general arrangement of apparatus is essentially similar to that used in earlier experiments on free-field diffraction by cylinders (Wiles and McLay 1954; Subbarao and McLay 1956). The present site of the experiment, however, is not so ideal as that in a very large laboratory room used earlier but not now available. In the smaller room now used reflection and scattering from back and side walls is very troublesome. However, with plentiful use of Sponge Rubber Products Ltd. Microwave Hair Absorbing sheets and after much time spent in finding the best disposition of them, an incident field region was obtained as free or freer from disturbance from scattering as that in the old location, where absorbing material was not used. A further drawback to the present site is that the receiving equipment has to be a little closer to the source, at 4 meters distance compared to some 6 meters in the past. Because of the small diameter of the diffracting object, $1\frac{1}{2}$ in., and the present limited area of field observation, the incident field near the object is still plane to a good approximation.

The 3.2 cm., 9375 Mc./sec. microwaves were generated by a 723 A/B klystron oscillator, with power and 800 c./sec. modulation from a TVN-7BL supply and square-wave modulator. The pyramidal horn radiator is a new one designed to radiate a broader main lobe with flatter front than the former one did and with less side lobe radiation. The horn was not changed with this particular experiment in mind, but for use alternatively for study of diffraction by objects of considerably larger cross-section than the $1\frac{1}{2}$ in. rod. It was constructed from a single sheet of brass to have a mouth 10.1 cm. by 10.1 cm., a flare angle of 15° in the *H*-plane and 17.2° in the *E*-plane to fit onto RG52U wave-guide. The apex in the *H*-plane at the projected intersection of the sides is 38.7 cm. from the center point of the square mouth aperture. The corresponding distance of the apex in the *E*-plane is 33.4 cm. A IN23 B crystal with much of the brass cut away to approximate a matched dipole was used as a field probe. Because of the radius, 3 mm., of the cylindrical ceramic casing, observations could not be made with the dipole axis closer than this distance from a surface. The rectified signal from the crystal was fed through coaxial cable to a narrow-band amplifier with twin-T feedback and thence by a vacuum tube voltmeter type coupling to a Brown Potentiometer Recorder, Type 153 X 12V-X-30. The probe stand and motor drive assembly were the same as used previously but a selsyn motor-driven marker

system has been added for easier correlation of track and recorder chart motions.

The geometry of this experiment is as follows: with the source, assumed to be a vertically polarized line source at the geometrical *H*-plane apex of the horn, the dipole probe with long axis vertical is moved horizontally at right angles to the incident beam direction in a fixed plane 4 meters from the source. The semicylindrical object with cylinder axis vertical (parallel to the incident vibrations) is placed in turn on the axis of propagation at various small distances from the plane of the probe motion. Because the distance of the axis of the rod was within limits of 4.8 cm. ahead of and 1.6 cm. behind the probe plane, the incident field throughout the whole region examined is considered to be plane and identical for all object positions. The results obtained are therefore taken to be the same as if the rod were fixed in position and the probe run changed to examine the diffraction field at various distances from the rod's axis.

For each position of rod with respect to probe run, the field intensity was measured, then the rod was removed and the incident field measured over the same probe run. The ratio of the values measured at each point was taken as that of the intensity of the resultant field normalized to that of the incident field, and denoted as I/I_i in the following sections.

3. RESULTS

Measured diffraction fields close to the semicylindrical lucite rod are shown in Figs. 1 to 5 for three orientations of the rod, labelled I, II, and III. Results are presented as field plots in rectangular coordinates about an origin at the intersection of the horizontal axis of propagation and the vertical axis of the semicylinder coincident with the vertical center line of the plane surface. The curves give the intensity distribution I/I_i for each probe run with certain base lines, $I/I_i = 0$, drawn brokenly so as not to cross any intensity curves. Some of the curves, that show additional detail very close to the rod, drawn only part way out are from runs halfway between adjacent full runs. Their base lines and ordinate values are not marked, except on the larger scale plot of Fig. 2. For orientations I and II of the rod, those symmetrical with the axis of propagation, the patterns shown on one side only (Figs. 1, 2, and 3) are drawn using the average of measurements made on both sides, which were very closely the same. For orientation III, plane face aligned along the axis of propagation (Figs. 4 and 5), separate measurements were made with the orientation shown in the figures and with one 180° from it; the patterns in the figures were drawn using average values of the measurements for the complementary orientations.

The rays shown on Figs. 1 to 5 are boundary ones between beams affected differently by the rod on simple geometrical optics considerations. They are drawn for this lucite material with refractive index taken as $n = 1.6$ and critical angle $C = 38° 41'$ and are labelled similarly to ones for the same cases in Fig. 6 of our earlier report on diffraction by this lucite semicylinder (McLay and Subbarao 1956), as follows:

1, 1′ etc. — incident rays,
S — external surface reflected rays,
T — directly transmitted rays,
R — rays transmitted after one or more internal reflections.

Because of large aberration effects (geometrical optics) refracted beams are not strictly confined between boundary rays, and, of course, spreading of all beams resulting from diffraction will be very marked.

Diffraction fields close to the semicylindrical conducting rod (lucite with foil-wrap coating) are presented in Figs. 6 to 9 similarly to those above.

4. DISCUSSION OF RESULTS FOR THE LUCITE SEMICYLINDER

The diffraction field of the semicylindrical lucite rod in orientation I, plane surface towards source, shown in Figs. 1 and 2 has features similar to that of a full cylinder of the same diameter in the region behind the rods where external surface scattering plays little part (McLay and Subbarao 1956). However, a difference in this region, referred to in the previous paper and in Section 1 above, is an enhancement of the field very close to the surface of the semicylinder. In the present set of experiments the field in this region has been an object of special study with probe runs carried out at several closely spaced distances (Figs. 1 and 2). Fig. 2 is included to show more detail close to the surface than would be clear on Fig. 1.

Inspection of the side diffraction peak nearest to the large central one shows clearly enhancement on approach to the rod. Maximum intensity, as near as can be observed from the plot in Fig. 2, is closer to the surface than the nearest observable value of 0.3 cm. (radius of probe casing) on the 1.6 cm. curve. This would fix it at or very near where ray 2′ meets the cylindrical surface internally at the critical angle. This is just where the evanescent wave in air associated with total internal reflection would be most intense, and the exponential decrease in intensity with increasing distance from the surface slowest (Born 1943), i.e., at critical incidence. Considerable evidence of strong evanescent wave effects has recently been obtained by the authors and Mr. N. E. Hedgecock behind the surface of a large 45-90-45 dielectric prism, oriented in two different ways to an incident microwave beam to totally reflect it. Results of these experiments in the much simpler case of the prism support the interpretation now given that the enhancement of field behind the part of the semicylinder surface that would totally reflect the beam 1′2′ is in most part the contribution of evanescent waves of intensity increasing to maximum across the beam in going from boundary ray 1′ to 2′.

Additional contributions to the field in the region discussed in the preceding paragraphs would be expected on considering incident beams 24 and 45 in Figs. 1 and 2. As shown, beam 24 would be partially reflected internally to emerge after geometrical refraction as a converging beam $R_2'R_4'$ in the back direction. Beam 45, after a partial internal reflection, a total internal reflection at the plane surface, and geometrical refraction, would emerge as a nearly parallel beam $R_4''R_5''$ in the forward direction. The intensity, varying rapidly across beam $R_2'R_4'$, should be fairly large close to ray R_2' because of

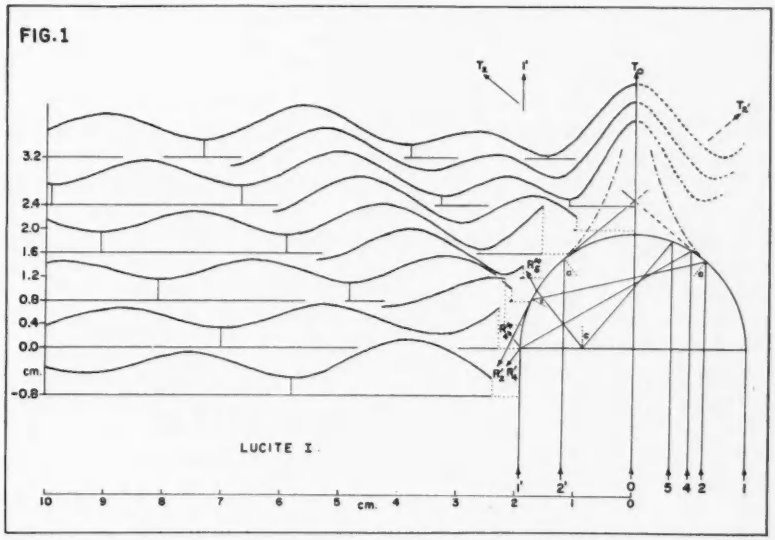

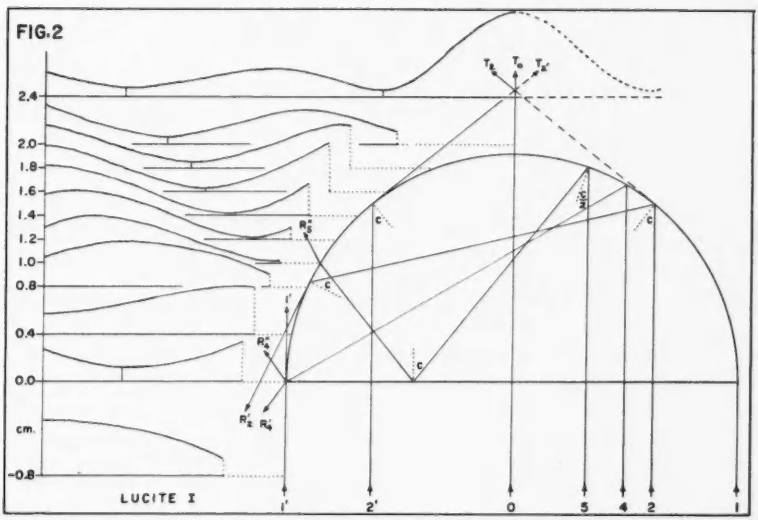

FIG. 1. Variation of the intensity ratio I/I_i (unit value is 0.5 units on ordinate scale) in the diffraction pattern of a long semicylindrical rod with plane face towards the source of 3.2 cm. radiation.

FIG. 2. Part of the pattern of Fig. 1, drawn to twice the rectangular scale with additional curves to show detail very close to the surface (unit value of I/I_i is here 0.25 units on ordinate scale).

partial reflection at angles near critical. Also because of convergence the effect of this beam on the field within and close to its boundaries should be quite pronounced. The normalized intensities at points closest to the rod on the 0.0 and 0.4 cm. curves are both greater than unity and the former curve has not yet reached a maximum on approach. Since according to boundary conditions the intensity should be close to unity at the right angle edge on the 0.0 ordinate and less than unity at the surface on the 0.4 ordinate, the evidence is that the enhancement here is contributed to by internal partial reflection and subsequent refraction. Any contribution to the field resulting from beam $R_4''R_5''$ should be quite small because of partial internal reflection at angles smaller than critical. It is shown only for sake of completeness. These beams were not considered earlier (McLay and Subbarao 1956) because no observations in the region between ordinates 0.0 and 2.3 cm. had been made then and the effects discussed in this paragraph were not evident.

All observed enhancements of field referred to above have been in the very near diffraction field of the dielectric semicylinder in orientation I. Far-field diffraction theory of optical semicylindrical lenses would not cover such effects. Other features of the diffraction field further behind the rod, observed in past and present experiments, are consistent with the diffraction theory of lens aberrations.

Results for the lucite rod in orientation II (Fig. 3) are mostly supplementary to those of the earlier investigation (McLay and Subbarao 1956)

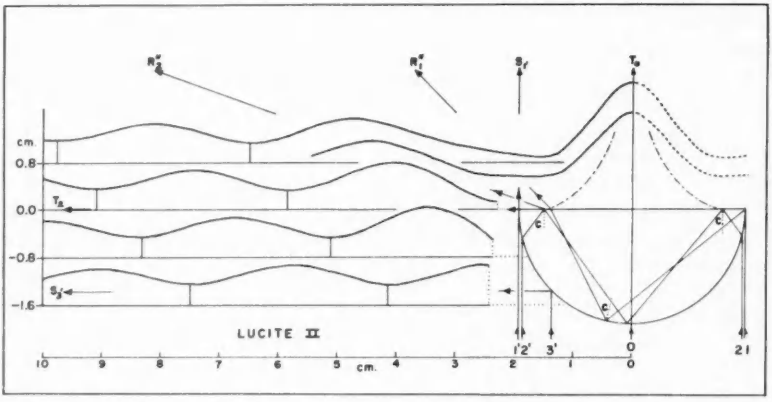

FIG. 3. Variation of the intensity ratio I/I_i (unit value is 0.5 units on ordinate scale) in the diffraction pattern of a long semicylindrical lucite rod with plane face away from the source of 3.2 cm. radiation.

on the field behind the plane face to as far out as 9.6 cm. from it. The present run at 0.8 cm. is a repeat and the one at 0.4 cm. is close to a previous run at 0.3 cm. The new runs at 0.0, −0.8, and −1.6 cm. show the part of the diffraction field resulting from superposition of the incident and surface-scattered fields without other appreciable effects. However, no new features of particular

interest have appeared in this investigation. An irregularity in the shape of the first trough out from the axis of propagation, ray $0T_0$, apparent on the curves at 0.4 and 0.8 cm. was accounted for earlier as an effect of the twice internally reflected beam $R_1''R_2''$ contributing to the resultant field along with the surface scattered beam $S_1'S_3'$, the transmitted beam T_0T_2, and the incident beam bounded on the right by ray 1′. This irregularity was traced previously out to 9.6 cm. behind the rod.

The diffraction fields on each side of the lucite rod in orientation III are shown in Figs. 4 and 5. In Case III*a* for the cylindrical surface side, Fig. 4, the simple field that would result from superposition of the incident beam bounded on the right by ray 1′ and the scattered beam $S_1'S_3'$ is modified by a weak beam $R_1'R_2'$, emerging after total internal reflection of the incident beam 1′2′ from the plane surface. The flattening of the first peak outside the geometrical shadow boundary $1'S_1'$, observable in runs from 0.4 to 3.2 cm., appears to be the effect of this beam being out of phase with respect to the in-phase condition of the other two in the region concerned. The large peak close to the axis of propagation just behind the rod on the run at 2.4 cm. and the rising intensity close to the axis on the 2.0 cm. one show the effect of superposition of radiation of the incident beam 02′, which is concentrated (within a small caustic surface) in a small region close behind the surface before crossing the axis of propagation to the right side of the field, and radiation from the right side of the plane face diffracted into the left-hand field. The intensity of this peak falls off rapidly behind the rod as expected on the above interpretation. The field in Case III*b* on the plane surface side of the rod, Fig. 5, in the region between runs at −1.6 and 2.0 cm. should be closely similar to that caused by diffraction at a right-angled dielectric wedge oriented with one face along the axis of propagation. Boundary conditions require zero intensity at all points on the plane surface.*

Two additional effects resulting from contributions of the incident beam 1′2′ could modify the field on the right side near the back and front corners of the rod. This beam is totally internally reflected at the plane surface as mentioned in Case III*a* but here (as in the different Case I) an evanescent wave in air is expected to travel back parallel to the surface. There is little evidence of this effect unless it is in the finite intensity at the troughs in runs at 2.0 and 2.4 cm. in the narrow region concerned. The same beam as above, 1′2′, after total reflection is re-reflected twice at angles close to critical and emerges, after convergence toward the plane surface, as a backward divergent beam $R_1''R_2''$. A noticeable irregularity in the curves of runs at −0.8 and −1.2 cm. near the rod and in particular the large intensity at close approach on the run at −1.6 cm., definitely not approaching zero boundary value at the surface, seems to be direct evidence of an effect of the beam considered.

The field in Fig. 5 from run 2.0 back is chiefly the simple resultant of two

*The regular change of closest measurable distance from the surface from run to run is because the diode probe is supported at the sharp bevel-nosed end of a hollow ebonite rod of 1 inch diameter, which extends backward horizontally and contains the coaxial lead from the diode. This rod had to be moved sideways a bit at the start of each successive run to allow the probe to clear the plane surface.

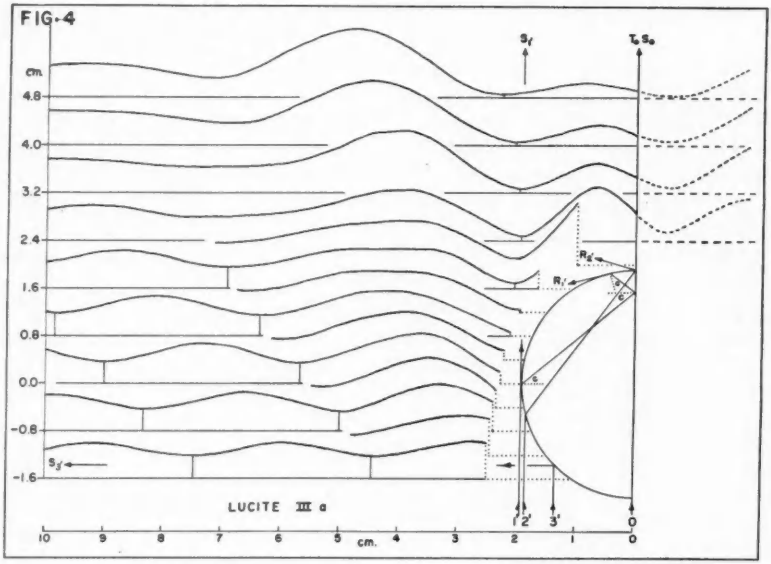

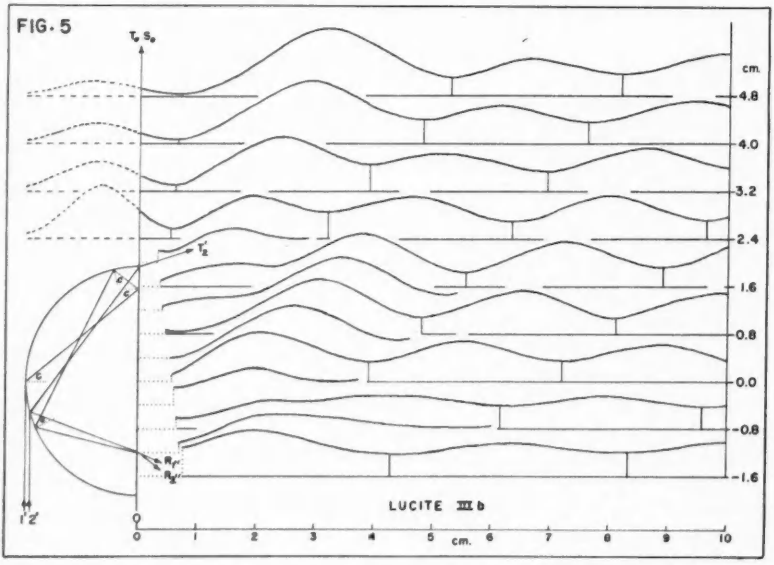

FIG. 4. Variation of the intensity ratio I/I_i (unit value is 0.5 units on ordinate scale) in the diffraction pattern on the cylindrical face side of a long semicylindrical rod of lucite with plane face aligned with the axis of propagation of 3.2 cm. radiation.

FIG. 5. Variation of the intensity ratio I/I_i (unit value is 0.5 units on ordinate scale) in the diffraction pattern on the plane face side of a long semicylindrical rod of lucite with plane face aligned with the axis of propagation of 3.2 cm. radiation.

interfering beams, the direct incident beam bounded on the left by ray $0S_0$ and the divergent beam T_0T_2' transmitted by the semicylinder. The regularity of its features, except close to the back corner of the rod, is consistent with this view.

5. THE ALUMINUM-COATED SEMICYLINDER

The fields of the conducting semicylinder in the same three orientations as for the lucite rod are much simpler and more regular than those of the dielectric one. They are shown in Figs. 6 to 9. In terms of simple, geometrical optics they would involve in various cases, on a given side of the rod, either the uniform field of the parallel incident beam passing the opaque object outside the geometrical shadow edge only, or superposition of this beam and a diverging beam reflected geometrically from a forward quadrant of the cylindrical surface. In the first case only physical optics effects produce the marked variations of intensity observed. In the latter case such effects will also determine the field in general, but most pronounced variations will be expected within and close to the region of overlap of the two geometrical beams. Boundary conditions are simple, requiring zero intensity everywhere at the surface of the conducting rod. Results are given here chiefly for comparison of these experimental fields with those of the dielectric rod and not for detailed comparison with theory.

In the case of orientation I, Fig. 6, the field is quite regular and should be very closely similar to that for a long conducting strip of width equal to the diameter of the semicylinder, except for small deviations expected near the front corner edge of the semicylinder.

In the cases of orientation II, Fig. 7, and III*a*, Fig. 8, on the cylindrical sides, the fields have regular variations and each should be closely similar to that on one side of a full cylinder of the same diameter. The two experimentally observed fields are very similar to each other outside the boundary ray $1'S_1'$, except for greater intensity in the case of orientation II of the first diffraction peak in the curves of runs at 0.0 and 0.8 cm. The difference would be expected because of the markedly different changes of shapes of surface at ordinate 0.0 cm. in the two cases. Differences within the geometrical shadow regions in the two cases are obvious and those to be expected in back-scattering, particularly near abscissa 0, have not been studied here. The field of the conducting semicylinder in Case III*b*, Fig. 9, on the side of the plane face, is not so regular as the other three. It should be closely that of a right-angled conducting wedge with one face aligned with the axis of propagation. The intensity curves tend to zero with approach to the rod in every run, as expected from boundary conditions. But a flattening of the first peak out from the surface is evident in runs taken at ordinates from 0.0 to 1.6 cm. inclusive. As mentioned before, the curves are drawn using the average of measurements made when the rod was in the orientation of Figs. 8 and 9 and when oriented at 180° to that, the two sets of measured values being very closely the same. Thus the effect is certainly not caused by an irregularity in the incident field on one side of the axis of propagation or by a stray effect of side wall or other

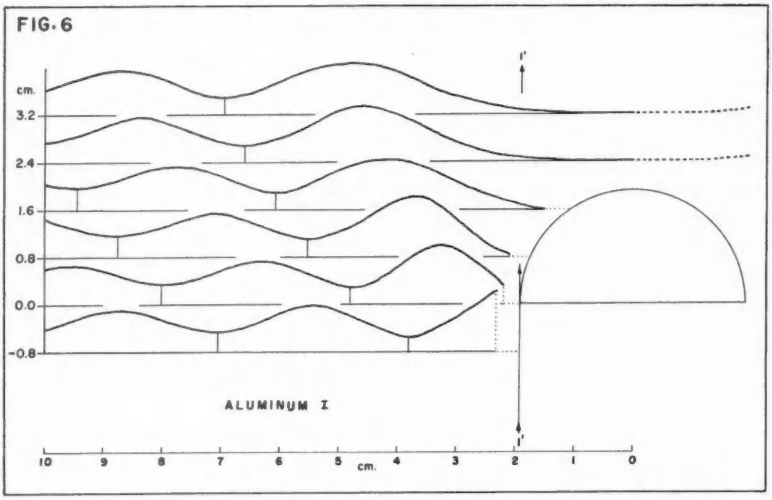

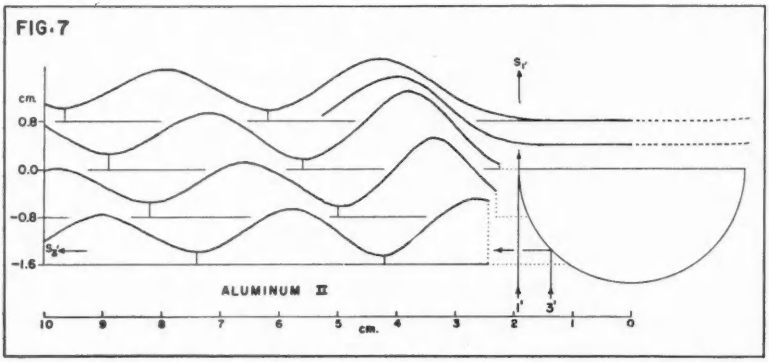

FIG. 6. Variation of the intensity ratio I/I_i (unit value is 0.5 units on ordinate scale) in the diffraction pattern of a long aluminum-coated semicylindrical rod with plane face towards the source of 3.2 cm. radiation.

FIG. 7. Variation of the intensity ratio I/I_i (unit value is 0.5 units on ordinate scale) in the diffraction pattern of a long aluminum-coated cylindrical rod with plane face away from the source of 3.2 cm. radiation.

scattering. It is not likely caused by a surface irregularity of the aluminum foil, which was tightly wrapped on the rod and flat visually on the plane face. It could be the result of the incident wave being only approximately plane and the source not the ideal vertical line one, so that incidence at the plane surface is not uniformly tangential as in the simplest case.

All special features of the diffraction fields of the lucite and aluminum-coated semicylinders observed and discussed here are in the near-field regions

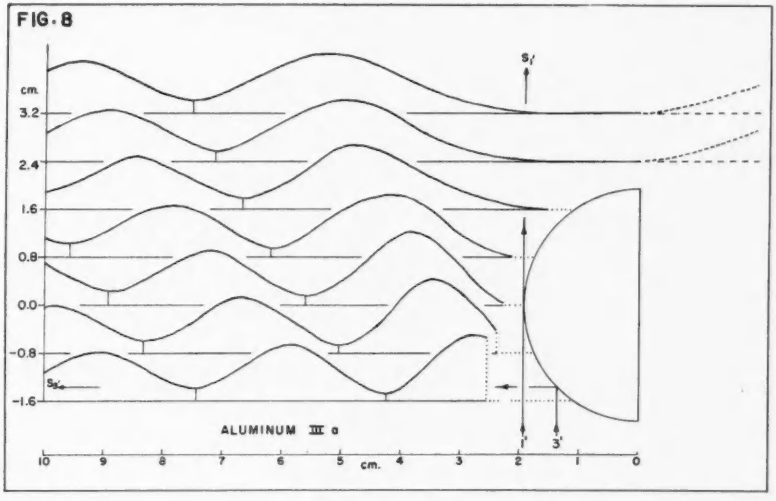

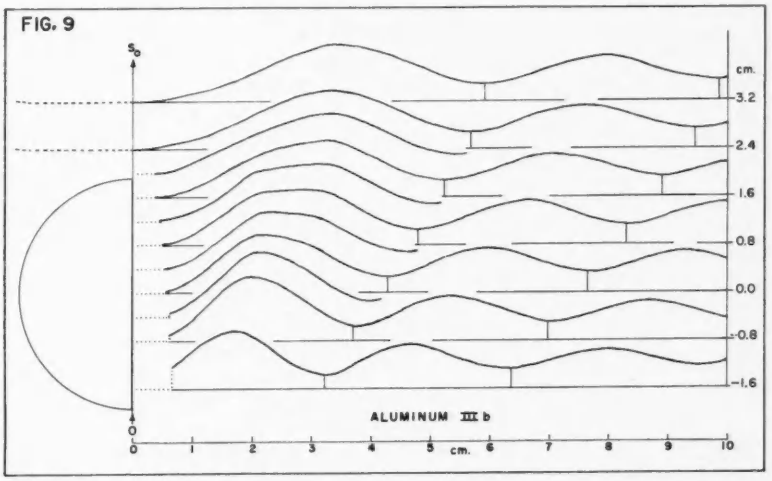

FIG. 8. Variation of the intensity ratio I/I_i (unit value 0.5 units on ordinate scale) in the diffraction pattern on the cylindrical face side of a long aluminum-coated semicylindrical rod with plane face aligned with the axis of propagation of 3.2 cm. radiation.

FIG. 9. Variation of the intensity ratio I/I_i (unit value is 0.5 units on ordinate scale) in the diffraction pattern on the plane face side of a long aluminum-coated semicylindrical rod with plane face aligned with the axis of propagation of 3.2 cm. radiation.

very close to the surfaces. Approximate solutions often found useful for theoretical prediction of far-field diffraction effects will probably not suffice to account for most of these features.

ACKNOWLEDGMENT

The support of the National Research Council by continued grants-in-aid throughout this research is gratefully acknowledged.

REFERENCES

BORN, M. 1943. Optik (Edward Bros. Inc., Ann Arbor, Mich.), Chap. I, Sec. 13.
MCLAY, A. B. and SUBBARAO, M. K. 1956. Can. J. Phys. **34**, 555.
SUBBARAO, M. K. and MCLAY, A. B. 1956. Can. J. Phys. **34**, 546.
WILES, S. T. and MCLAY, A. B. 1954. Can. J. Phys. **32**, 372.

THE LUMINOUS MANTLE OF FUEL-RICH OXYACETYLENE FLAMES

I. SPECTROSCOPIC TEMPERATURE MEASUREMENTS[1]

G. V. MARR[2]

ABSTRACT

The luminous mantle of fuel-rich oxyacetylene flames is a strong source of the 4050 Å bands of the C_3 radical. As a preliminary to the study of the chemical kinetics involved in the formation of the electronically excited C_3 radical, a temperature investigation of the luminous mantle has been undertaken. Rotational measurements are reported for the CH, C_2, and OH bands over a range of burning mixtures of 2.3 to 4.2 times stoichiometric. Self-absorption is shown to occur for OH and C_2 and is indicated for CH. After attempting to correct for this effect, an average rotational temperature for the three radicals of $3000\pm200°$ K. decreasing to $2900\pm200°$ K. is found to be applicable to the luminous mantle over the range of mixtures investigated. Vibrational temperatures obtained for CN and C_2, together with predissociation studies of the CH radical, indicate that small departures from complete thermal equilibrium cannot be eliminated.

1. INTRODUCTION

The premixed oxyacetylene flame burning at mixtures from 2 to 4.5 times stoichiometric possesses an intense white luminous mantle located immediately above the reaction zone and surrounded by the faintly luminous outer cone. The luminous mantle, which is very extensive compared to the thickness of the reaction zone (Fig. 1), should be distinguished from the yellowish luminosity

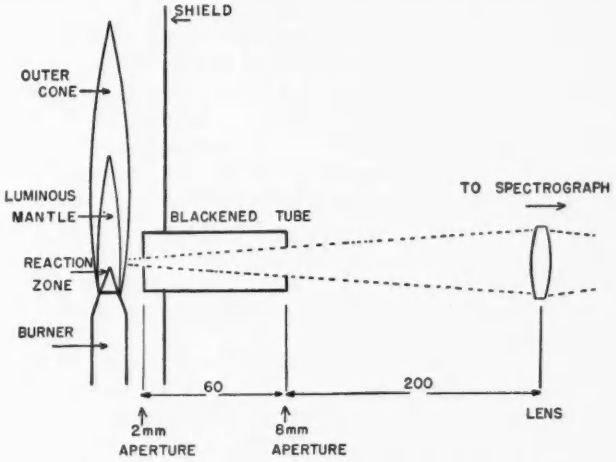

FIG. 1. Schematic diagram of optics; dimensions in mm.

[1]Manuscript received May 21, 1957.
Contribution from the Department of Physics, University of Western Ontario, London, Ontario.
[2]Now at the Eaton Research Laboratory, McGill University, Montreal, Canada.

observed in flames of mixtures richer than about 4 times stoichiometric. The latter flames owe their luminosity to the hot carbon particles formed in the very fuel-rich mixtures and their spectra approach that of a black-body continuum. The white luminous mantle, on the other hand, emits the discrete band spectra from several free radicals, not least of which is the C_3 radical, in addition to the emission from a fairly intense complex background continuum.

The C_3 radical emissions which occur in the 4050 Å region of the spectrum were first observed in the oxyacetylene flame by Kiess and Bass (1954) and are of considerable astrophysical importance in that they play a prominent part in the spectra observed from comets and late N-stars. Recent work by Phillips and Brewer (1955) using a carbon furnace and by Marr and Nicholls (1955) using oxyacetylene flames has shown that for these two laboratory sources, the C_3 bands are associated with a strong violet continuum reaching a maximum at 4000 Å. Kiess and Broida (1956) have verified these observations and carried out an extensive wavelength analysis of the C_3 bands from 3600 Å to 4200 Å. However, to date no work has been done on the study of the conditions necessary for the formation of the excited C_3 radicals. As a preliminary to an investigation of possible reaction mechanisms, a spectroscopic temperature study of some of the free radicals which are prominent features of the luminous mantle has been made.

2. EXPERIMENTAL

A commercial welding torch of 1 mm. nozzle diameter was supplied through flowmeters with commercial cylinder oxygen and acetylene. A rack and pinion device enabled the vertical positioning of the flame relative to the optics to be readily adjusted to within 1 mm. A schematic diagram of the optical arrangement for viewing the flame by a Leeds and Northrup photoelectric recording spectrometer is shown in Fig. 1. Collimating apertures of 2 and 8 mm. diameters were separated by a 60 mm. long internally blackened tube and the cone of light focused by means of a suitable lens onto the entrance slit of the spectrometer. By this means, only light from a small region of the flame was observed at any one time. The spectrum was recorded by means of a grating monochromator (Fastie 1952) capable of distinguishing between two lines of similar intensity which are 0.05 Å apart in the second order. The 800 volts d-c. supply to the IP28 photomultiplier was stabilized to within 0.1% for line voltage fluctuations between 97 and 130 volts at 50 and 60 cycles. A d-c. amplifier, used as a preamplifier to the chart recorder, enabled the output current from the photomultiplier to be displayed on a standard Leeds and Northrup Type-G pen recorder. The amplifier allowed the full scale deflection on the chart to correspond to values of the photomultiplier current ranging from 4×10^{-8} to 2×10^{-11} amp.

Two sets of experiments were carried out, one with a glass condensing lens which enabled intensity measurements to be made over a wavelength range of 3750 Å to 5200 Å in the first spectral order, and the other employing a quartz lens and an ultraviolet filter to remove the first-order spectrum and

enabling measurements to be made over the wavelength range 3000 Å to 3900 Å in the second order. In both cases the wavelength sensitivity of the photomultiplier and the associated optics was obtained by replacing the flame with a calibrated Phillips tungsten filament lamp to correct the recorder readings to relative intensity measurements.

Spectra were recorded from the flames of burning mixtures of 2.3 to 4.2 times stoichiometric with the total flow of gas to the burner kept constant at 2000 cc./min. Measurements were confined to the region of the luminous mantle and reaction zone such that the depth of the optical cone of the emitting gas (disregarding the outer cone) seen by the spectrometer remained constant at about 4 mm. A second set of spectra was taken for flames with a total flow of gas through the nozzle of 1000 cc./min. in order to investigate possible self-absorption effects taking place within the cone viewed by the spectrometer.

3. ROTATIONAL TEMPERATURE MEASUREMENTS

If it may be assumed that near thermal equilibrium, and hence a Boltzmann rotational energy distribution, exists in a luminous source, then the intensity of $I_{K'K''}$ of the rotational lines in a band may be written as

$$I_{K'K''} = A p_{K'K''} \nu^4_{K'K''} \exp[-E_k/kT_{\text{rot}}]. \tag{1}$$

Here K' and K'' are the rotational quantum numbers of the upper and lower rotational levels (for different vibrational and electronic states), E_k is the rotational energy in the upper level, $\nu_{K'K''}$ is the frequency of the emitted radiation in the transition, and T_{rot} is the rotational temperature which may be looked upon as a parameter of the energy distribution. A contains factors relating to units, geometry, vibrational transition probabilities, and the absolute oscillator strength of the whole system and $p_{K'K''}$ is the intensity factor involving the rotational transitional probability and the statistical weight of the states involved. $I_{K'K''}$ is obtained from the height of the rotational lines above the background continuum after correction for variation of the response of the spectrometer and detector with wavelength. E_k may be calculated from the rotational constants for the radical (Herzberg 1950) and $p_{K'K''}$ can be obtained from the statistical weight distribution for the branch or subbranch concerned (Mulliken 1927). Thus by plotting $\log(I_{K'K''}/p_{K'K''}\nu^4_{K'K''})$ against E_k, the rotational temperature may be obtained from the slope of the graph. Departures from the straight line drawn through the points indicate departures from thermal equilibrium. However, self-absorption effects may affect the slope of the line and have to be investigated. The presence of a straight line from which an apparent T_{rot} may be obtained is only an indication of possible local thermal equilibrium.

Reliable intensity measurements for rotational lines were possible for the radicals C_2, CH, and OH. Choice of branches of rotational lines in a band, suitable for temperature determinations, was limited by rather stringent conditions. First, the lines had to be free from overlapping of any other band systems and, secondly, free from overlapping from other branches of the

same band. Thus for the C_2 radical, the (0, 0) band of the $^3\Pi$—$^3\Pi$ system was used since at fairly high rotational quantum numbers ($K \geqslant 40$) the $R_{1,2,3}$ branches of the band were free from overlapping and the three lines in an individual K transition were not resolved by the spectrograph. They then appeared as single lines and the transition could then be considered as a singlet to singlet transition. Only a limited portion of the R_{cd} branch of the (0, 0) band of the $^2\Delta$—$^2\Pi$ system of the CH radical was suitable for T_{rot} determinations. For values of the rotational quantum number $K < 12$, overlapping was severe, and above $K = 21$ predissociation occurred. Again resolution was not sufficient to resolve the spin components and the close doublets were treated as single lines. For the OH measurements, the (0, 0) band of the $^2\Sigma$—$^2\Pi$ transition was used. The R_2 branch was employed, and since the low intensity lines of both extremes of the branch were available, isointensity techniques (Dieke and Crosswhite 1948) could be employed to obtain T_{rot} values which were not liable to be affected by self-absorption effects and provided a check on the other rotational determinations.

3.1. C_2 Rotational Temperatures

The intensities of the blended lines of the combined $R_{1,2,3}$ branches were measured from $K = 40$ to $K = 85$ for the (0, 0) band of the C_2 Swan system and a typical plot of $\log(I/p\nu)$ is shown in Fig. 2. Measurements on the change of T_{rot} with height above the reaction zone tip (Fig. 4) showed only a gradual decrease of T_{rot} with height and it was concluded that temperatures

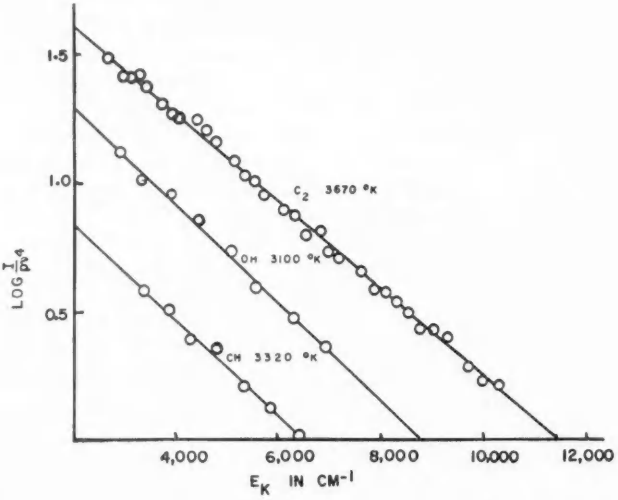

FIG. 2. Logarithmic plots of the rotational lines for the combined R branch of the (0, 0) band of the C_2 $^3\Pi$—$^3\Pi$ system, the R_{cd} branch of the (0, 0) band of the CH $^2\Delta$—$^2\Pi$ system, and the R_2 branch of the (0, 0) band of the OH $^2\Sigma$—$^2\Sigma$ system. The E_k values for the OH transitions are displaced by 3300 cm^{-1} to bring the logarithmic plot for OH into line with the CH and C_2 bands.

for similar regions of flames over a range of fuel/oxygen mixtures could be compared (Fig. 3). The optical depth of the luminous mantle seen by the spectroscope is several orders of magnitude greater than the thickness of the

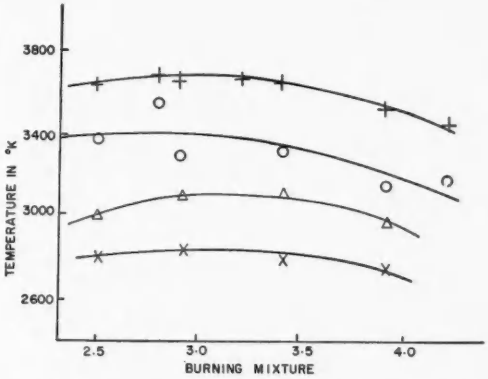

FIG. 3. Plots of rotational temperature with burning mixture. C_2 (+), CH (○), OH (△) values are calculated from logarithmic plots; OH (×) are from isointensity determinations.

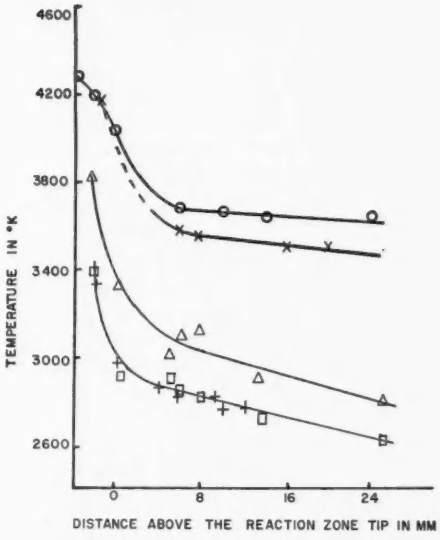

FIG. 4. Variation of rotational temperatures with distance above the tip of the reaction zone. Burning mixture 2.9 times stoichiometric. C_2 (○) experimental points from logarithmic plots for a total gas flow of 2000 cc./min. C_2 (×) experimental points from logarithmic plots for a total gas flow of 1000 cc./min. OH (△) experimental points from logarithmic plots for a total gas flow of 2000 cc./min. OH (□) experimental points from isointensity determinations for a total gas flow of 2000 cc./min. OH (+) experimental points from isointensity determinations for a total gas flow of 1000 cc./min.

reaction zone at atmospheric pressure and it is therefore likely that self-absorption will take place causing a greater suppression of the more intense lines than the weak ones. Since only the tail of the (0, 0) band of the C_2 radical was employed to determine T_{rot}, it is conceivable that self-absorption will not manifest itself as a deviation from a straight line but will cause a change of slope of the line giving a higher apparent temperature than the true one.

To investigate the effect of possible self-absorption, the total flow of gas to the burner was reduced to 1000 cc./min., thus decreasing the optical depth of the luminous mantle seen by the spectrograph by about 25%. Rotational temperature measurements were repeated for different heights above the reaction zone (after allowing for the change in vertical dimension involved) and the C_2 rotational temperatures were plotted as in Fig. 4. The change in the optical depth of the flame caused a reduction of the apparent C_2 rotational temperature by about 150° K. (from an average value over the range of 2.3 to 3.5 times stoichiometric of 3680 ± 100° K. to 3540 ± 100° K.) which is much greater than the random scatter of the points on the curves and just outside the probable error of any single point as deduced from the scatter of points about the best straight line in a logarithm plot. One may therefore conclude that the observation of a straight line plot from equation (1) to deduce T_{rot} does not necessarily imply that a true temperature for a molecule in rotational equilibrium has been obtained. If however rotational thermal equilibrium applies, then the true value of T_{rot} is less than the experimental values obtained.

3.2. CH Rotational Temperatures

A typical example of the CH (0, 0) rotational logarithm plots is shown in Fig. 2 and the variation of T_{rot} with burning mixture is shown in Fig. 3. Unfortunately the limited number of rotational lines available for plots of equation (1) for this radical and the low line to background intensity ratio combined to make the measurements of the apparent temperature less reliable than those of C_2 and a probable error of ±300° K. was obtained assuming local thermal equilibrium. An average value of 3350° K. was obtained for T_{rot} over the range of 2.3 to 3.5 times stoichiometric and over a considerable region of the mantle. The reduction of the flame dimensions by reducing the flow of gas to the burner did not permit such a definite decrease in apparent T_{rot} as was obtained for the C_2 to be observed, but a small decrease ($\sim$80° K.) was indicated.

3.3. OH Rotational Temperatures

Dieke and Crosswhite (1948) have shown that by using equation (1) in conjunction with two lines of comparable intensity (one of high K and one of low K) then a value of T_{rot} may be obtained. Such a value would be independent of self-absorption since lines of equal intensity will be reduced by identical amounts through self-absorption. A comparison of the lines of $K = 1, 2, 3, 4$ with lines of high K was made for the R_2 branch of the (0, 0) OH band and mean values of T_{rot} were obtained from data presented by Dieke and Crosswhite (1948). The variation of T_{rot} with burning mixtures is shown in Fig. 3 and the variation of rotational temperature with height

above the burner is shown in Fig. 4. Changing the dimensions of the flame by reducing the flow to 1000 cc./min. does not affect the values of the apparent T_{rot} and an average value of $2850\pm100°$ K. was obtained. This gives confidence to the assertion that the isointensity method enables meaningful rotational temperatures to be measured in the presence of self-absorption.

With the aid of the intensity factors given by Dieke and Crosswhite (1948), logarithmic plots to determine T_{rot} are also included in Figs. 3 and 4. The points for the latter plots have been taken from the high K tail of the band (Fig. 2) and while self-absorption would not be expected to be very great since the lines are of low intensity, the trend should be the same as for C_2 and CH. An average value of $3100\pm200°$ K. for the apparent T_{rot} was obtained, indicating that self-absorption does affect the logarithmic derivations of T_{rot}.

4. VIBRATIONAL TEMPERATURES

Similar assumptions to those made in Section 3 as to the possibility of a Boltzmann vibrational energy distribution enable the integrated intensity over a fixed set of rotational lines in a vibrational transition to be expressed by

$$I_{v'v''} = A'P_{v'v''}\nu^4_{v'v''}\exp[-E_{v'}/kT_{vib}]. \tag{2}$$

A' now includes the rotational transitional probabilities' sum for the lines concerned, the electronic transition probability, and the instrumental factors. $P_{v'v''}$ is the vibrational transitional probability and $E_{v'}$ is the energy of the upper vibrational state v'. The other factors have similar meanings to those in equation (1). $E_{v'}$ may be calculated from the molecular constants for the radical but $P_{v'v''}$ is a much more difficult proposition. Smoothed arrays of relative transition probabilities ($p_{v'v''} = P_{v'v''}/P_{00}$), however, have been obtained for several band systems (Nicholls 1956) and equation (2) may be adapted to use these $p_{v'v''}$ values. Since vibrational transition probabilities are only known relative to that of the (0, 0) transition, we may write

$$I_{v'v''}/I_{00} = p_{v'v''}(\nu^4_{v'v''}/\nu^4_{00})\exp[-(E_{v'}-E_0)/kT_{vib}]. \tag{3}$$

By taking logarithms, values of the apparent vibrational temperature may be obtained. Again T_{vib} is subject to the same limitations as T_{rot}. In general the overlapping of the bands and the accuracy of the relative transition probabilities places a limit to the reliability of this type of measurement.

The observations on the vibrational distributions have been limited to the CN ($^2\Sigma$—$^2\Sigma$) and the C_2 ($^3\Pi$—$^3\Pi$) systems of the free radicals. Vibrational temperatures were estimated for the CN radicals by integrating the intensity at the band heads of the (0, 0), (1, 1), and (2, 2) bands for the same rotational lines which were blended together at the band head. Similarly the band heads of the (0, 0), (1, 0), (1, 1), (2, 1), (3, 2), (3, 1), and (4, 2) bands of the C_2 system were measured to obtain an estimate of the vibrational temperature for this radical. To a good approximation, the same fraction of the band was thus used in each case although the fraction may depend somewhat on v' (Nicholls 1956). In each case the change of T_{vib} with burning mixture was similar to the corresponding curves (Fig. 3) for T_{rot} and only differed in the

absolute magnitude of the temperatures obtained. The average value obtained for C_2 T_{vib} is $3900 \pm 400°$ K. over the range of mixtures examined while that for the CN radical is $3600 \pm 400°$ K. Again the probable error is a measure of the scatter obtained for the individual points from which the apparent temperatures were obtained.

5. PREDISSOCIATION OF CH

Durie (1952) investigated the effect of gradually replacing the C_2H_2 by hydrogen in C_2H_2/O_2 flames while keeping the stoichiometry of the mixture constant. He observed that predissociation effects for the $^2\Sigma$—$^2\Pi$ system of CH were suppressed. The effect took place in the neighborhood of twice stoichiometric for the H_2/O_2 flames with 1 to 3% of C_2H_2 added. Under normal burning conditions the hydrocarbon/oxygen flames were observed to terminate their CH bands abruptly, that of the (0, 0) $^2\Sigma$—$^2\Pi$ band to terminate at $K = 17$, and the (1, 0) and the (1, 1) bands of the same system to end at $K = 7$ (Gaydon 1948). In the hydrogen-rich flame however, Durie observed lines up to $K = 20$ in the (0, 0) band and $K = 13$ in the (1, 0) and (1, 1) bands. The interpretation placed on the suppression of the predissociation by Durie was that an approach to thermal equilibrium was being observed as distinct from the chemiluminescence observed for pure C_2H_2/O_2 flames and that the observation of lines of high K values could be used as a test of the completeness or otherwise of thermal equilibrium.

Observation of a weakening in the intensity distribution in the high rotational quantum levels is consequently evidence of a non-thermal excitation mechanism for the CH radical. Broida (1953) verified the observations of Durie (1952) and for the reaction zone of fuel-rich C_2H_2/O_2 flames was able to observe an extension of the rotational lines to $K = 20$ for the (0, 0) band of the $^2\Sigma$—$^2\Pi$ system. By increasing the amplification of the photomultiplier current and by backing off the background continuum contribution with the suppression control on the recording console, it was evident in the present experiments that the partial suppression observed by Broida for the CH bands was carried into the luminous mantle. The presence of the closely packed rotational lines of the C_3 bands in the region 3980 to 4000 Å reported by Kiess and Broida (1956) and confirmed by the present observations, together with the broadening of the lines affected, prevented a more detailed examination of the effect. It was concluded therefore that the suppression of predissociation in the luminous mantle is at least equal to that in the reaction zone. Thus while there is still probably some departure from complete thermal equilibrium based on the predissociation effects, it is certainly not as great as that observed in the reaction zones of leaner flames than those which allow the formation of the luminous mantle.

6. DISCUSSION

From the preceding sections, it is apparent that the measured rotational temperatures for any one radical and method do not change appreciably over the range of fuel/oxygen ratios examined (Fig. 3). The decrease in

apparent rotational temperature with height above the reaction zone is not severe for the luminous mantle (Fig. 4), and the observations are consistent therefore with the concept of a spatially non-localized rotational temperature applicable to the radicals concerned. For the purpose of discussion, average rotational temperatures for the region within a few millimeters above the reaction zone, and applicable for about 2.3 to 3.5 times stoichiometric, will therefore be considered as the free radical rotational temperatures for the flame. Thus for the C_2 radical, the apparent T_{rot} is $3680\pm100°$ K.; however on reducing the physical dimensions of the flame, a value of $3540\pm100°$ K. is observed (Fig. 4).

For the CH radical a value of $3350\pm300°$ K. is observed for T_{rot} (Fig. 3) and reduction of the flame dimensions indicated a slight decrease in apparent temperature. However this is not so marked as in the case of the C_2 radical. The OH radical enabled two sets of observations to be made. The logarithmic determinations of T_{rot} indicated a value of $3100\pm200°$ K. while the isointensity determinations yielded a value of $2850\pm100°$ K. (Figs. 3 and 4). The latter determination is not affected by self-absorption which undoubtedly accounts for the decrease in the value as observed from the former type of observation.

It is of interest to note that the values of apparent rotational temperatures obtained by the logarithmic plots are higher for the more intense systems like C_2 than for the much weaker lines of a radical like OH. Consequently, other things being equal, one would expect the self-absorption effects to be greater for C_2 than for CH and OH, which is in agreement with the trend of the apparent rotational temperatures. Certainly the change of the apparent rotational temperature with flame dimensions is greater for C_2 than for CH and OH. The rotational temperature observations therefore do not conclusively indicate a separate temperature to be assigned to each of the free radicals and do not reveal the presence of any chemiluminescent radiation in any one radical rather than another. It should also be noted that the OH isointensity rotational temperature is in agreement with outer cone determinations of T_{rot} for rich C_2H_2/O_2 mixtures by Broida (1954) and since the observations reported here were obtained through the outer cone, the value of $2850\pm100°$ K. might be indicative of the region surrounding the luminous region rather than the OH rotational temperature inside the mantle. At least they probably indicate a lower limit to the rotational temperature of the luminous region and there is probably no great decrease in temperature in passing from the luminous region to the outer cone. The experimental observations of rotational temperatures are therefore consistent with the assignment of a true rotational temperature for the three radicals of $3000\pm200°$ K. for these flames. By similar considerations for flames burning at richer mixtures than 3.5 times stoichiometric, an average value of the true rotational temperature of 2900 $\pm200°$ K. was determined.

The vibrational observations on the C_2 and CN systems were based of necessity on the band head intensity of the (0, 0) band in each case. A high value of T_{vib} would be obtained if too small a contribution to the Boltzmann distribution was ascribed to this band. For both the C_2 and CN systems

the intensity of the (0, 0) band head was very strong; in the C_2 case it was much greater than the intensity of the rotational lines used to determine T_{rot}. Self-absorption effects may thus be expected to contribute to the discrepancy between the apparent vibrational and rotational temperatures. Whether the discrepancy between the vibrational and rotational temperatures is real or not cannot yet be definitely established. The possibility of chemiluminescence cannot therefore be discarded from these observations, particularly for the C_2 radical.

While it is not possible to say that departures from complete thermal equilibrium are eliminated by the predissociation studies, they are much less than is normally encountered in the reaction zones of premixed flames. In conjunction with the T_{vib} determinations, departures from complete thermal equilibrium may occur. The presence of a common Boltzmann distribution maintained by flame processes in the rotational degrees of freedom however is a strong indication that large departures from complete thermal equilibrium do not occur and that the rotational temperatures do not significantly differ from the kinetic temperature of the luminous mantle. These observations will be considered in connection with intensity measurements on the C_3 radicals in a forthcoming paper.

ACKNOWLEDGMENTS

The author would like to acknowledge a number of discussions with Dr. R. W. Nicholls as a result of which the above work was undertaken. The research was supported in part by the following agencies whose assistance is gratefully acknowledged: The Defence Research Board of Canada (Grant DRBC 5001-15), The National Research Council of Canada (Capital Grant for the purchase of the spectrometer), The Air Force Cambridge Research Centre (Contract AF 19(604)-1718), and Imperial Oil of Canada.

REFERENCES

Broida, H. P. 1953. J. Chem. Phys. **21**, 340.
——— 1954. Natl. Bur. Standards (U.S.) Circ. **523**, 23.
Dieke, G. H. and Crosswhite, H. M. 1948. Bumblebee Series, Report No. 87, Bur. Ord. U.S.N.
Durie, R. A. 1952. Proc. Phys. Soc. A, **65**, 125.
Fastie, W. G. 1952. J. Opt. Soc. Am. **42**, 641.
Gaydon, A. G. 1948. Spectroscopy and combustion theory, 2nd ed. (Chapman and Hall, Ltd., London).
Herzberg, G. 1950. Molecular spectra and molecular structure, Vol. I, 2nd ed. (D. Van Nostrand Co. Inc., New York).
Kiess, N. H. and Bass, A. M. 1954. J. Chem. Phys. **22**, 569.
Kiess, N. H. and Broida, H. P. 1956. Can. J. Phys. **34**, 1471.
Marr, G. V. and Nicholls, R. W. 1955. Can. J. Phys. **33**, 394.
Mulliken, R. S. 1927. Phys. Rev. **29**, 637.
Nicholls, R. W. 1956. Proc. Phys. Soc. A, **69**, 741.
Phillips, J. G. and Brewer, L. 1955. Mém. soc. roy. sci. Liège, **15**, 314.

THE LUMINOUS MANTLE OF FUEL-RICH OXYACETYLENE FLAMES

II. FREE RADICAL AND CONTINUUM INTENSITIES, AND THEIR INFLUENCE ON C_3 EMISSIONS[1]

G. V. MARR[2]

ABSTRACT

The spectroscopic emissions from the luminous mantle of the oxyacetylene flame have been examined over a range of burning mixtures from 2.3 to 4.2 times stoichiometric. Plots of the band-head intensities for the radicals C_2, C_3, CH, and CN for different burning mixtures and for vertical traverses through the flame are reported. From a study of the variation of the background continuum from 3000 Å to 5200 Å with burning mixtures, the over-all continuum may be considered to consist of (*a*) a black-body carbon particle continuum having an energy distribution corresponding to a temperature of 2900±200° K., (*b*) a continuum associated with the C_3 radical emissions extending from 3500 Å to 4600 A with a maximum at 4000 Å, and (*c*) an ultraviolet continuum extending from below 3000 Å to 5000 Å which appears similar to the carbon-monoxide flame continuum. Within the limits of experimental error the variation of the C_3 bands and their associated continuum are identical. Possible reaction mechanisms for the production of the C_3 emissions are considered and they probably may be accounted for by the reaction scheme

$$C_2(X\,^3\Pi) + C(^3P) \rightarrow C_3(\Sigma) + h\nu \text{ (cont.)}$$

followed by

$$C_3(\Sigma) \rightarrow C_3(\Pi) + h\nu \text{ (bands).}$$

1. INTRODUCTION

The luminous mantle of an oxyacetylene flame burning at mixtures of 2.3 to 4.5 times stoichiometric is a strong source of the 4050 Å bands of the C_3 radical (Kiess and Bass 1954). A detailed spectroscopic wavelength analysis of these bands has been undertaken by Kiess and Broida (1956) but little attention has been directed to a study of the reaction mechanisms capable of explaining the spectroscopic observations. Marr and Nicholls (1955) reported the observation of a violet continuum which appeared to be associated with the C_3 bands and which resembled that assigned to C_3 in the emissions from a carbon furnace by Phillips and Brewer (1955). As a preliminary to a more detailed study of the luminous mantle, Marr (1957)* investigated the temperatures for different radicals in the mantle and concluded that an average temperature of 3000±200° K. was indicative of the luminous mantle over much of the fuel/oxygen range. While departures from complete thermal equilibrium could not be entirely eliminated, they appeared to be small. It is the purpose of the present paper to consider the variations of the intensities of the carbon radical bands and background continuum with flame conditions and to discuss possible mechanisms for the formation of the C_3 radical which are consistent with the observations.

[1]Manuscript received May 21, 1957.
Contribution from the Department of Physics, University of Western Ontario, London, Ontario.
[2]Now at the Eaton Research Laboratory, McGill University, Montreal, Canada.
*Referred to hereinafter as Paper I.

2. EXPERIMENTAL

The optical arrangement, photoelectric recording spectrometer, and intensity calibrations have been fully described in Paper I and were used for the intensity studies reported here. Spectra were recorded in the second order using a quartz condensing lens and a Corning U.V. filter (No. 9863) over a wavelength range 3000 Å to 3950 Å, and in the first order using a glass condensing lens over a wavelength range 3750 Å to 5200 Å. By summation of the contributions of the rotational lines of the (0, 0) bands of the free radicals C_2, C_3, CH, CN to the band-head intensities (see Paper I), a measure of the concentrations of the electronically excited radicals can be obtained. While this method does not enable estimates of the absolute concentrations of the free radicals to be determined, it does allow changes in concentration of the excited radicals with flame conditions to be followed. Studies of the intensity variations of the background continua over a wavelength range 3000 Å to 5200 Å have also been made by combining the spectra from the first and second orders of the spectrometer.

3. THE FREE RADICAL INTENSITY VARIATIONS

Plots of the integrated band-head intensities versus reduced fuel/oxygen ratios (ρ) are shown in Fig. 1 for the excited electronic states $CN(^2\Sigma)$, $CH(^2\Delta)$, $C_2(^3\Pi)$, and $C_3(\Sigma)$ taken for a region within a few millimeters of the tip of the reaction zone. Similar plots for the variation of the intensities with height above the reaction zone are given in Fig. 2 for a flame of $\rho = 2.9$ times stoichiometric. The scales in Figs. 1 and 2 have been adjusted to combine the curves for all four radicals on the same graph. For the sake of clarity, the experimental points have not been included in Fig. 1. The scatter of points about the curves is such that the probable error for each curve is not more than

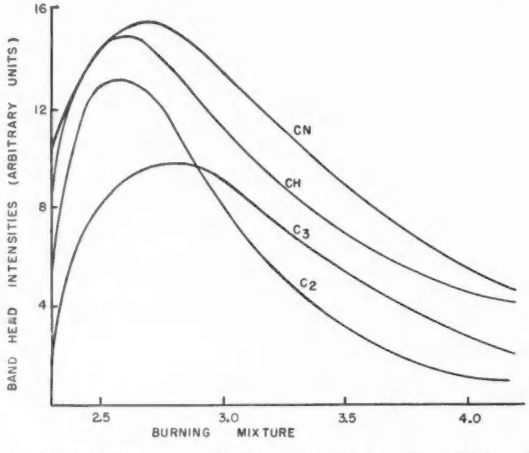

FIG. 1. The variation of the carbon radical band head intensities with burning mixture.

$\pm 7\%$. From Fig. 1 it is evident that the curves for all the radicals are similar in that they show a decrease in intensity towards the limits of the range of

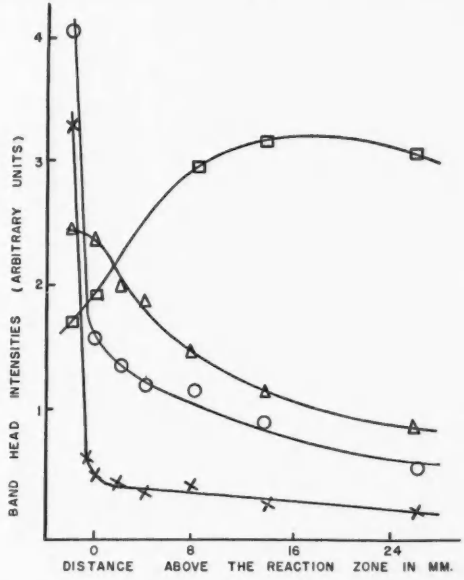

FIG. 2. The vertical variation of the carbon radical band head intensities through the reaction zone and luminous mantle. ○, C_2 radical; □, CN radical; △, C_3 radical; ×, CH radical.

mixtures examined. Part of the observed variation may be attributed to changes in the physical dimensions of the luminous mantle with ρ. However these are likely to be small and the general shape of the curves is indicative of the change in burning conditions with increase of fuel content. Thus it is evident that there is an optimum value of ρ for the emission of each free radical in the luminous mantle. In particular, both C_2 and CH have a maximum at leaner mixtures than C_3, and the C_2 intensity decreases more rapidly than either C_3 or CH to richer burning mixtures.

The variation of the free radical intensities with height above the burner is shown in Fig. 2 for a flame of $\rho = 2.9$ times stoichiometric. Over the range of the observations, the thickness of the luminous mantle remained constant and, if the discontinuities which may arise in crossing the reaction zone are neglected, the curves are effective plots of the change in concentration of electronically excited free radicals with height above the reaction zone. It is assumed in the above statement that the effects of self-absorption (see Paper I) do not vary appreciably over the range of the observations, confirmation of which was obtained by observations on a smaller flame.

A characteristic of the observations is the rapid decrease in intensity of

the C_2 and CH excited radicals on crossing the reaction zone boundary into the luminous mantle, the latter showing a more abrupt change than the former excited radical. The CN radical variation on the other hand shows a considerable increase through the reaction zone and part of the luminous mantle and is indicative of the formation of CN by the entrainment and subsequent dissociation of the N_2 molecules from the surrounding air. It is absent from the reaction zone of lean flames which do not have a luminous mantle, and the intensity observed in the region of the reaction zone in the present experiments is compatible with the amount which would be observed by emission from that portion of the luminous mantle surrounding the reaction zone. The C_3 band emission, while showing a maximum in the immediate neighborhood of the reaction zone tip, is probably affected by the presence of the strong CH line from the reaction zone in the neighborhood of 4050 Å, giving too high a value to the integrated intensity. Observations made lower in the flame, where most of the light comes from the reaction zone, suggest that the C_3 bands are not emitted from the reaction zone. Probably the state of affairs corresponds to that of a uniform decrease of C_3 concentration from the region immediately above the reaction zone with increasing height above the reaction zone. Thus it appears likely that the C_3 band emissions are confined to the luminous mantle.

For rich flames ($\rho > 2.9$), the decrease of the free radical intensities with height above the reaction zone is less rapid; however the luminous region extends over a greater distance and the fractional decrease with height is not significantly altered.

4. THE CONTINUUM

Plots of the intensity variation of the background continua over a wavelength range of 3000–5200 Å for the fuel/oxygen ratios of 2.5–4.2 times stoichiometric have been obtained from both the first-order spectral region of 5200–3750 Å and the second-order region, 3900–3000 Å. Fig. 3 is a typical continuum obtained for a flame of 3.4 times stoichiometric. The accuracy of the over-all variation of intensity with wavelength is governed by the reliability of the calibration curves over the range 3000 Å to 5200 Å and by the steadiness of the flame. From a study of the reproducibility of the intensity traces and by a comparison of the section of the continuum from 3800 Å to 4500 Å with the photographic observations over the same region (Marr and Nicholls 1955) it is estimated that the probable error is not more than $\pm 5\%$. The variation of the continuum profile with change in height above the burner is not appreciable; a steady decrease in intensity with increase in height is observed. The continuum profile, however, shows a marked change in composition with change of ρ. For very rich mixtures, the carbon particle black-body continuum becomes the dominant feature (Fig. 3) and the familiar yellowish carbon particle radiation color can easily be seen in the flame. From such flames ($\rho \simeq 4$) it is possible to determine a brightness temperature from the background radiation of $2900 \pm 200°$ K. Since the rotational and vibrational measurements (Paper I) indicate only a relatively small change of temperature

with fuel/oxygen ratio, and the rotational measurements also yield 2900 ±200° K. for burning mixtures in the neighborhood of 4 times stoichiometric, it is possible to use this black-body distribution to estimate the carbon particle

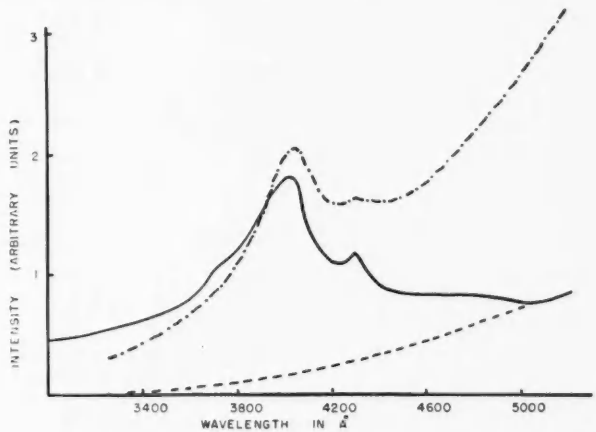

FIG. 3. ——— The luminous mantle background continuum for a flame of 3.4 times stoichiometric. —·—· The luminous mantle background continuum for a flame of 4.2 times stoichiometric (*V* dimension extended by factor of 4). — — — Black-body distribution for 2900° K.

contribution to the background radiation for the luminous mantle of leaner mixtures. The carbon particle continuum may thus be subtracted from the over-all blue-violet continuum and it is evident that unless the emissivity of the carbon particle changes by more than a factor of 10 over this range, then it is not possible to account for a considerable portion of the continuum below 4000 Å. That such a change in the emissivity is unlikely is indicated by the work of Rössler and Behrens (1950). They observed that the emissivity (α_λ) of carbon particles in flames could be expressed in the form $\alpha_\lambda \propto \lambda^{-n}$ where n has values ranging from 1.43 to 0.65 depending on the flame in question.

Removal of the black-body continuum from Fig. 3 leaves the full curve shown in Fig. 4. A comparison of the continuum profile of Fig. 4 with the C_3 continuum (Fig. 4*a*) of Phillips and Brewer (1955) suggests that the C_3 continuum is superimposed on a broad continuum extending into the ultraviolet. Diederichsen and Wolfhard (1956) have published an uncorrected CO flame continuum photographic density plot, which when compared with their published tungsten lamp curve is reasonably similar to the dotted curve in Fig. 4. It is therefore possible to attempt a separation of the over-all luminous mantle continuum into three continua and to plot a variation of their integrated intensities against the reduced fuel/oxygen ratio. Such plots are given in Fig. 5. The Phillips and Brewer points are seen to follow the curve for the C_3 band variation in Fig. 1 while the black-body and U.V. con-

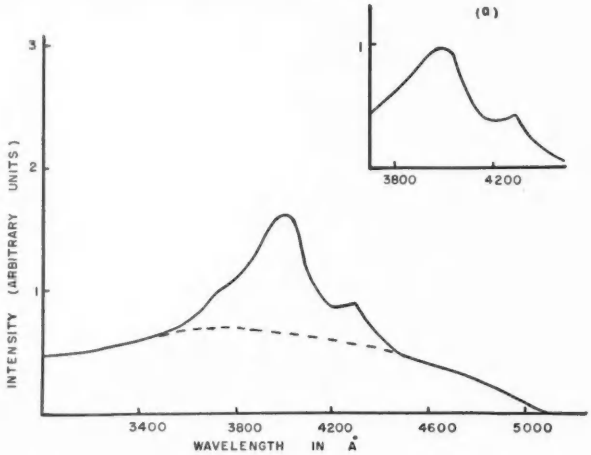

FIG. 4. The background continuum for a flame of 3.4 times stoichiometric after subtraction of the carbon particle black-body continuum. Inset (*a*): The C_3 continuum observed in the furnace experiments of Phillips and Brewer (1955).

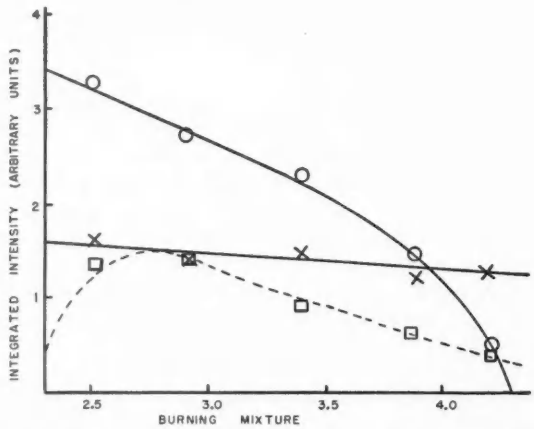

FIG. 5. The variation of the integrated intensities of the luminous mantle continua with burning mixture. ○, the ultraviolet CO continuum; ×, the carbon particle black-body continuum; □, the C_3 continuum; – – – the C_3 integrated band head intensity of Fig. 1.

tinua are quite different. The variation of the continua with height above the reaction zone is not so pronounced, as the components are not changing appreciably. However, within the limits of probable error in separation of the continua components, the Phillips and Brewer continuum appears to follow most closely that of the C_3 band variation. There is, however, no sharp discontinuity across the reaction zone as observed for the C_2 and CH radicals

for any of the three continua. The long wavelength limit to the U.V. continuum is found to be about 5000 Å and extends beyond 3000 Å, while the Phillips and Brewer continuum has a probable short wavelength limit of 3500 Å and a long limit of 4600 Å.

5. DISCUSSION

Over the reduced fuel/oxygen ratios of 2.3 to 4 times stoichiometric, the major portion of the background radiation in the blue-violet region appears to be made up from the Phillips and Brewer C_3 continuum plus a flat continuum which extends into the ultraviolet region and has the appearance of the usual hydrocarbon flame continuum observed in the reaction zone of a variety of hydrocarbon premixed flames. In line with the explanations put forward by Gaydon (1948) it is likely that the reactions

$$\text{(1)} \qquad CO + O \rightarrow CO_2 + h\nu,$$

$$\text{(2)} \qquad OH + OH \rightarrow H_2O_2 + h\nu$$

should be considered as giving rise to the U.V. continuum. The continuum shows a marked decrease in intensity with decrease in the oxygen content of the flame (Fig. 5), and a comparison of the background radiation in the neighborhood of the OH band head at 3050 Å showed a considerable decrease in the continuum as the region under observation moves from the luminous mantle to the outer cone, while the intensity of the OH band does not change appreciably. Thus it appears more than likely that reaction (2) does not appreciably contribute to the background radiation in this region of the spectrum and that the CO reaction is the more likely one to explain the U.V. continuous emission.

Behrens (1953), in his investigations of the formation of carbon in fuel-rich hydrocarbon flames, observed that the fuels could be typified by two limiting cases. In one, dissociation of the excess fuel molecules takes place in the preheating region of the flame and in the other, the dissociation is deferred until passage through the reaction zone. Acetylene is a good example of the latter, and for mixtures richer than twice stoichiometric, the excess fuel molecules may be expected to give rise to an excess of free radicals entering the luminous mantle which are formed by the acetylene dissociation products. The work of Ferguson (1955) on the C_2 Swan bands arising from $C_2^{12}H_2/O_2$, $C_2^{13}H_2/O_2$, and $C^{12}C^{13}H_2/O_2$ flames is consistent with the assumption that the original carbon–carbon bonds in the fuel molecules do not in general survive the reaction zone for stoichiometric mixtures. However it was not possible to show conclusively that *all* the original carbon–carbon bonds are ruptured and indeed it appeared that a small proportion do survive. For rich flames, in which the luminous mantle is formed, it is probable that the number of surviving bonds is not negligible and it is possible that they can provide a significant number of unexcited C_2 radicals. It is to be expected therefore that considerable quantities of free C and H atoms, together with the radicals CH and C_2, will be entering the luminous mantle from the reaction

zone. This is consistent with the ready formation of CN and NH radicals by the entrainment and subsequent dissociation of N_2 from the surrounding atmosphere.

The C_3 emissions appear to be confined to the luminous mantle, so that probable exothermic reactions capable of forming appreciable quantities of the C_3 radicals in electronically excited states from the above free radicals and atoms may be confined to:

$$C_2 + CH \rightarrow C_3 + H + \sim 90 \text{ kcal.}, \tag{3}$$

$$C + C_2 \rightarrow C_3 + \sim 170 \text{ kcal.}, \tag{4}$$

where the heats of formation of C_2 and C_3 are taken to be 140 kcal. and 310 kcal. respectively (Goldfinger 1955) and that of CH to be 80 kcal. (Gaydon 1947). Reaction (3) was proposed by Goldfinger (1955) as one step in the chain process maintained by CH for the polymerization of carbon to form soot. Reaction (4) is the reverse process to photodissociation and is hence similar to reactions (1) and (2), which are favored for the emission of the continua in carbon monoxide and hydrogen flames respectively (Gaydon 1948).

From the spectroscopic evidence obtained by a study of the C_3 band structure, Douglas (1951) has assigned a probable electronic transition $\Sigma \rightarrow \Pi$ to the vibrational bands and it now seems reasonable to consider the C_3 radical as a linear molecule (Clusius and Douglas 1954). The position of the C_3 bands in the spectrum requires that 70 to 80 kcal. of energy are needed to form the excited Σ state of C_3. The continuum, on the other hand, has an upper limit of 82 kcal. (3500 Å). Thus both equations (3) and (4) are sufficiently exothermic to dissipate energy in the form of a continuum or bands. If separate reactions are responsible for the emission of the C_3 bands and the C_3 continuum, a variation of the intensities of the bands and the C_3 continuum with respect to each other would be expected when the flame conditions are changed. Such an effect has not been observed, indicating that a single reaction scheme should be considered for the emission of both band and continuum. This being the case, reaction (3) is not so probable on energy grounds as reaction (4), which can emit radiation by both band and continuum by the following process:

$$C(^3P) + C_2(X\,^3\Pi) \rightarrow C_3(\Sigma) + h\nu \text{ (cont.)} \tag{5}$$

followed by $C_3(\Sigma) \rightarrow C_3(\Pi) + h\nu$ (bands).

Reaction (3) may still be considered for the formation of the bands alone as follows:

$$C_2(X\,^3\Pi) + CH(X\,^2\Pi) \rightarrow C_3(\Sigma) + H(^2S) \tag{6}$$

and

$$C_3(\Sigma) \rightarrow C_3(\Pi) + h\nu \text{ (bands)},$$

assuming that only a few kilocalories are lost in kinetic energy of separation of the $C_3(\Sigma)$ radical and the H atom. However in view of the similarity between the emission from flame and furnace experiments, it appears probable that (6) does not play a dominant part in the population of the C_3^* state for the luminous mantle of the fuel-rich oxyacetylene flame. The probability

that reaction (6) may be employed to account for the observed C_3 spectra from other laboratory and astrophysical sources cannot be excluded and will be considered in a forthcoming paper.

ACKNOWLEDGMENTS

The author would like to acknowledge a number of discussions with Dr. R. W. Nicholls, as a result of which the above work was undertaken. The research was supported in part by the following agencies whose assistance is gratefully acknowledged: The Defence Research Board of Canada (Grant DRBC 5001-15), The National Research Council of Canada (Capital Grant for the purchase of the spectrometer), The Air Force Cambridge Research Centre (Contract AF 19(604)-1718), and Imperial Oil of Canada.

REFERENCES

BEHRENS, H. 1953. Fourth Symposium on Combustion (Williams & Wilkins Co., Baltimore, Md.), p. 538.
CLUSIUS, K. and DOUGLAS, A. E. 1954. Can. J. Phys. **32**, 319.
DIEDERICHSEN, J. and WOLFHARD, H. G. 1956. Proc. Roy. Soc. A, **236**, 89.
DOUGLAS, A. E. 1951. Astrophys. J. **114**, 466.
FERGUSON, R. E. 1955. J. Chem. Phys. **23**, 2085.
GAYDON, A. G. 1947. Dissociation energies (Chapman & Hall, Ltd., London).
——— 1948. Spectroscopy and combustion theory (Chapman & Hall, Ltd., London).
GOLDFINGER, P. 1955. Mém. soc. roy. sci. Liège, **15**, 378.
KIESS, N. H. and BASS, A. M. 1954. J. Chem. Phys. **22**, 569.
KIESS, N. H. and BROIDA, H. P. 1956. Can. J. Phys. **34**, 1471.
MARR, G. V. 1957. Can. J. Phys. **35**, 1265 (Paper I).
MARR, G. V. and NICHOLLS, R. W. 1955. Can. J. Phys. **33**, 394.
PHILLIPS, J. G. and BREWER, L. 1955. Mém. soc. roy. sci. Liège, **15**, 314.
RÖSSLER, F. and BEHRENS, H. 1950. Optik, **6**, 145.

SPECTRUM OF *L* AUGER ELECTRONS FROM $_{81}Tl^{208}$ AND $_{83}Bi^{212}$ [1]

C. GEOFFRION AND G. NADEAU

ABSTRACT

The spectrum of *L* Auger electrons emitted by a source of Th(B+C+C″) has been measured with a 180° beta-ray spectrometer. An empirical formula for the calculation of secondary ionization potentials has been used for a tentative identification of the transitions giving rise to the measured lines.

INTRODUCTION

The study of Auger spectra has been, until now, the subject of very little experimental work, but recent progress in beta-ray spectrometry makes it possible to obtain important information from these spectra. In particular, data can be derived about secondary ionization potentials, that is, the energy necessary to extract an electron from an atom already ionized in an inner shell. In this work a study has been made of the *L* Auger spectra of bismuth ($Z = 83$) and thallium ($Z = 81$), and an empirical formula has been worked out for the calculation of secondary ionization potentials.

EXPERIMENTAL WORK

The beta-ray spectrometer used in this work has been described by Geoffrion and Giroux (1956). The resolution, as measured on the *I*-line of ThC, was about 0.3%.

The 5.2×0.1 cm. sources were prepared in the usual manner: a very thin Zapon film (about 20 μg./cm.^{2}) was lightly aluminized by vacuum evaporation, and exposed 24 hours at 800 volts to thorium emanation.

The Geiger counter detector was filled with a mixture of 60% argon and 40% propane at 5 cm. Hg pressure. The counter window was of Zapon film from 30 to 50 μg./cm.^{2} thick.

Several runs gave positive identification of 37 *LMM* and *LMN* Auger lines in the region from 5 to 13 kev. A typical spectrum is given in Fig. 1. The short life of the source did not permit measurement of the whole spectrum in sufficient detail in a single run, so that Fig. 1 is in fact the juxtaposition of two partial spectra, which must be taken into consideration in evaluating the relative intensities of the lines. The counter is equipped with an electrostatic accelerator, and a few runs were made with a 5 kev. acceleration to eliminate errors due to absorption by the counter window. These techniques have been described (Giroux and Geoffrion 1956).

The energies of the lines were determined in the following way. The two most intense lines (Nos. 13 and 24 of Fig. 1) were calibrated by linear extra-

[1]Manuscript received July 2, 1957.
Contribution from the Département de Physique, Université Laval, Québec, Que.
This research was supported by the United States Air Force through the Air Force Office of Scientific Research of the Air Research and Development Command, under contract No. AF-18(600)-1574, by the Defence Research Board (Grant No. D.R.B. 9510-13), and by the National Research Council (Grant No. T-45). Reproduction in whole or in part is permitted for any purpose of the United States Government.

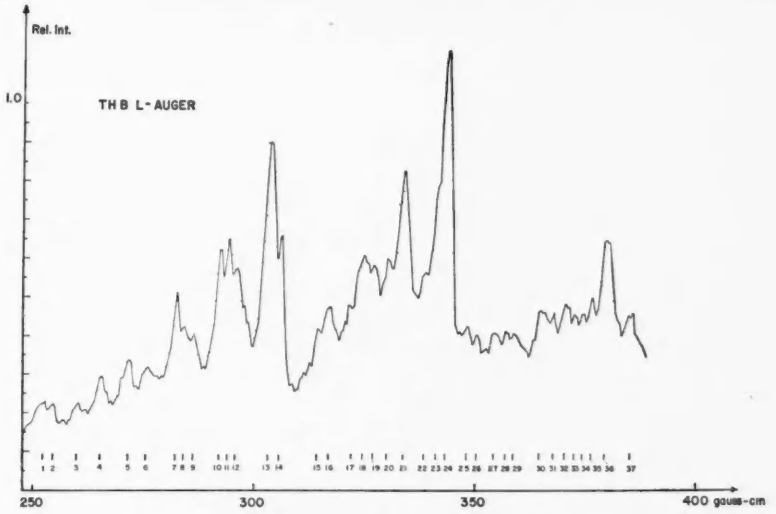

FIG. 1. Spectrum of L Auger electrons from $_{81}Tl^{208}$ and $_{83}Bi^{212}$.

polation from the standard A and I lines, using for these the absolute values of Siegbahn (1955). The results of five independent calibrations are given in Table I. Lines No. 13 and 24 have been attributed to $L_2M_4M_5$ and $L_3M_4M_5$ transitions in bismuth. Their energy difference of 2267 ± 17 ev. compares well with the energy difference of the L_2 and L_3 subshells of bismuth, which is 2292 ev. (Siegbahn 1955).

Then, on each measured spectrum, the energy of the other lines has been calculated by interpolation and extrapolation from lines No. 13 and 24. Each

TABLE I

CALIBRATION OF LINES NO. 13 AND 24

Line		H_r, gauss-cm.	Energy, kev.
I		1753.91 ± 0.14	$222.22\ \pm0.03$
A		534.20 ± 0.06	24.509 ± 0.005
24	I	344.38	
	II	344.47	
	III	344.41	
	IV	344.34	
	V	344.36	
	Average	344.39 ± 0.15	10.325 ± 0.009
13	I	303.80	
	II	303.89	
	III	304.05	
	IV	303.96	
	V	303.84	
	Average	303.91 ± 0.15	8.058 ± 0.008

line has thus been measured from 7 to 10 times, and the consistency of the results indicates a precision of 10 to 20 volts on the energies. The relative intensities have been evaluated from 1 for the weakest lines to 10 for the strongest line. The fact that most of the lines are not completely separated makes probable an error of about 20% on these relative intensities. The experimental results are included in Table III.

IDENTIFICATION OF AUGER TRANSITIONS

The process of emission of an Auger electron is well known. It may be described as follows. First, in some way or another, an atom is ionized in an inner shell V ($V = K$, L, or M). Then an electron from an outer shell X falls into shell V, thereby liberating the energy $(E_V - E_X)$, where E_V and E_X are the energy of primary ionization of the normal atom in shells V and X respectively. This energy, instead of being emitted as an X-ray, is used to extract an electron from shell Y, and give it the kinetic energy associated with this particular Auger transition, which energy can be represented by the symbol E_{VXY}, and will be given by the formula

$$E_{VXY} = E_V - E_X - E_{XY}, \tag{1}$$

where E_{XY} = energy of secondary ionization in shell Y when a primary ionization exists in shell X. The differences $E_V - E_X$ are accurately known from X-ray spectra, so that a measurement of the energies E_{VXY} of Auger electrons can be used to determine the energies E_{XY} of secondary ionizations, provided the transitions VXY have been identified correctly.

Such an identification is comparatively easy for KLL lines, which are only six in number and are generally well separated; but in the case of KLM, KLN, KMM, LMM, LMN, etc. transitions, the great number of possible lines makes the identification quite difficult.

It would be therefore very useful to have a means of calculating the energies of secondary ionizations. Various workers use the formula

$$E^Z_{XY} = E^{Z+1}_Y, \tag{2}$$

where Z is the charge on the nucleus and Y is the outer shell. This was refined (Bergstrom and Hill 1954) by introducing an effective incremental charge ΔZ, so that

$$E^Z_{XY} = E^{Z+\Delta Z}_Y = E^Z_Y + (E^{Z+1}_Y - E^Z_Y)\Delta Z. \tag{3}$$

ΔZ is obtained by experiment and its value will in general depend upon the particular shells X and Y involved in the transition. We suggest an alternative way of calculating secondary ionization energies. Let us write

$$E_{XY} = E_Y + (\Delta E)_{XY}, \tag{4}$$

where $(\Delta E)_{XY}$ = the additional energy necessary for the extraction of a Y electron as a consequence of the atom being already ionized in shell X. As the Auger transitions VXY and VYX start from the same initial state, ionization

in shell V, and end in the same final state, ionization in shells X and Y, we must have

$$E_{VXY} = E_V - E_X - E_Y - (\Delta E)_{XY} = E_{VYX} = E_V - E_Y - E_X - (\Delta E)_{YX}$$

so that

$$(\Delta E)_{XY} = (\Delta E)_{YX}. \tag{5}$$

Any theoretical or empirical formula for the calculation of $(\Delta E)_{XY}$ must be symmetrical with respect to the two concerned shells. It will be noted that this condition is not satisfied by (2) or (3).

Moreover the said formula must only contain quantities already known with sufficient precision, as, for instance, the energies of primary ionization, which can be deduced from X-ray emission lines and absorption discontinuities.

Finally, when X is an internal shell (L, for example) and Y an external one (N or O), we may expect that $(\Delta E)_{XY}$ be more or less equal to $E_Y^{Z+1} - E_Y^Z$, that is to the difference of primary ionization energies in shell Y for an atom of charge $Z+1$ and an atom of charge Z. The absence of an electron in an internal shell must make at the periphery of the atom an effect similar to that of increasing by one the charge of the nucleus.

The following formula is proposed to satisfy these criteria:

$$\left[\frac{1}{(\Delta E)_{XY}^Z}\right]^n = \left[\frac{1}{E_X^{Z+1} - E_X^Z}\right]^n + \left[\frac{1}{E_Y^{Z+1} - E_Y^Z}\right]^n. \tag{6}$$

To make calculations easier, it can be written

$$(\Delta E)_{XY}^Z = (E_Y^{Z+1} - E_Y^Z) \Big/ \left[1 + \left[\frac{E_Y^{Z+1} - E_Y^Z}{E_X^{Z+1} - E_X^Z}\right]^n\right]^{1/n}. \tag{7}$$

If we let n go to infinity we get the formula

$$(\Delta E)_{XY}^Z = E_Y^{Z+1} - E_Y^Z, \tag{8}$$

where Y is the outer shell. This is formula (2). It is clear that it can be good only in the limiting case where X and Y are shells very far apart, and in that case any value of n will give about the same results.

The dependence on the value of n of the results obtained from formula (7) is greatest when X and Y are both L subshells. Accordingly, to determine a convenient value for n, a comparison has been made of energies of KLL Auger electrons from bismuth ($Z = 83$), mercury ($Z = 80$), platinum ($Z = 78$), and silver ($Z = 47$), calculated from (1), (4), and (7) with $n = 1$ and $n = 2$, and the energies measured by Mladjenovic and Slatis (1955), Bergstrom and Hill (1954), Ewan (1957), and Johnson and Foster (1953). The results of Johnson and Foster, based on the value 24459 ev. for the A line of Th C″, have been corrected for the more recent value of 24509 ev. As far as possible K absorption discontinuities were not used in the calculations. Instead the differences $E_K - E_{L_i}$ were taken directly as the energies of $K \rightarrow L_i$ X-ray emission lines. For KL_1L_1 Auger lines, $E_K - E_{L_1}$ was obtained by taking the differences between the energies of $K \rightarrow M_i$ and $L_1 \rightarrow M_i$ lines. For mercury data are lacking on K lines, and K absorption discontinuity had to be used, with a decrease in accuracy. The tables of Cauchois and Hulubei (1947) were

used for emission lines, and those of Hill, Church, and Mihelich (1952) for absorption energies. The results of the comparison between these calculations and measurements are shown in Table II. In the case of KL_2L_2, KL_1L_3, KL_2L_3, and KL_3L_3 lines, the exponent $n = 2$ seems to be favored. The evidence is not so simple for KL_1L_1 and KL_1L_2 lines, but we must consider that the measurements of Mladjenovic and Slatis, and Bergstrom and Hill, which have a better precision than any other made until now, are definitely in favor of $n = 1$. So it seems that the choice of the exponent n must depend on the kind of subshells involved in the Auger transition.

TABLE II

COMPARISON OF EXPERIMENTAL RESULTS WITH CALCULATIONS USING FORMULA (7)

Auger transition		Energy (kev.)			
		Measured		Calculated	
				$n = 1$	$n = 2$
$_{83}Bi^{212}$	KL_1L_1	57.466	±0.020	57.477	57.365
	KL_1L_2	58.186		58.159	58.059
	KL_1L_3	60.417		60.490	60.399
	KL_2L_3	61.090		61.171	61.081
	KL_3L_3	63.404		63.491	63.409
$_{80}Hg$	KL_1L_1	53.18	±0.04	53.17	53.07
	KL_1L_2	53.79		53.80	53.69
	KL_2L_2	54.32		54.44	54.34
	KL_1L_3	55.71		55.77	55.68
	KL_2L_3	56.35		56.40	56.31
	KL_3L_3	58.27		58.35	58.28
$_{78}Pt^{193}$	KL_1L_1	50.35		50.407	50.305
	KL_1L_2	51.06		51.009	50.916
	KL_1L_3	52.68		52.754	52.671
	KL_2L_2	53.28		53.362	53.278
	KL_3L_3	55.03		55.093	55.018
$_{47}Ag^{107}$	KL_1L_1	17.74	±0.06	17.784	17.745
	KL_1L_2	18.02		18.066	18.028
	KL_1L_3	18.18		18.243	18.207
	KL_2L_2	18.29		18.349	18.311
	KL_2L_3	18.46		18.526	18.490
	KL_3L_3	18.65		18.702	18.667

More numerous and more precise measurements will be needed before one can estimate the practical value of formula (7).

The value $n = 2$ was adopted for the calculation of L Auger electron energies appearing in Table III under the heading "Calculated energies". The reason for this choice is only that it seemed to give a better fit than any other value between measured and calculated energies. In addition to these calculated energies, some consideration must be given to the relative distribution of primary ionizations in L_1, L_2, and L_3 subshells, after allowing for possible Coster-Kronig transitions. Table III gives the experimental results, a proposed identification, the calculated energies, and a comparison with recent measurements made by Burde and Cohen (1956) and Bellicard and Moussa (1956) on the same spectra.

TABLE III

L AUGER ELECTRONS IN THALLIUM AND BISMUTH

This work						Burde and Cohen				Bellicard and Moussa			
Measures			Identification			Measures		Identification		Measures		Identification	
Line No.	Energy, kev.	Rel. int.	Z	Transition	Calc. en., kev.	Line	Energy, kev.	Z	Transition	Line	Energy, kev.	Z	Transition
						A_1	5.48	81	$L_3M_1M_2$				
1	5.623	1	83	$L_3M_1M_2$	5.618	A_1'	5.66	83	$L_3M_1M_2$				
2	5.727	1	81	$L_3M_2M_2$	5.725								
3	5.893	1	81	$L_3M_1M_3$	5.908	A_2	5.95	81	$L_3M_1M_3$				
			83	$L_3M_2M_2$	5.920								
						A_2'	6.18	83	$L_3M_1M_3$				
4	6.286	2	81	$L_3M_2M_3$	6.198	A_3	6.18	81	$L_3M_2M_3$	*a*	6.150	81	$L_3M_2M_3$
			81	$L_3M_1M_4$	6.387								
5	6.463	2	83	$L_3M_2M_3$	6.455	A_3'	6.44	83	$L_3M_2M_3$	*b*	6.435	83	$L_3M_2M_3$
6	6.654	1	83	$L_3M_1M_4$	6.644								
			81	$L_3M_2M_4$	6.676	A_4	6.65	81	$L_3M_2M_4$				
			81	$L_3M_3M_3$	6.669						6.615	81	$L_3M_3M_3$
										c	6.735	81	$L_3M_3M_4$
7	6.990	6	83	$L_3M_2M_4$	6.950	A_4'	7.02	83	$L_3M_2M_4$	*d*	6.980	83	$L_3M_2M_4$
			83	$L_3M_3M_3$	6.985								
8	7.101	3	83	$L_3M_2M_3$	7.060								
			81	$L_3M_3M_4$	7.145	A_5	7.14	81	$L_3M_3M_4$				
9	7.185	3	81	$L_2M_1M_1$	7.187								
10	7.487	6	83	$L_3M_3M_4$	7.478	A_5'	7.49	83	$L_3M_3M_4$				
			81	$L_2M_1M_2$	7.477								
11	7.603	6	83	$L_3M_3M_5$	7.588						7.540	83	$L_3M_3M_5$
			83	$L_2M_1M_1$	7.603								
			81	$L_3M_4M_4$	7.620	A_6	7.62	81	$L_3M_4M_4$				
12	7.708	5	81	$L_3M_4M_5$	7.721					*e*	7.640	81	$L_3M_4M_5$
13	8.058	9	83	$L_3M_4M_5$	8.079	A_6'	8.05	83	$L_3M_4M_4$	*f*	8.040	83	$L_3M_4M_5$
14	8.173	3	83	$L_3M_3M_5$	8.189						8.145	83	$L_3M_3M_5$
			83	$L_2M_2M_2$	8.212								
			81	$L_2M_2M_3$	8.240	B_1	8.14	81	$L_2M_2M_3$				
15	8.617	1	81	$L_1M_1M_3$	8.600								
											8.670	81	$L_2M_3M_3$
16	8.747	4	81	$L_2M_3M_3$	8.711								
			81	$L_2M_2M_4$	8.718	B_2	8.60	81	$L_2M_2M_4$				
			83	$L_2M_2M_3$	8.747	B_1'	8.71	83	$L_2M_3M_3$	*g*	8.720	83	$L_2M_2M_3$
17	9.006	1	83	$L_2M_1M_5$	9.046						8.960	83	$L_2M_1M_5$
						C_1	9.06	81	$L_1M_1M_4$				
18	9.233	6	83	$L_2M_2M_4$	9.242	B_2'	9.28	83	$L_2M_1M_4$		9.200	83	$L_2M_2M_4$
19	9.324	5	83	$L_2M_2M_5$	9.352					*h*	9.305	83	$L_2M_2M_5$
			81	$L_1M_2M_3$	9.360								
20	9.520	3	81	$L_2M_3N_2$	9.513								
			81	$L_2M_4N_2$	9.536								
			83	$L_2M_3N_2$	9.540								
			83	$L_2M_2N_{6,7}$	9.544								
						C_1'	9.68	83	$L_1M_1M_4$				
21	9.739	7	81	$L_2M_4N_{4,5}$	9.751	A_7	9.68	81	$L_2M_4N_{4,5}$				
			81	$L_2M_4M_5$	9.763								
			83	$L_2M_3M_4$	9.770						9.735	83	$L_2M_3M_4$
22	10.021	2	83	$L_1M_2M_5$	10.029								
			81	$L_2M_4N_{6,7}$	10.037								
23	10.238	2	83	$L_2M_4N_{4,5}$	10.250	A_7'	10.21	83	$L_2M_4N_{4,5}$				
			83	$L_2M_4M_4$	10.261						10.260	83	$L_2M_4M_4$
24	10.325	10	83	$L_2M_4M_5$	10.371					*i*	10.340	83	$L_2M_4M_5$
						C_2	10.27	81	$L_1M_4M_4$				
25	10.641	1	83	$L_2M_3N_{6,7}$	10.664								
			81	$L_2M_2N_2$	10.642								
						C_2'	10.7	83	$L_1M_4M_4$				
26	10.767	1	83	$L_2M_1N_1$	10.725								
			81	$L_1M_1N_1$	10.752								
27	11.062	1	83	$L_1M_4M_5$	11.048								
						B_3	11.02	81	$L_2M_2N_2$				
28	11.169	1	83	$L_1M_5M_5$	11.158								
						B_3'	11.2	83	$L_2M_1N_{4,5}$				
29	11.326	1	83	$L_2M_2N_2$	11.303								
			81	$L_2M_2N_{4,5}$	11.321								
			81	$L_2M_4N_1$	11.326								
						B_4	11.52	81	$L_2M_4N_2$				
30	11.543	2	83	$L_2M_1N_{6,7}$	11.531								
			83	$L_2M_2N_{4,5}$	11.534								
			81	$L_2M_3N_2$	11.555								
			81	$L_2M_4N_3$	11.578					*j*	11.515	81	$L_2M_4N_3$
31	11.654	1	81	$L_2M_3N_2$	11.673								
			83	$L_2M_2N_2$	11.698	B_4'	11.65	83	$L_2M_3N_2$				
32	11.827	2	81	$L_2M_4N_{4,5}$	11.793								
			83	$L_2M_2N_2$	11.832								
			83	$L_2M_2N_{6,7}$	11.836								
33	11.954	1	81	$L_2M_3N_{4,5}$	11.889	B_5	11.93	81	$L_2M_3N_{4,5}$				
34	12.114	1	81	$L_2M_4N_{6,7}$	12.080								
35	12.214	2	81	$L_2M_3N_{6,7}$	12.175								
			83	$L_2M_4N_2$	12.176	B_5'	12.22	83	$L_2M_4N_2$				
										k	12.260	83	$L_2M_4N_3$
36	12.459	4	81	$L_1M_4N_{4,5}$	12.442	C_3	12.42	81	$L_1M_4N_{4,5}$				
						B_6'	12.61	82	$L_2M_4N_{4,5}$		12.500	83	$L_2M_4N_4$
37	12.813	2	83	$L_2M_4N_{6,7}$	12.846								

DISCUSSION

Except for a few isolated cases, it has been impossible to assign a single Auger transition to each measured line. This is due in part to the fact that the two spectra of thallium and bismuth are superimposed. Burde and Cohen used an alpha-coincidence method to measure only the spectrum of thallium, and then obtained the spectrum of bismuth by difference. In that way they could, with a resolution of only 1.2%, detect 30 lines, 15 in each spectrum. Bellicard and Moussa reported only 20 lines in the composite spectrum.

Concerning the spectrum of thallium, Burde and Cohen pointed out that consideration must be given to the fact that thallium nuclei suffer a recoil as a result of the emission of an α-particle. In their α-coincident arrangement, Burde and Cohen selected recoil nuclei leaving the source into the vacuum, and therefore the coincident spectrum that they obtained showed increased energies and had to be corrected accordingly. In our case we measure all Auger electrons emitted in a given direction from the source. About half of them will have increased energies, corresponding to recoil nuclei moving away from the source backing, and the other half will have reduced energies, corresponding to electron emission from nuclei at rest after having penetrated the source. As a result there is a broadening of the lines and possibly a shift in energy. A comparison between lines attributed to thallium and lines attributed to bismuth shows that the broadening due to recoil is quite small, and consequently the energy shift is negligible compared to the experimental error in energy determination.

Table III shows that our results are only partly concordant with those of Burde and Cohen and those of Bellicard and Moussa. A major discrepancy is in the identification of the strongest lines (our Nos. 13 and 24, Burde and Cohen's A_6' and A_7', Bellicard and Moussa's f and i). Burde and Cohen assign them to Auger transitions $L_3M_4M_4$ and $L_3M_4N_{4,5}$ in bismuth, while, as do Bellicard and Moussa, we assign them to transitions $L_3M_4M_5$ and $L_2M_4M_5$ in bismuth. An argument in favor of this attribution is the fact already mentioned that the measured energy difference of 2267 ev. of these two lines is quite near the difference of 2292 ev. between subshells L_2 and L_3 of bismuth. Moreover the same Auger transitions were detected for thallium, with a measured energy difference of 2031 ev. compared to an energy difference of 2042 ev. between the L_2 and L_3 subshells of thallium.

More precise measurements, made with a better resolution and a thinner source backing, would make possible the separation of a greater number of lines and a better identification of the Auger transitions. Thus we could get a sounder appraisal of the value of the empirical formula proposed for the calculation of energies of secondary ionization.

REFERENCES

BELLICARD, J. B. and MOUSSA, A. 1956. Compt. rend. **242**, 1156.
BERGSTROM, I. and HILL, R. D. 1954. Arkiv Fysik, **8**, 21.
BURDE, J. and COHEN, S. G. 1956. Phys. Rev. **104**, 1085.
CAUCHOIS, Y. and HULUBEI, H. 1947. Longueurs d'onde des émissions X et des discontinuités d'absorption X (Hermann & Cie, Paris).

EWAN, G. T. 1957. Can. J. Phys. **35**, 672.
GEOFFRION, C. and GIROUX, G. 1956. Can. J. Phys. **34**, 920.
GIROUX, G. and GEOFFRION, C. 1956. Can. J. Phys. **34**, 153.
HILL, R. D., CHURCH, E. L., and MIHELICH, J. W. 1952. Rev. Sci. Instr. **23**, 523.
JOHNSON, F. A. and FOSTER, J. S. 1953. Can. J. Phys. **31**, 469.
MLADJENOVIC, M. and SLATIS, H. 1955. Arkiv Fysik, **9**, 45.
SIEGBAHN, K. 1955. Beta- and gamma-ray spectroscopy (North-Holland Publ. Co., Amsterdam), p. 920.

ON FOCUSING ELECTROMAGNETIC RADIATORS[1]

ROBERT W. BICKMORE

ABSTRACT

The transmission of electromagnetic energy between two apertures is examined as a function of their sizes, separation, excitation functions, and surface shapes with Fresnel approximations made throughout. Relations are derived which show when it is advantageous to focus the apertures by curving about a spherical surface.

I. INTRODUCTION

The conventional form of a coherent electromagnetic radiator can be considered as an aperture focused on infinity. Just as optical photography has benefited by variable focus instruments, so also can certain microwave systems such as high-resolution radar (Tetelbaum 1946).

Prior to the employment of extremely large apertures, it was sufficient to ignore the focusing of microwave radiation. However, recent developments require the operation, and perhaps the measurement, of antennas well within the "far-zone criterion" of $2L^2/\lambda$.

It is the purpose of this paper to establish a focusing criterion and to indicate how the loss in gain and resolution which normally attends "near-zone" operation may be eliminated.

II. TRANSMISSION BETWEEN TWO ARRAYS

Consider two identically polarized antenna elements dS_1 and dS_2 as elements of two apertures, S_1 and S_2, shown in Fig. 1. Let dS_2 be an absorber and

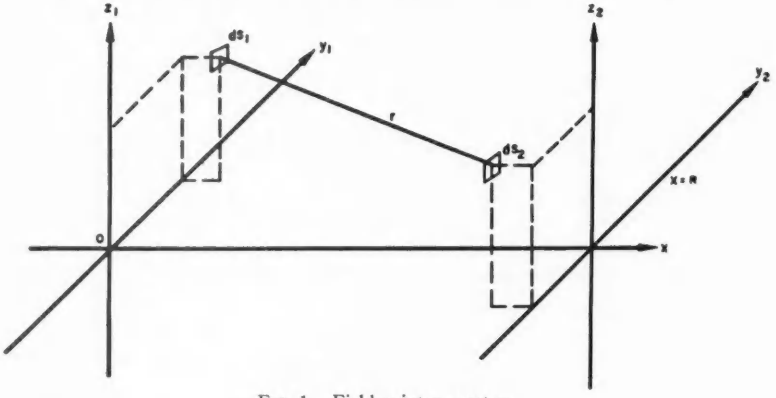

FIG. 1. Field point geometry.

[1]Manuscript received July 31, 1957.
Contribution from Research Laboratories, Hughes Aircraft Company, Culver City, California.
The work described in this report was sponsored by the Air Force Cambridge Research Center under Contract AF 19(604)-1317.

dS_1 be a source of monochromatic radiation with time dependence $e^{j\omega t}$. Then the current induced in dS_2 by dS_1 is

$$dI = \frac{E_0 F_1 F_2}{Z} \frac{e^{-jkr}}{r} dS_1\, dS_2,$$

where Z = impedance of dS_2,
$k = 2\pi/\lambda$,
λ = wavelength,

neglecting induction fields (that is, $1/r << 2\pi/\lambda$). F_1 and F_2 are the element factors of dS_1 and dS_2, respectively. Let r be great enough so that F_1 and F_2 are essentially constant over the apertures; then, the total induced current is

$$(1) \qquad I = \frac{E_0 F_1 F_2}{Z} \int_{S_1} \int_{S_2} f_1(y_1, z_1)\, f_2(y_2, z_2) \frac{e^{-jkr}}{r} dS_1\, dS_2,$$

where f_1 and f_2 are the aperture distribution functions. By the geometry of Fig. 1,

$$r^2 = (x_2 - x_1)^2 \left[1 + \frac{(y_2 - y_1)^2 + (z_2 - z_1)^2}{(x_2 - x_1)^2} \right].$$

Making the usual Fresnel approximations,

$r \approx R$ in the amplitude factor and

$$r \approx (x_2 - x_1) \left[1 + \frac{(y_2 - y_1)^2 + (z_2 - z_1)^2}{2(x_2 - x_1)^2} \right] \text{ in the phase factor.}$$

At this point it is logical to attempt a maximization of the resulting integral

$$I = \frac{E_0 F_1 F_2}{ZR} \int_{S_1} \int_{S_2} f_1 f_2\, e^{-jkr} dS_1\, dS_2.$$

By the Cauchy inequality,

$$\left| \int f(z)\, dz \right| \leqslant \int |f(z)|\, dz.$$

Therefore,

$$|I| \leqslant \left| \frac{E_0 F_1 F_2}{ZR} \right| \int_{S_1} \int_{S_2} |f_1 f_2| dS_1\, dS_2.$$

The equals sign will apply only when the variation of r with the variables of integration is zero or when the phase variation of the product $f_1 f_2$ exactly complements the factor e^{-jkr}. Since this is impossible for any pair of finite arrays, a more subtle method must be used to make I a maximum. While it is obvious that a quadratic phase term in the product $f_1 f_2$ will maximize I for plane, parallel apertures, a more interesting and useful solution is obtained by letting the product $f_1 f_2$ be real and allowing the shape of the aperture surface to vary.* This is done as follows:

*For line sources, a combination of electrical and mechanical focusing may be desirable to control the shape of the focal line (Bickmore 1954, 1955).

Let $x = x_1(y_1, z_1)$ and $x = x_2(y_2, z_2)$ be the surfaces making $I = I_{\max}$. For other possible surfaces

$$x = x_1(y_1, z_1)+\epsilon_1\eta_1(y_1, z_1) \qquad \text{and } x = x_2(y_2, z_2)+\epsilon_2\eta_2(y_2, z_2)$$

with

$$\eta_1(0, 0) = \eta_2(0, 0) = 0 \tag{2}$$

and

$$x_1(0, 0) = 0, \qquad x_2(0, 0) = R.$$

$I = I_{\max}$ when $\epsilon_1 = \epsilon_2 = 0$.

Let us define

$$\Phi(\epsilon_1, \epsilon_2) = \int_{S_1}\int_{S_2} f_1 f_2\, e^{-jkr}\, dS_1\, dS_2.$$

A necessary condition for $I = I_{\max}$ is that $\Phi'(0, 0) = 0$; it is also a sufficient condition provided that the integral has been maximized rather than minimized.

$$\frac{\partial\Phi(0, 0)}{\partial\epsilon_1} = -jk\int_{S_1}\int_{S_2} f_1 f_2\eta_1 \frac{\partial r}{\partial x_1}\, e^{-jkr}\, dS_1\, dS_2$$

$$\frac{\partial\Phi(0, 0)}{\partial\epsilon_2} = -jk\int_{S_1}\int_{S_2} f_1 f_2\eta_2 \frac{\partial r}{\partial x_2}\, e^{-jkr}\, dS_1\, dS_2$$

Since $\Phi'(0, 0) = 0$ for all η_1 and η_2, a pair of "Euler equations" follows:

$$\int_{S_1} f_1 \frac{\partial r}{\partial x_2}\, e^{-jkr}\, dS_1 = 0, \qquad \int_{S_2} f_2 \frac{\partial r}{\partial x_1}\, e^{-jkr}\, dS_2 = 0.$$

If both integrals are over a finite area, the only solutions are

$$x_1 = \text{constant} = 0,$$

$$x_2 = \text{constant} = R.$$

These solutions indicate that the optimum condition is in general two *plane* arrays.

However, if *either* array is such that it may be regarded as a point source relative to the other array, the solution must be

$$\partial r/\partial x_1 = 0 \qquad \text{or } \partial r/\partial x_2 = 0.$$

Integrating and applying the conditions given in (2) yields

$$x_1^2+y_1^2+z_1^2 = 2x_1R \qquad \text{or } x_2^2+y_2^2+z_2^2 = R^2.$$

These are spherical surfaces, each of radius R. S_1 is centered at $(R, 0, 0)$ and S_2 is centered at the origin.

It remains to determine the region in which each type of solution is valid.

III. FOCUSING CRITERION

In order to choose between a plane aperture and a focused (i.e., spherical solution) aperture, it is necessary to ascertain the value of R at which the two solutions are equivalent, that is, the value of R at which either aperture may be considered a point source.

Let the ratio of total induced current in the spherical aperture to the total induced current in the plane aperture be

$$\gamma = I_s/I = \left| \frac{\int_{S_1}\int_{S_2} f_1 f_2 \exp[jk/R(y_1y_2+z_1z_2)] \exp[jkx_1(x_2-R)/R]\, dS_1\, dS_2}{\int_{S_1}\int_{S_2} f_1 f_2 \exp[-jk\{(y_2-y_1)^2+(z_2-z_1)^2\}/2R]\, dS_1\, dS_2} \right| .$$

No generality is lost by taking $S_1 > S_2$ and letting S_2 be the point source. Then $x_2 = R$, $y_2 = z_2 = 0$, and

$$\gamma = \left| \frac{\int_{S_1} f_1\, dS_1}{\int_{S_1} f_1 \exp[-jk/2R(y_1^2+z_1^2)]\, dS_1} \right| .$$

Setting $\gamma = 1$ results in the correct but impractical solution $R = \infty$, because the effect of Fresnel diffraction does not suddenly end but carries to infinity. However, the effect of Fresnel diffraction is generally considered to be negligible beyond the last oscillation of the Fresnel function. This is equivalent to substituting, for the Fresnel integral, its asymptotic value. The result is an expression for transitional $R = R_0$,

$$R_0 = \left| \frac{\frac{1}{2}\lambda \int_{-\infty}^{\infty}\int_{-\infty}^{\infty} f(u,v) \exp[-j\pi/2(u^2+v^2)]\, du\, dv}{\int_{-\eta_1}^{\eta_1}\int_{-\xi_1}^{\xi_1} f(\xi,\eta)\, d\xi\, d\eta} \right| \tag{3}$$

where $u = y\sqrt{(2/\lambda R_0)}$, $v = z\sqrt{(2/\lambda R_0)}$, $\xi = y/R_0$, $\eta = z/R_0$, $\xi_1 = L_\xi/2R$, and $\eta_1 = L_\eta/2R$.

For the case $f = 1$, it is easily found that $R_0 = L^2/\lambda$ is the focusing criterion and coincides with the generally accepted transition point between the Fresnel and Fraunhofer regions of a uniformly illuminated aperture.

It is now evident that, when Equation (3) is applied to the two-aperture problem, a pair of points, R_1 and R_2, is found, corresponding respectively to S_1 and S_2. It is in the region between these two points that one of the spherical solutions applies. If the separation is less than the smaller value, the plane solution applies. If the separation is greater than the larger value, *both* apertures approximate point sources and the two solutions coincide.

The quantity γ is the voltage gain of the focused aperture relative to the plane aperture. For the special but important case of two square apertures with $f_1 = f_2 = 1$, it can easily be found that

$$\gamma = 4(\lambda/\pi)^2 R^2\, \mathrm{Si}^2(\pi\alpha_1\alpha_2)/(\bar{C}^2+\bar{S}^2),$$

where $\mathrm{Si}(x)$ = Sine integral, $\alpha_1 = \sqrt{(L_1^2/2\lambda R)}$, and $\alpha_2 = \sqrt{(L_2^2/2\lambda R)}$. $\bar{C}$

and $\bar{S}$ are modified Fresnel functions as defined in the Appendix.

For a linear array looking at a point, and $f_1 = 1$,

$$\gamma = \sqrt{\tfrac{1}{2}\pi}\,\frac{\alpha}{[C^2(\alpha\sqrt{\tfrac{1}{2}\pi})+S^2(\alpha\sqrt{\tfrac{1}{2}\pi})]^{1/2}},$$

where $$C(x) = \int_0^x \cos t^2\,dt, \qquad S(x) = \int_0^x \sin t^2\,dt.$$

Using the asymptotic values for C and S gives the approximate expression $\gamma = L^2/\lambda R$, which illustrates the afore-mentioned focusing criterion at the point where $\gamma = 1$.

Fig. 2 shows γ for a square aperture looking at a point with $f = 1$ plotted against the quantity $\sqrt{(L^2/2\lambda R)}$. This curve becomes γ^2 for the corresponding linear array.

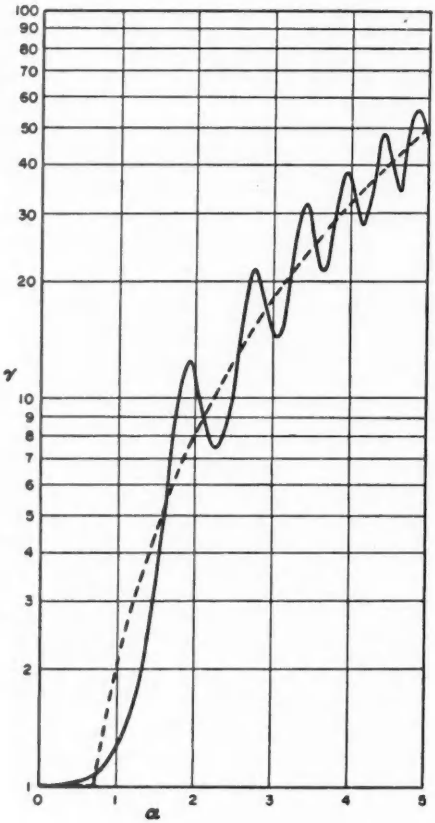

FIG. 2. γ versus α.

IV. INTERPRETATION OF FOCUSING CRITERION

It has been assumed that the point defined by approximate $\gamma = 1$ is that point at which intensity degradation begins as the point comes from infinity toward a fixed plane aperture. The equivalence between this distance from the aperture and the familiar hyperfocal distance in optics can be demonstrated as follows.

Consider the equations for depth of focus

$$\Delta R_{\pm} = R^2 \tan \theta / L \pm R \tan \theta, \qquad L \geqslant R \tan \theta,$$

and

$$\Delta R_{-} = \infty, \qquad L \leqslant R \tan \theta,$$

where $R - \Delta R_{+}$ is the near limit, $R + \Delta R_{-}$ is the far limit, and θ is the angular intercept of the circle of confusion. Taking θ as the beam width of the aperture gives $\tan \theta \approx L/R_0$. The solutions $\Delta R_{+} = \frac{1}{2}R_0$ and $\Delta R_{-} = \infty$ confirm the result that R_0 is the hyperfocal distance.

The equations for optical depth of focus can now be restated for the electromagnetic aperture and become

$$\Delta(R/\lambda)_{\pm} = (R/\lambda)/[(L^2/\lambda R) \pm 1], \qquad L^2/\lambda R \geqslant 1,$$

and

$$\Delta(R/\lambda)_{-} = \infty, \qquad L^2/\lambda R \leqslant 1.$$

Further, since the gain of a radiating aperture is approximately $G = 4\pi/\theta^2$, the ratio of the gain of a focused aperture to that of a plane aperture is given by

$$G_s/G = (\theta/\theta_s)^2.$$

But

$$G_s/G = (I_s/I)^2 = \gamma^2.$$

Therefore, $\theta = \gamma\theta_s$ represents the decrease in resolution caused by a failure to focus a plane array.

V. FOCUSING GEOMETRY

Fig. 3 shows a portion of a curved array. The distance that the center must be deflected is measured by d. For large apertures

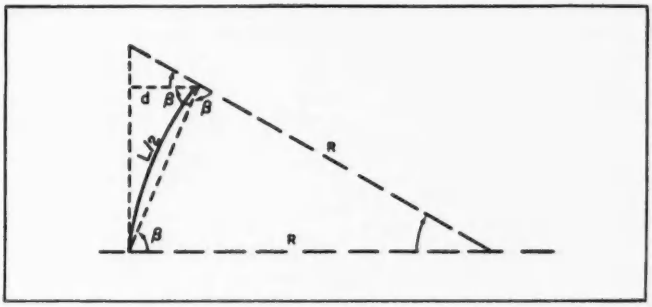

FIG. 3. Geometry of a curved array.

$$d \simeq (L/2)\cos\beta \qquad \text{and } \cos\beta \simeq \sin(L/4R).$$

Consequently, $d \simeq L^2/8R$ is an excellent approximation for arrays large enough to make focusing advantageous.

APPENDIX ON FRESNEL FUNCTIONS

The integrals involved in Section II take on the form (Tetelbaum 1945)

$$I = \int_{-l_\psi}^{l_\psi}\int_{-l_x}^{l_x}\int_{-l_\eta}^{l_\eta}\int_{-l_y}^{l_y} \exp[-jk(y-\eta)^2/2R]\exp[-jk(z-\psi)^2/2R]\,dy\,d\eta\,dz\,d\psi$$

$$= [\bar{C}_{y\eta}\bar{C}_{z\xi} - \bar{S}_{y\eta}\bar{S}_{z\xi}] - j[\bar{S}_{y\eta}\bar{C}_{z\xi} + \bar{S}_{z\xi}\bar{C}_{y\eta}],$$

where

$$\bar{C}_{x\delta} = \frac{2(l_x+l_\delta)}{\sqrt{K}}\,C[\sqrt{K}(l_x+l_\delta)] - \frac{2(l_x-l_\delta)}{\sqrt{K}}\,C[\sqrt{K}(l_x-l_\delta)]$$

$$- \frac{1}{K}[\sin K(l_x+l_\delta)^2 - \sin K(l_x-l_\delta)^2],$$

$$\bar{S}_{x\delta} = \frac{2(l_x+l_\delta)}{\sqrt{K}}\,S[\sqrt{K}(l_x+l_\delta)] - \frac{2(l_x-l_\delta)}{\sqrt{K}}\,S[\sqrt{K}(l_x-l_\delta)]$$

$$+ \frac{1}{K}[\cos K(l_x+l_\delta)^2 - \cos K(l_x-l_\delta)^2];$$

$$K = \pi/\lambda R, \quad l = L/2, \quad C(x) = \int_0^x \cos t^2\,dt, \quad S(x) = \int_0^x \sin t^2\,dt.$$

The latter functions are tabulated in several references (Jahnke and Emde 1945).

REFERENCES

Bickmore, R. W. 1954. A focusing criterion for rectangular apertures. Technical Memorandum No. 376, Hughes Aircraft Company, Culver City, Calif.

——— 1955. On the transmission between two rectangular apertures. Scientific Report No. 1, Hughes Aircraft Company, Culver City, Calif.

Jahnke, E. and Emde, F. 1945. Tables of functions (Dover Publications, New York).

Tetelbaum, S. 1945. J. Phys. U.S.S.R. **9**, 505.

——— 1946. J. Phys. U.S.S.R. **10**, 285.

FRAUNHOFER PATTERN MEASUREMENT IN THE FRESNEL REGION[1]

ROBERT W. BICKMORE

ABSTRACT

A method of Fraunhofer pattern measurement is presented by which the distance between antennas may be reduced from the usual $2L^2/\lambda$ to values of the order of $0.1(L^2/\lambda)$. This reduction may be applied to any antenna in which the aperture plane may be physically molded about a spherical surface having a radius of curvature less than $2L^2/\lambda$. It is shown that such measurements have less inherent phase error in the region of the main lobe than the conventional measurements on a plane aperture at $2L^2/\lambda$.

I. INTRODUCTION

Measurement of the Fraunhofer pattern of any aperture has always involved probing the field at a constant radius far enough away so that the aperture approximates a point source. The degree of approximation is perfectly arbitrary, a typical criterion (Silver 1949) being that distance at which a maximum phase error of $\lambda/16$ occurs over the aperture plane. This criterion results in the familiar $R = 2L^2/\lambda$ for a uniformly phased aperture in the field of a point source. Modifications of this rule, too numerous to mention, have appeared in the literature quite frequently.

Recent work at Hughes Aircraft Company (Bickmore 1957) on focused arrays has resulted in a more general expression for a "focusing criterion", which is considered to be the Fresnel–Fraunhofer transition point. This expression takes into account aperture size as well as excitation function. The criterion is still arbitrary in the sense that the actual transition is gradual rather than abrupt; however, it is derived on a sounder mathematical basis than arbitrarily assigning a maximum tolerable phase error.

Unfortunately, the finer details of the Fresnel–Fraunhofer transition must remain of purely academic interest to one faced with the problem of measuring the Fraunhofer pattern of a typical high-resolution array, say 1000 wavelengths long at $\lambda = 4.3$ mm. For such an antenna, $2L^2/\lambda$ becomes *5.35 miles*. From accepted siting procedure (Silver 1949), it is evident that the sites must be quite high to provide an obstacle-free path. In addition, the companion antenna must be large enough to avoid an overly wide beam and also to provide a considerable amount of gain, but must not be large compared with the antenna being tested. The added requirement that the range be flexible enough for use with various high-resolution arrays in the millimeter wave region makes the problem quite formidable and the answer at best inconvenient and expensive.

[1]Manuscript received July 31, 1957.
Contribution from Research Laboratories, Hughes Aircraft Company, Culver City, California.
The work described in this report was supported by the Air Force under Contract AF 19(604)-1317.

An alternative solution is therefore sought now that high-resolution arrays are becoming commonplace.

II. ALTERNATIVE METHODS

The alternatives to measurement of the Fraunhofer pattern in the Fraunhofer region appear to be as follows:

(1) Measurement of the Fresnel pattern (Barrar and Wilcox 1955).
(2) Calculation of the Fraunhofer pattern from measurements in the Fresnel region.
(3) Extension of the Fraunhofer region by focusing the aperture at a point other than infinity.

The first method has the great disadvantage that the pattern is a function of the distance from the antenna and is, therefore, not a unique specification. The second method involves a difficult transition from the Fresnel to the Fraunhofer pattern since the required phase and amplitude measurements are almost impossible to perform with existing equipment. Retention of the Fraunhofer pattern as a means of pattern specification appears to be almost mandatory, at least at the present time. Hence, the possibility of obtaining a true Fraunhofer diffraction pattern in the Fresnel region by means of focusing offers a solution applicable to many types of arrays.

III. FRESNEL FIELD OF A FOCUSED APERTURE

It has been shown (Bickmore 1957) that the field intensity, at any point $P(x_2, y_2, z_2)$, produced by an aperture which has been molded about a concave spherical surface is given by

$$U_p = F\frac{\exp[-jkR]}{R}\int_s f \exp\left[jk\frac{x_1(x_2-R)}{R}\right]\exp\left[j\frac{k}{R}(y_1y_2+z_1z_2)\right]dS$$

where

F = element factor,
f = excitation function of the aperture,
k = $2\pi/\lambda$,
λ = wavelength,
$e^{j\omega t}$ = time dependence.

The geometry is shown in Fig. 1.

The term $\exp[jkx_1(x_2-R)/R]$ is an aberration term and is the factor by which U_p differs from the true Fraunhofer pattern within the limit of the Fresnel approximation. From Fig. 2 it can be seen that $x_{1\,\max} \simeq L^2/8R$, since x_1 is usually small; and $(x_2-R) = -R\sin\phi\tan\phi/2$ in any principal pattern plane.

Consequently, $|kx_1(x_2-R)/R| \leqslant (k/R)(L^2/8R)(R\sin\phi\tan\phi/2)$. Letting $R = KL^2/\lambda$,

$$\left|\frac{kx_1(x_2-R)}{R}\right| \leqslant \frac{\pi\sin\phi\tan\phi/2}{4K}.$$

If the maximum permissible phase error is taken as $\lambda/16$ so that these

measurements are *at least* as good as the measurements at $R = 2L^2/\lambda$, then $K_{\min} = 2 \sin \phi \tan \phi/2$. Thus, the value of K depends on how much of the Fraunhofer pattern it is desired to measure within the specified error.

It can be noted that the phase error as a function of ϕ is zero at $\phi = 0$ and increases to a maximum at $\phi = \pm\pi/2$* while in the case of a plane aperture the phase error is maximum at $\phi = 0$ and decreases to zero at $\phi = \pm\pi/2$. Thus, the focusing technique gives minimum error in the vicinity of the main lobe where accuracy is most desirable.

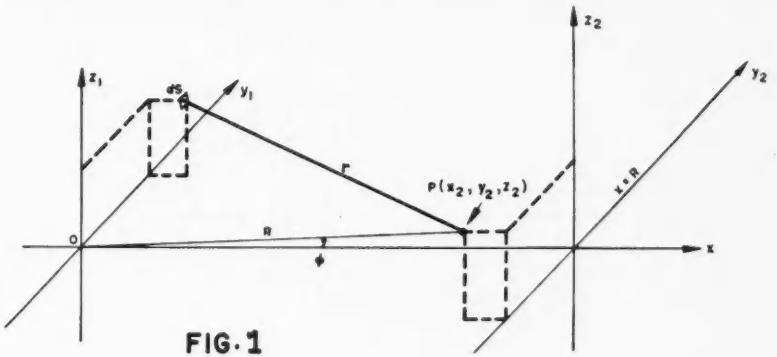

FIG. 1

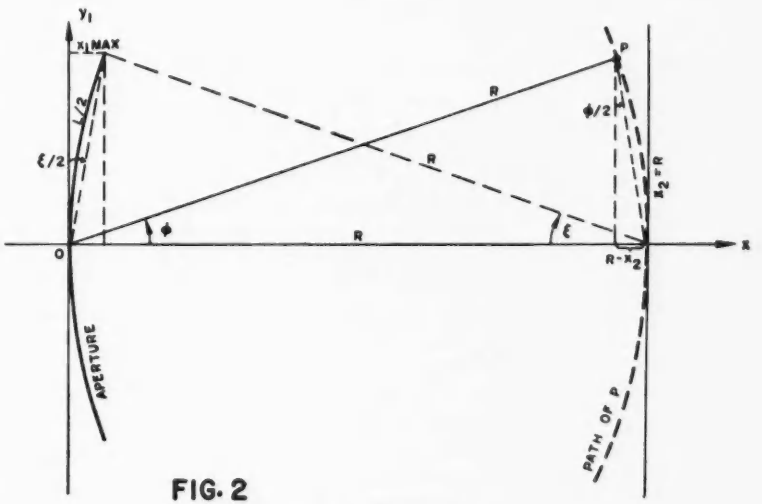

FIG. 2

FIG. 1. Field point geometry.
FIG. 2. Aperture geometry.

*For $\phi > \pi/2$ the array is assumed to have a negative radius of curvature.

For high-resolution antennas, a few degrees either side of the main lobe is usually sufficient to include several side lobes. $K_{\min}$ versus $\phi_{\max}$ is plotted in Fig. 3.

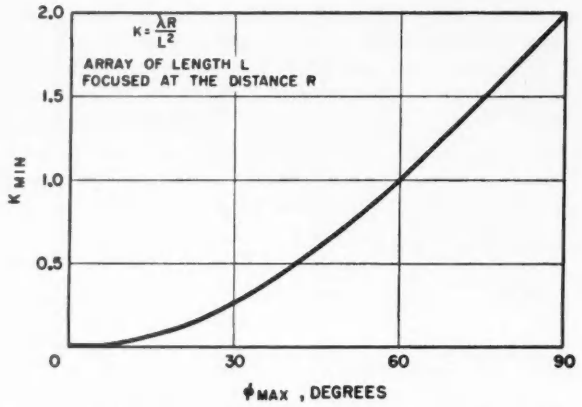

FIG. 3. Minimum K for a maximum phase error of $\lambda/16$ at the extremities $\pm\phi_{\max}$.

Within the specified error then

$$\left| U_p \right| = \frac{F}{R}\int_s f \exp\left[j\frac{k}{R}(y_1y_2+z_1z_2) \right] dS,$$

which is the Fraunhofer field of a plane aperture having a distribution f and element factors F.

IV. APPLICATION TO LINEAR SLOT ARRAYS

This method of measuring patterns is particularly applicable to slotted waveguide arrays. The amount of bending necessary is easily within the elastic limit of the waveguide unless it is necessary to get extremely close to the array.

In order to get an experimental evaluation of this method, two resonant arrays of moderate length (L^2/λ = 33 ft.) were built. Such arrays permitted pattern measurements to be taken at many times L^2/λ as well as at fractions of L^2/λ. These arrays, one having a uniform distribution and the other having a 25-db. Taylor distribution, were curved by putting a permanent bend in the waveguide to a tolerance of ± 0.010 in.

In addition, a typical nonresonant array having a 25-db. Taylor distribution and L^2/λ = 2193 ft. was mounted in a focusing framework having only a nine-point support as shown in Fig. 4. The characteristic linear phase error of nonresonant arrays is most easily handled by dealing with the equivalent equi-phased array obtained by projection of the aperture. For this array the projection angle is only about one degree.

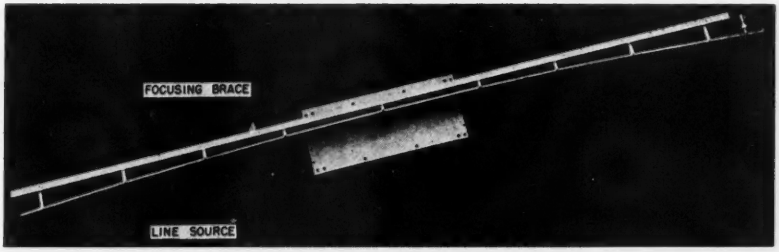

FIG. 4. Slot array in focusing frame.

Table I summarizes the characteristics and measurement parameters of the antennas tested.

TABLE I

CHARACTERISTICS AND MEASUREMENT PARAMETERS OF ANTENNAS TESTED

Antenna	Aperture distribution	L^2/λ, feet	Chosen focal distance, feet	$K = \lambda R/L^2$	ϕ_{max}, degrees	Transmitting horn L^2/λ, feet
Resonant inclined slot array	Uniform	33	11	1/3	±34	0.054
Resonant inclined slot array	25-db. Taylor	33	11	1/3	±34	0.054
Nonresonant edge slot array	25-db. Taylor	2193	65	0.03	±10*	0.055

*Relative to the projected equi-phase array.

V. EXPERIMENT

The patterns of all three arrays were measured at the focal distance with the arrays both curved and straight. In addition, the short arrays were measured in the normal manner at $R = 18\,L^2/\lambda$ while the long array was measured at $R = 1.37\,L^2/\lambda$.

These patterns are shown in Figs. 5 through 7. By comparing the patterns taken at the focal distance, the quantity γ can be obtained in two ways. It will be recalled that γ is the factor by which the beamwidth increases because of focusing on infinity rather than the focal point. Under the same conditions γ is also the factor by which the maximum gain of a *linear* array decreases.

For convenience, a theoretical curve of γ versus $\sqrt{(L^2/2\lambda R)}$ for a uniformly illuminated linear array is shown in Fig. 8. For other illuminations, γ can be computed from the formula in Bickmore (1957). These results are summarized in Table II.

The tabulated data were taken from vacuum-tube voltmeter readings rather than from the recorded data. The recorded patterns are, however, fairly accurate and give a better over-all perspective of the results of the various measurements. Gain comparisons between individual recorded patterns cannot be made because of the normalization.

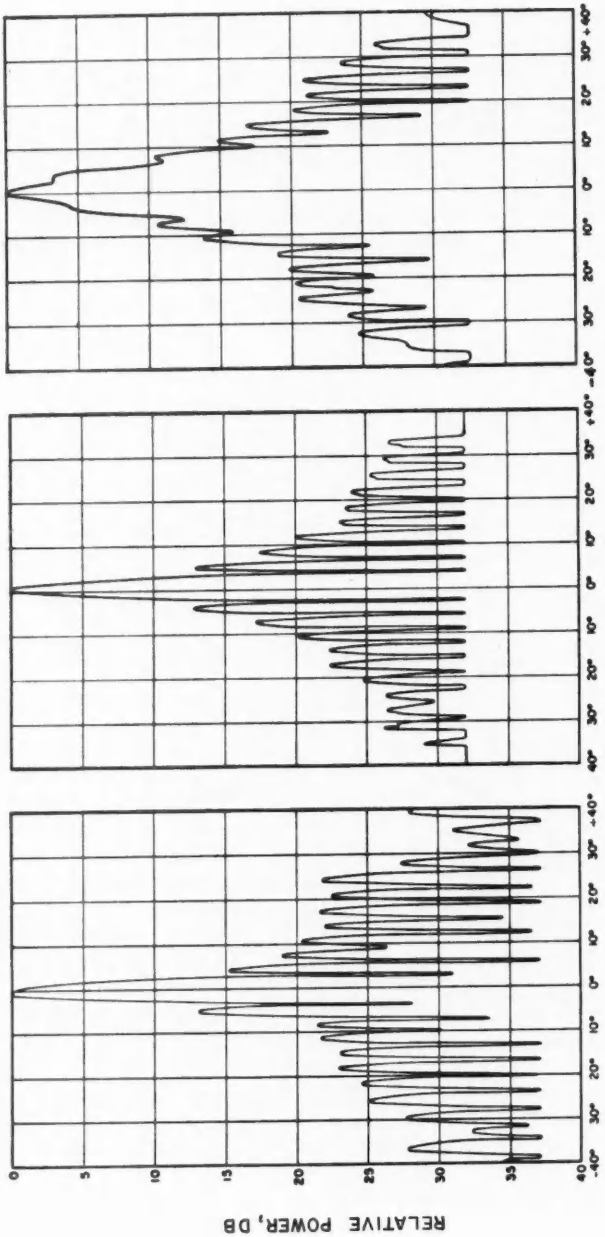

FIG. 5. Patterns of uniform array at various distances.

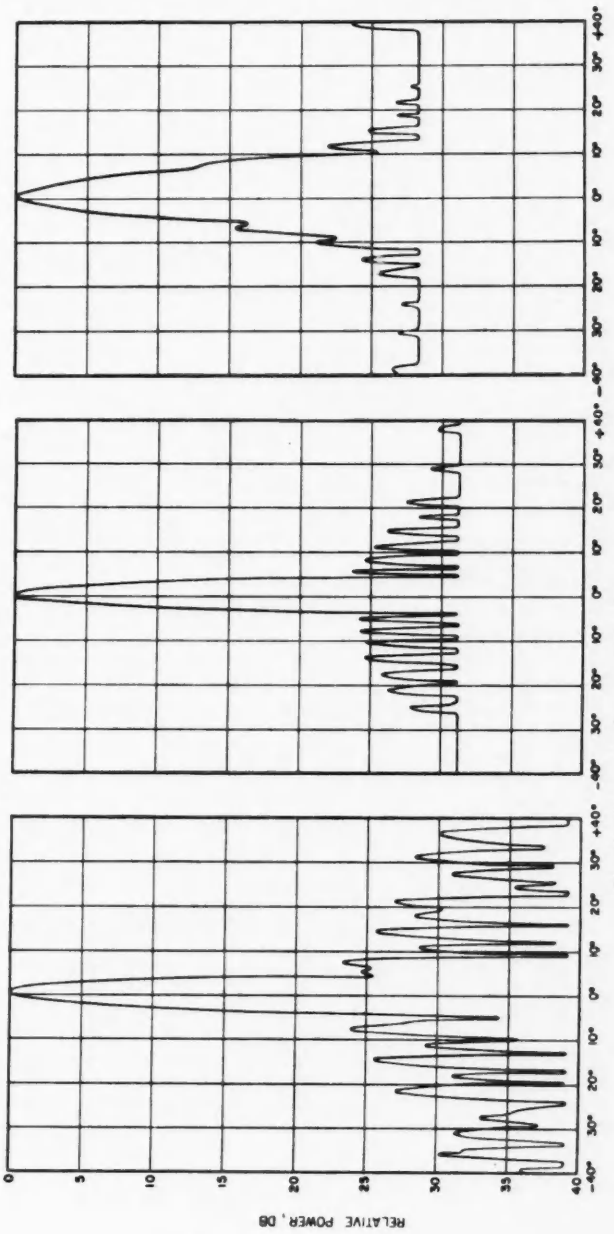

FIG. 6. Patterns of resonant Taylor array at various distances.

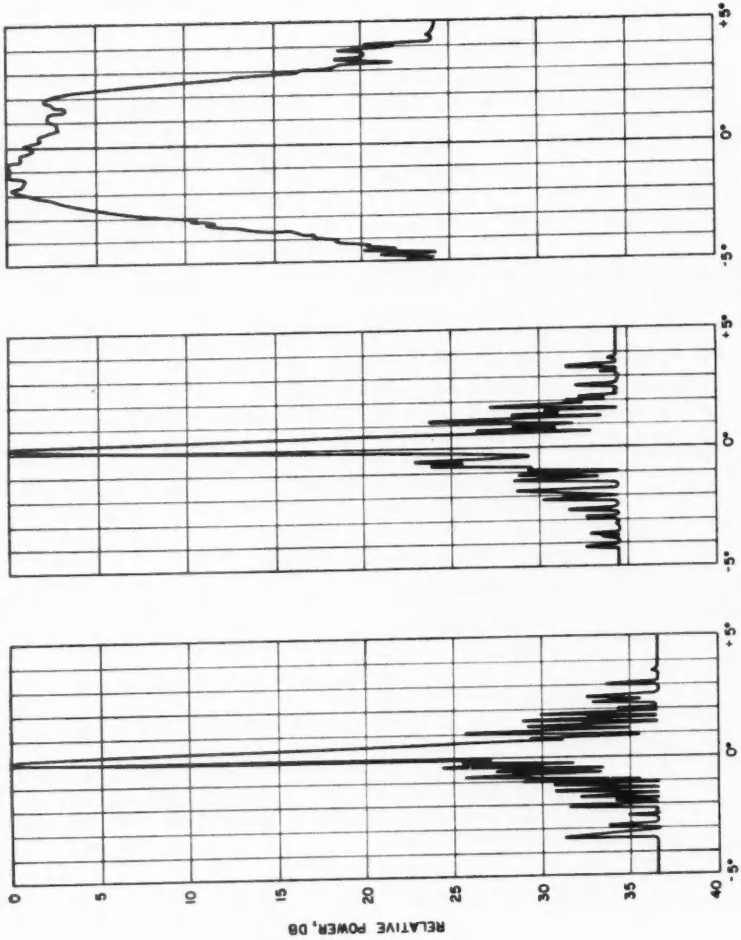

FIG. 7. Patterns of nonresonant Taylor array at various distances.

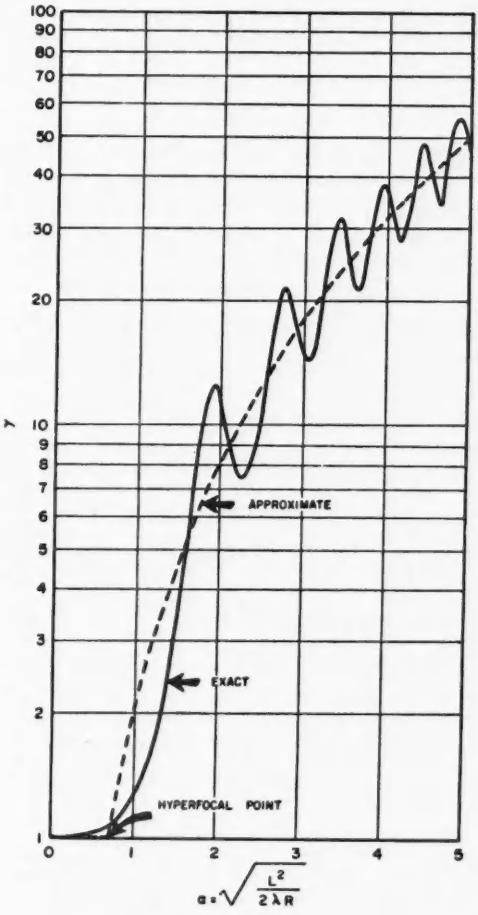

FIG. 8. γ versus α.

TABLE II

THEORETICAL AND EXPERIMENTAL RESULTS

Antenna	L^2/λ, feet	$K' = \lambda R/L^2$ at focal distance	$K' = \lambda R'/L^2$ on normal pattern range	Theoretical γ, (db.)	Experimental γ from 1/10 power beam-width	Experimental γ from gain, db.
Uniform resonant array	33	1/3	18	1.68 = (2.25)	1.67	2.23
Taylor resonant array	33	1/3	18	1.56 = (1.94)	1.53	2.01
Taylor nonresonant array	2193	0.03	1.37	28.0 = (14.5)	25.7	14.7

Comparison of the focused patterns with the patterns taken on the conventional range shows in general the cleaner, more symmetrical nature of the focused patterns, especially for the short arrays in which tolerances were held quite close.

In the process of accumulating more experimental data than are practical to include, a number of salient features which bear directly on pattern measurements by this method were noted and are described as follows:

(1) The truth of curvature should be maintained within $\lambda/10$.
(2) The nominal radius of curvature (focal distance) should be maintained within 1/10 of the operational depth of focus as defined by Bickmore (1957).
(3) The phase center of the array should coincide with the geometrical axis of rotation.
(4) The focal distance should be measured to the phase center of the transmitting antenna. For example, a horn may have its phase center several inches behind the opening.
(5) Multiple reflection between the two antennas could conceivably be a problem, but no difficulty was encountered in any of these measurements.

VI. CONCLUSIONS

This method of Fraunhofer pattern measurement has some obvious advantages for certain types of arrays to which it is adaptable. However, the price paid for the superiority in the region of the main lobe is in the form of tighter tolerances on setting up and rotating the array on the pattern range.

The chief advantage of focusing does not occur when there is a choice of methods but rather when an extremely high-resolution array must be measured. For such arrays most pattern ranges are completely inadequate unless focusing is used, and yet the employment of the focusing method is in no sense a compromise in the main region of interest.

ACKNOWLEDGMENT

The author is indebted to M. G. Chernin and C. M. Knop for supplying the experimental data used in this paper.

REFERENCES

BARRAR, R. B. and WILCOX, C. H. 1955. The Fresnel field of a finite line current distribution. Scientific Report No. 4 on Contract AF 19(604)-1317, Research Laboratories, Hughes Aircraft Company, Culver City, Calif.

BICKMORE, R. W. 1957. Can. J. Phys. **35**, 1292.

SILVER, S. 1949. Microwave antenna theory and design. M.I.T. Radiation Laboratory Series No. 12 (McGraw-Hill Book Co., Inc., New York, N. Y.).

CONSERVATION OF PARITY IN STRONG INTERACTIONS[1]

SURAJ N. GUPTA[2]

ABSTRACT

The conservation of parity in electromagnetic and mesonic interactions and the non-conservation of parity in the neutrino interactions are discussed on the basis of the principle of invariance under combined space inversion and charge conjugation.

It has been established by recent experiments (Wu *et al.* 1957) that parity is not conserved in processes involving the neutrinos. On the other hand, it is well known that parity is conserved in electromagnetic and mesonic interactions. We shall briefly discuss the theoretical reason for this difference in the behavior of the neutrino interactions and the "strong" interactions.

ELECTROMAGNETIC INTERACTION

If we assume that the interaction between the photon and the electron fields should only satisfy the requirement of invariance under proper Lorentz transformations, the simplest field equation for the photon field in the Heisenberg representation will be

$$\Box^2 A_\mu = -ie\bar{\psi}\gamma_\mu\psi - ie'\bar{\psi}\gamma_5\gamma_\mu\psi, \tag{1}$$

where $\bar{\psi} = \psi^*\gamma_4$, and an asterisk denotes the Hermitian conjugate. But the photon field has to satisfy also the supplementary condition (Gupta 1950)

$$[\partial A_\mu/\partial x_\mu]^+\psi = 0, \tag{2}$$

which is compatible with (1) only if

$$\partial(-ie\bar{\psi}\gamma_\mu\psi - ie'\bar{\psi}\gamma_5\gamma_\mu\psi)/\partial x_\mu = 0. \tag{3}$$

In order to satisfy the above relation, we must take $e' = 0$, so that (1) reduces to the usual field equation

$$\Box^2 A_\mu = -ie\bar{\psi}\gamma_\mu\psi. \tag{4}$$

Thus, the conservation of parity in the electromagnetic interactions can be regarded as a consequence of the supplementary condition.

MESONIC INTERACTION

If we again confine ourselves to the requirement of invariance under proper Lorentz transformations in the interaction of spinless mesons and nucleons, we can write the simplest interaction energy density in the interaction representation as

$$H = gU_0\bar{\psi}\psi + ig'U_0\bar{\psi}\gamma_5\psi, \tag{5}$$

[1]Manuscript received July 22, 1957.
Contribution from the Division of Pure Physics, National Research Council, Ottawa, Ontario.
Issued as N.R.C. No. 4503.

[2]Permanent address: Department of Physics, Wayne State University, Detroit, Michigan, U.S.A.

where for the sake of simplicity we have taken the meson field as neutral. In the present case it is not possible to eliminate one of the above interactions by any supplementary condition. Therefore, following Lee and Yang (1957) and Landau (1957), we shall further assume that the physical laws should be invariant under the combined inversion, which includes space inversion as well as charge conjugation. In order to ensure the invariance of the above nucleon–meson interaction under the combined inversion, we must replace (5) by

$$H' = gU_0[\bar{\psi}_\alpha\psi_\alpha - \psi_\alpha\bar{\psi}_\alpha] + ig'U_0[\bar{\psi}_\alpha(\gamma_5)_{\alpha\beta}\psi_\beta + \psi_\beta(\gamma_5)_{\alpha\beta}\bar{\psi}_\alpha], \tag{6}$$

where we have treated U_0 as a scalar. The second term on the right-hand side of (6) does not contribute to any Feynman diagram except in the trivial case when two nucleon lines originating from the same vertex are joined to each other. Therefore, for all practical purposes (6) is equivalent to the usual scalar coupling interaction

$$H' = gU_0[\bar{\psi}_\alpha\psi_\alpha - \psi_\alpha\bar{\psi}_\alpha]. \tag{7}$$

Similarly, if we treat U_0 as a pseudoscalar, then the invariance under the combined inversion requires that (5) be replaced by

$$H'' = gU_0[\bar{\psi}_\alpha\psi_\alpha + \psi_\alpha\bar{\psi}_\alpha] + ig'U_0[\bar{\psi}_\alpha(\gamma_5)_{\alpha\beta}\psi_\beta - \psi_\beta(\gamma_5)_{\alpha\beta}\bar{\psi}_\alpha], \tag{8}$$

which is equivalent to

$$H'' = ig'U_0[\bar{\psi}_\alpha(\gamma_5)_{\alpha\beta}\psi_\beta - \psi_\beta(\gamma_5)_{\alpha\beta}\bar{\psi}_\alpha]. \tag{9}$$

Thus, the principle of combined inversion rules out a mixture of the scalar and the pseudoscalar couplings.

The above argument can also be applied to the charge symmetrical meson theory. In that case the simplest charge symmetrical interaction energy density, which is invariant under proper Lorentz transformations, is

$$H_{\text{sym}} = H_1 + H_2 \tag{10}$$

with

$$H_1 = \sqrt{2}g\bar{\psi}_N\psi_P U^* + \sqrt{2}g\bar{\psi}_P\psi_N U + g\bar{\psi}_N\psi_N U_0 - g\bar{\psi}_P\psi_P U_0, \tag{11}$$

$$H_2 = i\sqrt{2}g'\bar{\psi}_N\gamma_5\psi_P U^* + i\sqrt{2}g'\bar{\psi}_P\gamma_5\psi_N U + ig'\bar{\psi}_N\gamma_5\psi_N U_0 - ig'\bar{\psi}_P\gamma_5\psi_P U_0, \tag{12}$$

where ψ_N and ψ_P denote the field operators for neutrons and protons respectively. However, the requirement of invariance under the combined inversion is again sufficient to eliminate either H_1 or H_2 from (10) according to whether we treat U as a scalar or a pseudoscalar.

CONCLUSION

We have shown that for strong interactions the principle of combined inversion leads to the same results as the usual space inversion. Moreover, there are indications that the principle of combined inversion is also satisfied by the neutrino interactions, although these interactions are not invariant under space inversion alone. Hence, the parity conservation in strong inter-

actions and the parity non-conservation in the neutrino interactions can both be understood on the basis of the principle of combined inversion.

It should be observed that we have referred to the electromagnetic and the mesonic interactions as strong interactions merely for convenience. We do not believe that the parity non-conservation in the neutrino interactions is connected with the weakness of these interactions. For, according to Einstein's theory of gravitation, parity is conserved in the gravitational interactions, which are even weaker than the neutrino interactions. Although several attempts have been made from time to time to find an alternative to Einstein's theory, all such attempts have proved futile so far (Gupta 1957). Moreover, since there exists a close analogy between gravitation and electromagnetism (Gupta 1954), we can show by the same argument as used for the electromagnetic field that we cannot introduce in Einstein's gravitational field equations an interaction which will violate the conservation of parity.

REFERENCES

GUPTA, S. N. 1950. Proc. Phys. Soc. A, **63**, 681.
——— 1954. Phys. Rev. **96**, 1683.
——— 1957. Revs. Modern Phys. **29**, 334.
LANDAU, L. 1957. Nuclear Phys. **3**, 127.
LEE, T. D. and YANG, C. N. 1957. Phys. Rev. **105**, 1671.
WU, C. S., AMBLER, E., HAYWARD, R. W., HOPPES, D. D., and HUDSON, R. P. 1957. Phys. Rev. **105**, 1413.

AN ABSOLUTE DETERMINATION OF RESISTANCE[1]

M. Romanowski and N. Olson

ABSTRACT

An absolute determination of resistance has been completed in the laboratories of the National Research Council, using a bridge which was originally derived as a modification of Campbell's network. It can be shown that this network can also be treated as a special case of the bridge used by Hartshorn for the comparison of equal mutual inductors. This latter aspect is a very valuable feature, for it means that the same basic network can be used for nearly all the a-c. operations, i.e. calibration of inductors in terms of the computed standard, measurement of self-capacitances and intercapacitances, and the inductance bridge. The change from the comparison bridge to inductance bridge is accomplished simply by replacing one of the inductors by one having twice its value and by shunting its primary by an appropriate resistor. By doing so, the very low value of the "potentiometer" in the comparison bridge increases so as to be equal to $R_1 = 1\ \Omega$, the latter becoming the resistor whose value is to be determined in terms of inductance (length) and frequency (time). The computed value of the standard inductor being equal to 10 mh. nominal, the value 20 mh. is obtained by the addition method on a specially designed inductor.

A complete analysis of the circuit, including all small terms (self-capacitances, intercapacitances, residual inductances), is made for all operations: comparisons of inductors, addition of inductances, and finally the main bridge. The methods for the evaluation of these small terms are the most important and are therefore given with some detail. This includes also the evaluation of a ratio of resistances that figures in the equation for R_1. This is made by means of a resistance comparator and its auxiliary equipment. A complete measurement is quoted from our laboratory book.

A total of over 100 such measurements of R_1 in absolute units were made. Their average shows that the unit presently used in the N.R.C. laboratory (deduced from calibrations made on N.R.C. standards by other national laboratories) is about 8 parts in a million smaller than the unit given by our method. This absolute unit agrees very closely with units resulting from similar work done in various other national laboratories.

1. INTRODUCTION

A general survey of bridge methods for the determination of the unit of electrical resistance and a brief outline of the method adopted in our laboratory were given in a previous paper (Romanowski 1952). The equations given in it are identical with the equations (1) and (2) of this publication. A simple comparison between these expressions and the equations (9) and (10), actually used in our work, shows the complexity of the problem. In addition to the main terms (in bold printing) we see many secondary terms of the form of $[K]x$, where x is a small component and $[K]$ is a factor formed of various large components, not only of those which figure in the main terms but also of many others of lesser importance. While the components that form the main terms have to be measured with the highest possible precision, the accuracy of all others depends on the magnitude of x. It is generally obtained by some classical medium precision method. The description and the list of small components (of x type) are given in Section 2. Their measurement constitutes one of the major problems of the determination of the ohm. It is

[1]Manuscript received June 24, 1957.
Contribution from the Division of Applied Physics, National Research Council, Ottawa, Ontario.
Issued as N.R.C. No. 4513.

given full consideration in various parts of the article (particularly Sections 6 and 7).

Before describing the work actually done since the first paper (Romanowski 1952), let us simply recall that the most important innovation in our method is the measurement of the value of an inductor the nominal value of which is equal to twice the value of our computed Standard. Although the Neumann integral, by means of which the inductance is computed, follows the law of addition, the presence of all small components requires a thorough analysis (theoretical and experimental) of the problem of the actual addition process on mutual inductors.

2. INDUCTANCE BRIDGE

The simple circuit of the inductance bridge is given in Fig. 1. The balance conditions are expressed by the equations

$$R_1(R_2+R_c)+\omega^2 L_c M_1 = 0, \tag{1}$$

$$R_1 L_c - R_2(M_1+M_2) - R_c M_1 = 0. \tag{2}$$

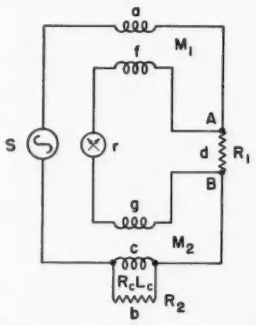

FIG. 1. Basic circuit of inductance bridge.

M_1, M_2, and R_1 can be positive or negative. Therefore, the following combinations are possible:

$$(a)\ M_1-,\ M_2+,\ R_1+,$$

$$(b)\ M_1+,\ M_2-,\ R_1-.$$

Before proceeding further, it will be necessary to clarify the preceding statement about the signs of M_1, M_2, and R_1, and to adopt a convention.

First consider two coils, a primary and secondary, with a common point, and wound in the manner shown in Fig. 2(*a*). Starting at the free primary terminal and proceeding through the common point to the free secondary terminal, the coils are in the same sense. The arrows indicate the arbitrary positive sense of currents and e.m.f.'s. The primary e.m.f. $-j\omega Li$ and the corresponding secondary e.m.f. $-j\omega Mi$ are in the same sense, i.e. *series aiding*, and since L is always positive, then M is regarded as having a *positive* sign.

Next consider two coils as shown in Fig. 2(*b*), where, starting at the free primary terminal and proceeding through the common point to the free secondary terminal, the coils are in opposite senses. The primary e.m.f. $-j\omega Li$ and the secondary e.m.f. $-j\omega Mi$ are in opposite senses, i.e. *series opposition*, and M is regarded as having a *negative* sign.

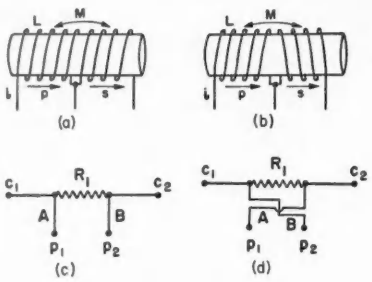

FIG. 2. Convention on signs: (*a*) positive mutual, (*b*) negative mutual, (*c*) positive R_1, (*d*) negative R_1.

Finally consider a four-terminal resistor such as R_1 with current terminals C_1 and C_2, and potential terminals p_1 and p_2, and with potential leads A and B connected to the resistor as shown in Fig. 2(*c*). Here we see that the e.m.f. between p_1 and p_2 is in phase with the current from C_1 to C_2. Consequently R_1 is treated mathematically as having a *positive* sign.

If the potential leads A and B are crossed as shown in Fig. 2(*d*), then the e.m.f. between p_1 and p_2 is in opposite phase with the current from C_1 to C_2. Consequently R_1 is treated mathematically as having a *negative* sign.

The inductance bridge circuit in Fig. 1 corresponds to case (*a*) above. Substitute $L_c = -R_1(R_2+R_c)/\omega^2 M_1$ from eq. (1) and $M_2 = -\kappa M_1$ into eq. (2) and solve for R_1:

$$R_1 = \left[\frac{(\kappa-1)R_2-R_c}{R_2+R_c} \times \omega^2 {M_1}^2\right]^{\frac{1}{2}}. \tag{3}$$

Equation (3) is the fundamental relation between resistance R_1, frequency $f = \omega/2\pi$, and mutual inductance M_1. The first factor in the square root bracket is a pure ratio.

In order to derive the numerical values of the components of the bridge, four initial selections must be made:

(1) Standard of mutual inductance, which may be used as M_1 in the inductance bridge, or in Hartshorn bridge (Hartshorn 1925) comparisons to establish M_1 for the inductance bridge. The nominal value is 10^{-2} h., and its precise value is computed from the dimensions of the windings.

(2) Ratio of M_2 to M_1, i.e. κ. The guiding principle here is simplicity, so a nominal value $\kappa = 2$ is chosen. The exact value of κ must be determined by suitable experimental methods.

(3) Frequency f ($\omega = 2\pi f$). The choice of $f = 100$ c.p.s. is in line with the choice in other laboratories. It represents a compromise between large reactive components and high frequency difficulties, such as skin effect. The desired frequency is obtained by standard scaling techniques from quartz crystal oscillators.

(4) Resistance R_1, whose value in ohms is to be determined in terms of ω and M_1. $R_1 = 1$ ohm nominal is chosen, since this facilitates comparisons with 1-ohm standards whose values have been established in terms of our laboratory's unit of resistance.

It is now possible to establish the relation between the remaining three components, R_2, R_c, and L_c, which appear in eqs. (1) and (2). With the values $M_1 = -10^{-2}$ h., $\kappa = 2$, and $R_1 = 1\ \Omega$, we have:

$$L_c = -\frac{R_1(R_2+R_c)}{\omega^2 M_1} = \frac{R_2+R_c}{39.4783\times 10^2}, \tag{4}$$

and from eq. (2)

$$R_1 L_c + (R_2 - R_c)M_1 = 0$$

or

$$(R_2+R_c) = 39.4783(R_2-R_c); \tag{5}$$

therefore

$$\begin{aligned} R_2 &= 1.0520 R_c, \\ R_c &= 1.9237\times 10^2 L_c. \end{aligned} \tag{6}$$

The physical realization of the primary circuit of M_2 imposes certain limitations on the possible values of R_c and L_c if the second relation in eq. (6) is to be satisfied. Once appropriate values of R_c and L_c have been established, the value of R_2 follows immediately from the first relation in eq. (6).

In addition to the two possible combinations for the signs of M_1, M_2, and R_1, there are limiting values for κ, M_1, and M_2 beyond which there is no balance for the inductance bridge. These limits may be determined as follows:

Eliminate L_c from eqs. (1) and (2) and solve for M_1:

$$M_1 = -\frac{R_2 M_2}{2(R_2+R_c)} \pm \left[\frac{R_2^2 M_2^2}{4(R_2+R_c)^2} - \frac{R_1^2}{\omega^2}\right]^{\frac{1}{2}}. \tag{7}$$

Since M_1 is always real, it follows that

$$M_2^2 \geqslant \frac{4(R_2+R_c)^2}{R_2^2}\frac{R_1^2}{\omega^2}. \tag{8}$$

(*a*) Let $R_1 = +r$, where r is real and positive. Then

$$M_2 \geqslant \frac{2(R_2+R_c)}{R_2}\frac{r}{\omega}.$$

For each value of M_2 there are two possible values for M_1 and κ:

(1) $$-\frac{r}{\omega} \leqslant M_1 \leqslant 0, \qquad \frac{2(R_2+R_c)}{R_2} \leqslant \kappa \leqslant \infty,$$

(2) $$-\frac{r}{\omega} \geqslant M_1 \geqslant -\infty, \qquad \frac{2(R_2+R_c)}{R_2} \geqslant \kappa \geqslant \frac{R_2+R_c}{R_2}.$$

(*b*) Let $R_1 = -r$. Then

$$M_2 \leqslant -\frac{2(R_2+R_c)}{R_2}\frac{r}{\omega}.$$

As before, there are two possible values of M_1 and κ for each value of M_2:

(1) $$+\frac{r}{\omega} \geqslant M_1 \geqslant 0, \qquad \frac{2(R_2+R_c)}{R_2} \leqslant \kappa \leqslant \infty,$$

(2) $$+\frac{r}{\omega} \leqslant M_1 \leqslant +\infty, \qquad \frac{2(R_2+R_c)}{R_2} \geqslant \kappa \geqslant \frac{R_2+R_c}{R_2}.$$

For high accuracy work, a more detailed analysis of the inductance bridge is necessary. The simple circuit of Fig. 1 must be replaced by a network which includes small components. These small components may be described as follows:

(*a*) Every winding of the mutual inductances M_1 and M_2 has distributed self-capacitance which may be represented as a lumped capacitance between the terminals of the winding (subscripts p, q, u, v).

(*b*) Between the primary and secondary of each mutual inductance there is a distributed intercapacitance, which in the present case of a common point may be represented as a lumped capacitance between the free terminals of the two windings (subscripts h, k).

(*c*) Every winding has a leakage resistance which depends on the quality of the insulation between turns. In addition there is a leakage resistance between windings. These components are represented in the network by a resistance between appropriate pairs of terminals. If the insulation is good, they can be neglected.

(*d*) Every resistance has an associated residual reactance, which may be inductive or capacitative. If the reactance is inductive, it is represented as an inductance in series with the resistance. If it is capacitative, it is represented as a capacitance in parallel with the resistor, or an equivalent negative inductance in series. The impedance of a resistor with shunted residual capacitance is

$$Z = \frac{R-j\omega R^2C}{1+\omega^2R^2C^2} \simeq R-j\omega R^2C.$$

Therefore to a very good approximation the reactance is represented by a negative inductance with a magnitude R^2C.

(*e*) The magnetic field of the primary current induces currents in surrounding conducting materials, which in turn react with the secondary circuits. The effect may be represented by a conducting loop associated with each

mutual inductance and inductively coupled to its windings. This effect can of course be eliminated by removing all conducting materials from the vicinity of the inductors.

Eddy currents in the windings themselves may also be represented as loops, and can be reduced to negligible proportions by using highly stranded and twisted wire in the coils.

(*f*) Interactions between M_1 and M_2 whereby the primary of M_1 induces an e.m.f. in the secondary of M_2, and vice versa. This effect is eliminated by suitable orientation of the inductors with respect to each other.

(*g*) Ground capacitance effects in the primary circuit are negligible. Ground capacitance effects in the secondary circuit are eliminated by the use of a Wagner ground (see Appendix 2).

(*h*) Interactions between primary circuits and other leads and connections in the bridge circuit are eliminated by proper positioning of leads, and use of compensating loops if necessary.

In view of the preceding discussion of small components, it will be necessary to include self-capacitance and intercapacitance of the inductors, and residual reactance of the resistors in the bridge network. The reactance of the resistors is shown as inductive, corresponding to the actual case. The branch symbols and the impedances they represent are listed for convenience.

$a = R_a + j\omega L_a$	$h = -j/\omega C_h$	r	=	impedance of detector
$b = R_2 + j\omega\lambda_2$	$k = -j/\omega C_k$	s	=	impedance of source
$c = R_c + j\omega L_c$	$p = -j/\omega C_p$	af	=	$fa = +j\omega M_1$
$d = R_1 + j\omega\lambda_1$	$q = -j/\omega C_q$	cg	=	$gc = +j\omega M_2$
$f = R_f + j\omega L_f$	$u = -j/\omega C_u$			
$g = R_g + j\omega L_g$	$v = -j/\omega C_v$			

The inductance bridge network, Fig. 3, corresponding to case (*a*) has been analyzed by Kron's matrix method, and the complete real and imaginary equations are given below, (9) and (10). In Appendix 1 is given an outline of the calculation for the case of one single small component.

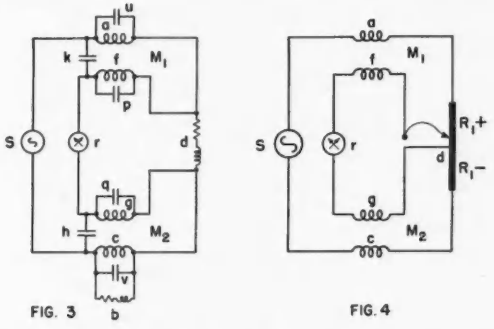

FIG. 3. Circuit of inductance bridge with small components.
FIG. 4. Basic circuit of the Hartshorn bridge with the slide wire replacing the resistor R_1 (in Fig. 1).

Equations (1) and (2), being linear and homogeneous in M_1, M_2, and R_1, are satisfied by two sets of values of M_1, M_2, and R_1, where one set is converted into the other by multiplication by -1. In eqs. (9) and (10) this property is preserved in the secondary terms in λ_1, λ_2, and all self-capacitances, but not in intercapacitances. It is interesting to note that λ_1 has the same mathematical properties as R_1.

In the bridge corresponding to case (*b*), the coefficients of the intercapacitance terms are somewhat different. This is not surprising in view of the different aspect of the common point between primary and secondary windings in the two bridges. These common points are more precisely defined in the bridge corresponding to case (*a*), and therefore this bridge was given preference.

$$
\begin{aligned}
(9)\quad & \boldsymbol{R}_1(\boldsymbol{R}_2+\boldsymbol{R}_c)+\omega^2\boldsymbol{L}_c\boldsymbol{M}_1 \\
& +[-\omega^2L_c]\lambda_1+[\omega^2(M_1+M_2)]\lambda_2 \\
& +[\omega^2R_2M_1(R_c+R_g)-\omega^2R_1R_2(L_c+L_g+2M_2)-\omega^2(R_1+R_2)(R_cL_g+R_gL_c) \\
& \quad +\omega^2M_1(R_cR_g-\omega^2L_cL_g+\omega^2M_2{}^2)]C_h \\
& +[\omega^2(R_2M_2-R_1L_c)(R_a+R_f)-\omega^2R_1(R_2+R_c)(L_a+L_f+2M_1) \\
& \quad -\omega^2(R_2+R_c)(R_aL_f+R_fL_a)-\omega^2L_c(R_aR_f-\omega^2L_aL_f+\omega^2M_1{}^2)]C_k \\
& +[\omega^2(R_2M_2-R_1L_c)R_f-\omega^2R_1(R_2+R_c)L_f]C_p \\
& +[\omega^2\{(R_2+R_c)M_1-R_1L_c\}R_g-\omega^2\{R_1(R_2+R_c)+\omega^2L_cM_1\}L_g+\omega^4M_1M_2{}^2]C_q \\
& +[\omega^2(R_2M_2-R_1L_c)R_a-\omega^2R_1(R_2+R_c)L_a]C_u \\
& +[\omega^2R_2R_cM_1-\omega^2R_1R_2L_c]C_v \qquad = 0
\end{aligned}
$$

$$
\begin{aligned}
(10)\quad & \boldsymbol{R}_1\boldsymbol{L}_c-\boldsymbol{R}_2(\boldsymbol{M}_1+\boldsymbol{M}_2)-\boldsymbol{R}_c\boldsymbol{M}_1 \\
& +[R_2+R_c]\lambda_1+[R_1]\lambda_2 \\
& +[R_1R_2(R_c+R_g)+\omega^2R_2M_1(L_c+L_g+2M_2)+\omega^2M_1(R_cL_g+R_gL_c) \\
& \quad +(R_1+R_2)(R_cR_g-\omega^2L_cL_g+\omega^2M_2{}^2)]C_h \\
& +[R_1(R_2+R_c)(R_a+R_f)+\omega^2(R_2M_2-R_1L_c)(L_a+L_f+2M_1) \\
& \quad -\omega^2L_c(R_aL_f+R_fL_a)+(R_2+R_c)(R_aR_f-\omega^2L_aL_f+\omega^2M_1{}^2)]C_k \\
& +[R_1(R_2+R_c)R_f+\omega^2(R_2M_2-R_1L_c)L_f]C_p \\
& +[\{R_1(R_2+R_c)+\omega^2L_cM_1\}R_g+\omega^2\{(R_2+R_c)M_1-R_1L_c\}L_g+\omega^2M_2{}^2R_1]C_q \\
& +[R_1(R_2+R_c)R_a+\omega^2(R_2M_2-R_1L_c)L_a]C_u \\
& +[R_1R_2R_c+\omega^2R_2M_1L_c]C_v \qquad = 0
\end{aligned}
$$

Equations (9) and (10) may be written in the following concise form:

$$(11)\qquad R_1(R_2+R_c)+\omega^2L_cM_1+k_1 = 0,$$

$$(12)\qquad R_1L_c-R_2(M_1+M_2)-R_cM_1+k_2 = 0.$$

The main terms of eqs. (9) and (10) are identical to eqs. (1) and (2). k_1 and k_2 represent the sums of all the small terms of the form $[K]x$.

Eliminate L_c and M_2 from eqs. (11) and (12) and solve for R_1:

$$(13)\qquad R_1 = -\frac{k_1}{2(R_2+R_c)}+\left[\frac{(\kappa-1)R_2-R_c}{R_2+R_c}\omega^2M_1{}^2+\frac{k_2\omega^2M_1}{R_2+R_c}\right]^{\frac{1}{2}}.$$

Equation (13) is the complete expression for R_1 with the effects of all the small components accounted for in k_1, k_2, and κ.

The inductance bridge is one of a large family of possible bridges, the

prototype of which is the well-known Hartshorn bridge (Hartshorn 1925), Fig. 4, for the comparison of nominally equal mutual inductances. The Hartshorn bridge is obtained by simply making the resistance R_2 in the inductance bridge infinite. R_1 now becomes a small component in which the residual inductance λ_1 is no longer of any consequence, and nominally M_1 becomes equal to M_2.

The equations for the Hartshorn bridge follow immediately from eqs. (9) and (10). It will be noted that all small terms containing R_1 now become negligibly small and will be discarded. The equations are:

$$(14)\quad \begin{aligned} R_1 &-[-\omega^2 M_1(R_c+R_g)+\omega^2(R_cL_g+R_gL_c)]C_h \\ &-[-\omega^2 M_2(R_a+R_f)+\omega^2(R_aL_f+R_fL_a)]C_k \\ &+\omega^2 M_2R_fC_p+\omega^2 M_1R_gC_q+\omega^2 M_2R_aC_u+\omega^2 M_1R_cC_v = 0, \end{aligned}$$

$$(15)\quad \begin{aligned} (M_1+M_2) &-[\omega^2 M_1(L_c+L_g+2M_2)+(R_cR_g-\omega^2 L_cL_g+\omega^2 M_2^{\,2})]C_h \\ &-[\omega^2 M_2(L_a+L_f+2M_1)+(R_aR_f-\omega^2 L_aL_f+\omega^2 M_1^{\,2})]C_k \\ &-\omega^2 M_2L_fC_p-\omega^2 M_1L_gC_q-\omega^2 M_2L_aC_u-\omega^2 M_1L_cC_v = 0. \end{aligned}$$

Equation (14) will be used in the section dealing with the evaluation of self-capacitance and intercapacitance, while (15) will be used for the establishment of κ. Equation (15) may be put in the simplified form

$$(16)\qquad M_1+M_2+\Delta M_1+\Delta M_2 = 0.$$

ΔM_1 represents the terms in C_k, C_p, and C_u, and ΔM_2 the terms in C_h, C_q, and C_v.

3. DESCRIPTION OF INDUCTORS

Four inductors were actually used to perform all operations for a determination of the ohm.

(*a*) *The Standard Campbell Inductor*, the computed value of which is equal to 0.010007248 h., has been described in another paper (Henderson and Romanowski 1955). The Standard is directly included in the inductance bridge and its value is designated in the balance equations by the symbol M_1.

(*b*) *The Horizontal Inductor* is a close replica of the Standard but with the axis horizontal. A small circular loop with a sliding contact, *S*, in series with the primary provides a range of adjustment of the order of 1 μh. (Fig. 5). The loop is fixed to a bakelite plate mounted on one of the ends of the quartz cylinder.

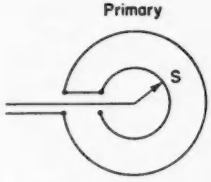

FIG. 5. Schematic diagram of the variable part of the horizontal inductor.

(*c*) The transition from 10 to 20 mh. is made on the *Double Campbell Inductor*, Fig. 21. Its primary consists of three helices wound on a bakelite cylinder and very similar to those of the Standard. It is equipped with two identical secondaries, each of them located close to the neutral circle of two adjacent primary helices. The secondaries can be used either separately (as 10 mh.) or connected in series to give 20 mh. They are of the same construction as the secondary of the Standard. The inductance is adjusted by means of the levelling screws on which the secondaries are resting.

(*d*) *The Manganin Inductor*, Fig. 22, has a value of 20 mh. and is designated by M_2. Its primary winding consists of 285 turns of stranded manganin cable (27 strands of No. 26 BS gauge wire) specially prepared for us by Northern Electric Company. In series with the primary winding and at a distance of several feet are located two small coaxial coils (l) of No. 12 BS gauge manganin wire, Fig. 9. By varying the distance between these coils (i.e. their mutual inductance) the self-inductance of the primary can be very finely adjusted to the value required in the bridge-balance equations. The resistance and the self-inductance of the primary are called respectively R_c and L_c (both include the small adjusting coils).

The relation between R_c and L_c was given above (eq. (6)). It is not difficult to satisfy with a manganin wire (or equivalent cable) on which the resistance per unit of length is similar to that of No. 12 BS gauge manganin wire. The coil is wound on a bakelite support built according to Brooks' design in order to obtain the maximum inductance for a given type and length of wire. From the originally built coil with 17 turns in 17 layers, 4 turns had to be removed when the inductor was incorporated into the general bridge circuit. The secondary is built on the same principle as all other secondaries. It is coaxial and almost coplanar with the primary coil. The axis of the inductor is horizontal.

Both vertical inductors (Standard and Double Campbell) are located side by side and as far as possible from those with horizontal axes. Thus a vertical inductor is always compared with a horizontal one. The process of eliminating the residual interaction which may remain is to reduce to zero (by appropriate adjustment of position) the flux linkage between one energized primary and the opposite secondary.

The value of κ defined by $\kappa = -M_2/M_1$ is determined by a series of four comparisons on the inductors described above. In this operation we indicate by superscripts the order of comparisons and we obtain:

(*a*) Comparison of the Standard Inductor (designated now by M_1') with the Horizontal Inductor (M_2')

$$M_1'+M_2'+\Delta M_1'+\Delta M_2' = 0.$$

(*b*) Comparison of the Double Campbell Inductor with the Horizontal Inductor

$$\text{Top secondary } (M_1''): M_1''+M_2'+\Delta M_1''+\Delta M_2' = 0,$$

$$\text{Bottom secondary } (M_1'''): M_1'''+M_2'+\Delta M_1'''+\Delta M_2' = 0.$$

(*c*) Comparison of the Double Campbell Inductor Series ($M_1{}^{IV}$) with the Manganin Inductor ($M_2{}^{IV}$)

$$M_1{}^{IV}+M_2{}^{IV}+\Delta M_1{}^{IV}+\Delta M_2{}^{IV}=0.$$

By means of these four relations we eliminate all terms related to the Horizontal Inductor (M_2' and $\Delta M_2'$) and taking into account the equality

$$M_1''+M_1'''=M_1{}^{IV},$$

we establish the formula

$$(17)\quad \kappa=-\frac{M_2{}^{IV}}{M_1'}=2+2\frac{\Delta M_1'}{M_1'}-\frac{\Delta M_1''}{M_1'}-\frac{\Delta M_1'''}{M_1'}+\frac{\Delta M_1{}^{IV}}{M_1'}+\frac{\Delta M_2{}^{IV}}{M_1'}.$$

The complete expression is:

$$\begin{aligned}(18)\quad \kappa=2&-\frac{2}{M_1'}[\omega^2M_2'(L_a'+L_f'+2M_1')+(R_a'R_f'-\omega^2L_a'L_f'\\&+\omega^2M_1'^2)]C_k'-\frac{2}{M_1'}[\omega^2L_f'M_2']C_p'-\frac{2}{M_1'}[\omega^2L_a'M_2']C_u'\\&+\frac{1}{M_1'}[\omega^2M_2'(L_a''+L_f''+2M_1'')+(R_a''R_f''-\omega^2L_a''L_f''\\&+\omega^2M_1''^2)]C_k''+\frac{1}{M_1'}[\omega^2L_f''M_2']C_p''+\frac{1}{M_1'}[\omega^2L_a''M_2']C_u''\\&+\frac{1}{M_1'}[\omega^2M_2'(L_a'''+L_f'''+2M_1''')+(R_a'''R_f'''-\omega^2L_a'''L_f'''\\&+\omega^2M_1'''^2)]C_k'''+\frac{1}{M_1'}[\omega^2L_f'''M_2']C_p'''+\frac{1}{M_1'}[\omega^2L_a'''M_2']C_u'''\\&-\frac{1}{M_1'}[\omega^2M_2{}^{IV}(L_a{}^{IV}+L_f{}^{IV}+2M_1{}^{IV})+(R_a{}^{IV}R_f{}^{IV}-\omega^2L_a{}^{IV}L_f{}^{IV}\\&+\omega^2M_1{}^{IV2})]C_k{}^{IV}-\frac{1}{M_1'}[\omega^2L_f{}^{IV}M_2{}^{IV}]C_p{}^{IV}-\frac{1}{M_1'}[\omega^2L_a{}^{IV}M_2{}^{IV}]C_u{}^{IV}\\&-\frac{1}{M_1'}[\omega^2M_1{}^{IV}(L_c{}^{IV}+L_g{}^{IV}+2M_2{}^{IV})+(R_c{}^{IV}R_g{}^{IV}-\omega^2L_c{}^{IV}L_g{}^{IV}\\&+\omega^2M_2{}^{IV2})]C_h{}^{IV}-\frac{1}{M_1'}[\omega^2L_g{}^{IV}M_1{}^{IV}]C_q{}^{IV}-\frac{1}{M_1'}[\omega^2L_c{}^{IV}M_1{}^{IV}]C_v{}^{IV}.\end{aligned}$$

The manner in which eq. (18) is derived will be clearly understood by referring to eqs. (15), (16), and (17). The prime superscripts refer only to the sequence of Hartshorn bridge operations for the evaluation of κ, and have no significance for the inductance bridge and its eqs. (9) and (10). Thus, for example, R_a', L_a', etc. of eq. (18) are identical to R_a, L_a, etc., of eqs. (9) and (10). There is a similar identity between $R_c{}^{IV}$, $L_c{}^{IV}$, etc. and R_c, L_c, etc., whereas R_a'', L_a'', etc. have no counterpart in the inductance bridge.

4. DESCRIPTION OF RESISTORS

The special resistors used in the inductance bridge are of such a design that they can be directly measured by means of the resistance comparator

(Kelvin Double Bridge built by Eppley Laboratories) against the reference standards of the same nominal value.

It is obvious that the resistance of R_1 obtained from the inductance bridge via eq. (13) is its value at 100 c.p.s., whereas the only link between R_1 and the present N.R.C. unit of resistance is the comparator, in which only direct current can be used. Accordingly, the question of the equivalence of a resistance in a-c. and d-c. is one that has been carefully examined with respect to our method, as well as with other a-c. methods for the absolute ohm. This agrees with the generally accepted principle that a resistor made of highly stranded wire shows no significant change of resistance between d-c. and a low frequency such as 100 c.p.s.

In the case of R_2 and R_c, the question is less critical because these resistances appear in the main term of eq. (13) only as a ratio. If all the resistances involved change in the same way with frequency, the compensation is complete, and d-c. measurements are correct.

The procedure established here is that all main bridge components whose resistance has to be known with high precision will be made with stranded wire and will be calibrated in d-c. only. The mechanical parts, with the exception of copper connecting bars, are non-metallic. The type of construction is shown in Fig. 6, the terminals shown corresponding to those on R_1. The other resistors will have a different arrangement of bars and terminals to suit their particular application.

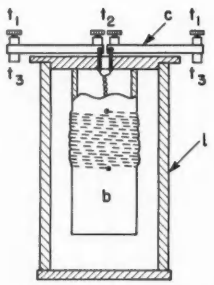

FIG. 6. Stranded resistor R_1 used in inductance bridge circuit. t_1 and t_3 are current terminals, t_2 potential terminals. Other stranded resistors are of similar construction.

The 1-ohm resistor R_1 is made by twisting 20 strands of No. 26 double silk-covered manganin wire into a cable, and arranging this cable as a twisted bifilar coil on a bakelite cylinder b, $2\frac{1}{4}$ in. in diameter and 6 in. long. This is mounted in a protective container of lucite l. A number of holes are cut in the bottom and sides of the lucite container to permit oil to enter freely and surround the resistance coil.

The copper bars C are provided with terminals or mercury contacts to make the necessary connections in the bridge. The screw terminals t_1 and t_2 are the current and potential terminals respectively. In the resistance comparator the amalgamated contacts t_3 are used instead of t_1.

The resistance R_2 in Fig. 1 is made up of a resistor R_2' with a nominal value of 28.6 ohms shunted by a good quality decade box S_2, where the shunting resistance is of the order of 6000 ohms. The resistor R_2' is made of 10 strands of No. 30 double silk-covered manganin wire, twisted and mounted in the same manner as for R_1. The arrangement of copper bars and terminals is shown in Fig. 10.

The resistance R_c of the primary circuit of M_2 (manganin) is measured *in situ* by a substitution method in an auxiliary Wheatstone bridge. The substitution resistor R_c', with the same nominal value (27.3 ohms) as R_c, is made in the same manner as R_2', as is the other arm of the Wheatstone bridge. The ratio arms are two resistors of 100 ohms each. The arrangement of copper bars and terminals is shown in Fig 13. Photographs of resistors R_1, R_c', and R_2' are shown in Fig. 24.

The calibration of R_2' (28.6 Ω) and R_c' (27.3 Ω) can be made on the resistance comparator in terms of any nominal 1 Ω resistor. For this measurement duplicates of these resistors were built and used in the resistance comparator. The reference is a special resistor built according to the diagram, Fig. 7. Its sections are good quality coils made by Tinsley Co. and can be directly compared with the standards or the sections of standard decades of the same nominal value. The values 28.6 and 27.3 Ω can be obtained by a suitable choice of potential terminals.

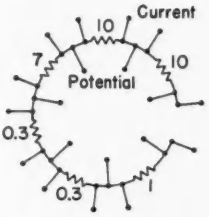

FIG. 7. Reference resistor used as a connecting link between the standards and stranded resistors R_2' and R_c'. All values are in ohms.

In the Hartshorn bridge comparisons, the resistance, also called R_1, is small, and is one of the variables used to establish the bridge balance. A slide wire type of variable resistance was adopted for this purpose.

The resistor acting as the "slide wire" is a brass tube 1 meter long and $\frac{3}{4}$ in. in outside diameter, mounted side by side with another similar brass tube which serves simply as a potential lead. A short brass bar, carrying two spring-loaded sliding contacts of the sleeve type, bridges the two tubes. The instrument is shown in Fig. 8.

All terminals are located at one end of the assembly and connecting wires are placed inside the resistor tube. The two current terminals are connected to the extreme ends of the tube. One potential terminal is connected to the sliding contact, and by a choice of one of three other terminals, the fixed potential point may be located at either end of the tube or at its center.

This instrument was calibrated by means of a potentiometer, and has a nominal resistance of 8 $\mu\Omega$ per cm.

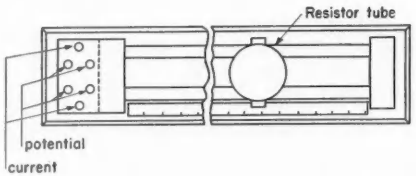

FIG. 8. Slide wire type potentiometer (see Fig. 4).

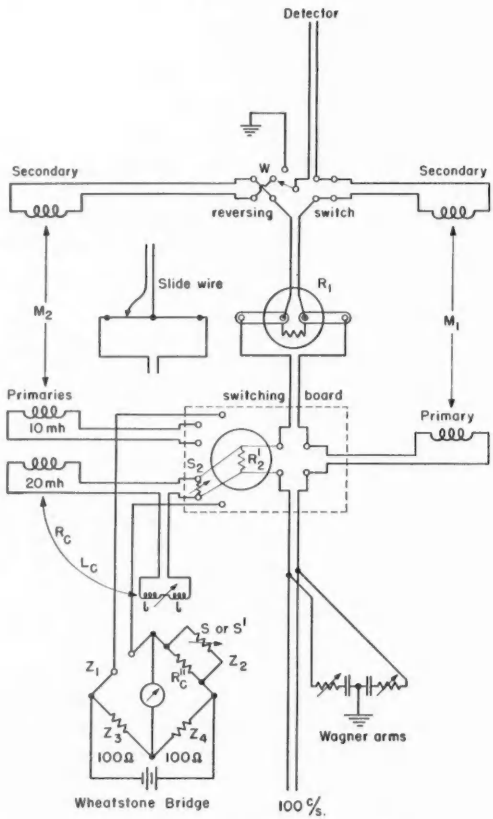

FIG. 9. General plan of inductance bridge, showing how the conversion into Hartshorn bridge can be made on the "switching board". The Hartshorn bridge uses both polarities for mutual inductors, i.e. combinations similar to (*a*) and (*b*) in eqs. (1) and (2). They are obtained by means of "reversing switch" (in which *w* establishes the Wagner ground in all cases). For arrangements of connections on "switching board" see next figures.

The general arrangement of components used in the absolute ohm measurement is shown schematically in Fig. 9. The actual appearance of the switching board is shown in Figs. 10 to 13 for each of the four main operations.

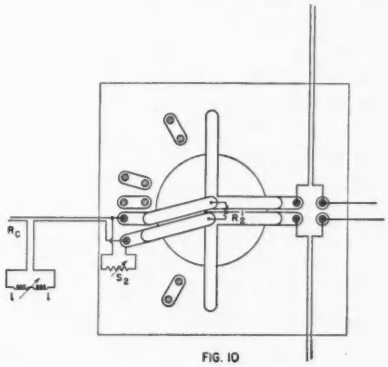

FIG. 10

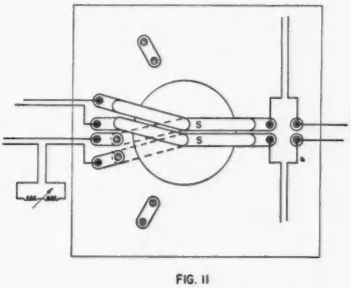

FIG. 11

FIG. 10. Switching board for inductance bridge: R_2' is a shunt across R_c and is made adjustable by means of S_2.

FIG. 11. Switching board for the Hartshorn bridge: the central plate (without a resistor) is simply used to support the copper bars S S that introduce into the circuit the primary of either a 10 mh. or a 20 mh. inductor (so-called Horizontal or Manganin inductors).

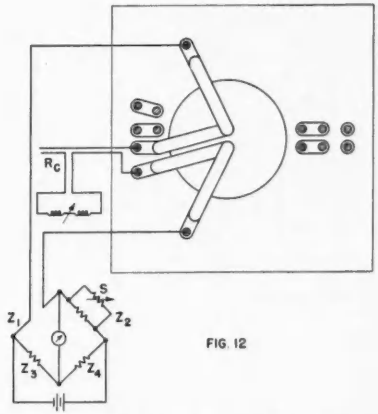

FIG. 12

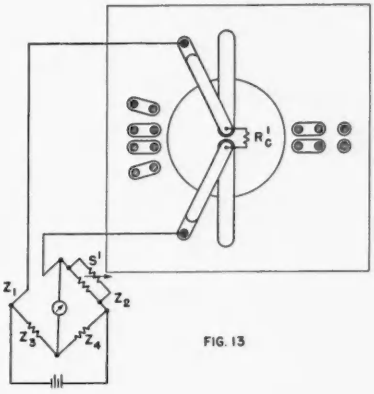

FIG. 13

FIG. 12. Switching board for the measurement of R_c, which is in the arm Z_1 of the Wheatstone bridge.

FIG. 13. Second phase of R_c measurement: R_c is replaced by R_c'. The configuration of copper block remains the same as in Fig. 12.

The inductance bridge is set up by mounting R_2' on the switching board and placing two copper bars between the potential terminals and the primary terminals of M_2 (20 mh.), as shown in Fig. 10. R_1 (1 ohm) is in the circuit, as shown in Fig. 9. The desired polarity of M_1 and M_2 is obtained by the proper

position of the reversing switch. The shunt S_2 and the variable inductance are shown schematically.*

To change over to the Hartshorn bridge, Fig. 11, resistor R_2' is replaced by a plate carrying simply two parallel bars corresponding to the parallel bars on R_2'. Connections can then be made to either pair of M_2 primary terminals. R_1 (1 ohm) is replaced by the slide wire.

For the measurement of R_c, R_2' (Fig. 10) is replaced by a plate carrying two short studs to support the connecting bars. Connections to the Wheatstone bridge are made with another pair of bars as shown in Fig. 12. In Fig. 13, R_c is simply replaced by the substitution resistor R_c'.

It is important to note that the configuration of all connections and resistors is preserved through all the measurements. Thus, R_c includes two copper bars, and the junction between R_c and R_2' is the junction between these bars and the potential terminals of R_2'. In the measurement of R_c, these same junction points are connected to the Wheatstone bridge through a pair of bars which are also used in the measurement of R_c'.

5. SOURCE OF VOLTAGE AND DETECTOR CIRCUIT

(1) *Bridge Voltage*

The 100 c.p.s. frequency is supplied by a quartz crystal oscillator (100 kc.) with 100 c.p.s. sine wave output at 1.5 v. r.m.s. It is located in the standard frequency laboratory where it is compared periodically with the main quartz crystals.

The 100 c.p.s. sine wave is fed to a power amplifier through a coaxial cable (RG-9) and a General Radio type B variac for bridge voltage control. The circuit diagram is shown in Fig. 14.

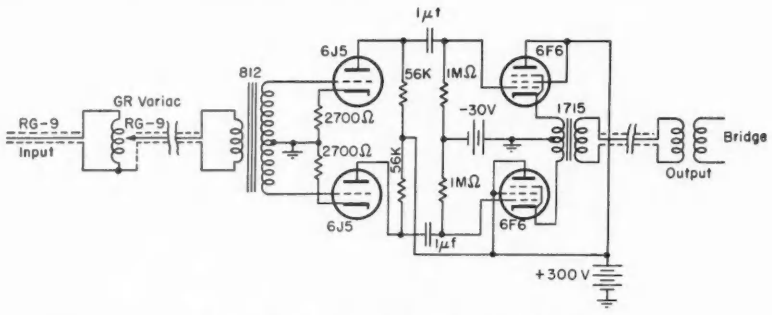

FIG. 14. Bridge voltage (power amplifier).

The cathode follower type of push–pull output has low distortion and is relatively insensitive to changes in load impedance. Therefore a wide variety of bridges can be coupled to this amplifier without any appreciable loss in

*The effect of the connecting copper bars on the shunting process of R_2' by S_2 (Fig. 10) has been shown experimentally as being undetectable.

voltage. The output voltage (6–8 v. r.m.s.) is ample for all our applications. The amplifier is battery operated.

(*2*) *Detector*

The detector circuit is shown in a block diagram, Fig. 15.

The 100 c.p.s band pass filter is a conventional three-section three-element series type. The inductances are toroidal.

The band stop filters are of a type (Dauphinee 1953) shown in Fig. 16. The equation for the e.m.f., e_g, across a load impedance R_g is

$$e_g = \frac{1}{\Delta}\left[\left(R_b R_d + \frac{L_d - M}{C}\right) + j\omega\left\{R_b\left(L_d - \frac{1}{\omega^2 C}\right) - \frac{R_d}{\omega^2 C}\right\}\right] R_g e_a,$$

where Δ is a determinant which need not be known, and e_a is the applied e.m.f.

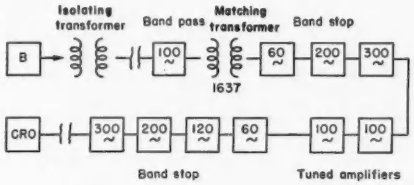

Fig. 15

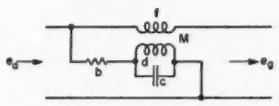

Fig. 16

FIG. 15. Block diagram of detector circuit: B = bridge, CRO = cathode ray oscilloscope. The tuned amplifiers are preceded and followed by filters.
FIG. 16. Band stop filter.

If the network is to behave as a band stop filter, then $e_g = 0$, and therefore

$$R_b R_d + (L_d - M)/C = 0,$$

$$R_b(L_d - 1/\omega^2 C) - R_d/\omega^2 C = 0.$$

If M is a toroidal transformer, unit coupling may be assumed, so that $M = nL_d$ where $n = \sqrt{(L_f/L_d)}$ = turns ratio.

For a given transformer, R_d, L_d, and n are specified. Therefore solving the equations for R_b and C, we have

$$R_b = \frac{\omega^2 L_d^2 (n-1) - R_d^2}{R_d},$$

$$C = \frac{L_d(n-1)}{\omega^2 L_d^2 (n-1) - R_d^2}.$$

Using the same toroidal transformer design for all the filters, 950 primary turns of No. 26 wire and 6500 secondary turns of No. 32 wire, the values of R_b and C may be quickly computed for each frequency.

The 100 c.p.s. tuned amplifier is shown in Fig. 17. The toroidal transformer has 600 turns on the primary and 2800 turns on the secondary, both of No. 26 wire. The tuning condenser is about 4 μf. and is fixed tuned for each of the two amplifiers. The amplifiers are battery operated; this feature is essential for stability.

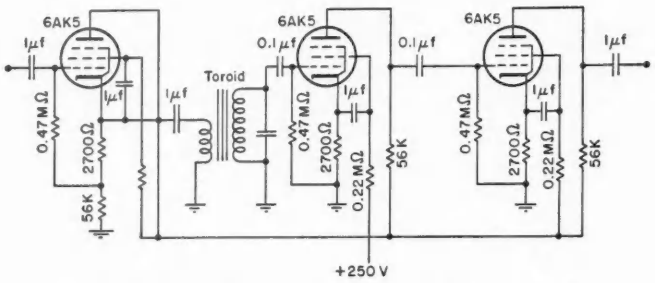

FIG. 17. Diagram of tuned amplifiers in the detector circuit.

The two amplifiers are connected in series. The circuit of the first one is as shown in Fig. 17. In the second one, the last stage is converted to a cathode follower for coupling to the band stop filters.

It is of utmost importance to exclude harmonics of 100 c.p.s. from the detector amplifiers. The second and third harmonics are the most prominent and require the attenuation provided by the band stop filters as well as the band pass. Heterodyne mixing of any two consecutive harmonics produces the 100 c.p.s. fundamental, which results in a false bridge balance.

The frequency 60 c.p.s. and its harmonic 120 c.p.s. produce unwanted deflections on the oscilloscope, and may overload the amplifiers if the signal level is excessive. These frequencies must therefore be suppressed.

The power amplifier and the detector circuit, with the exception of the oscilloscope, are located 50 feet or more from the bridge, and from each other, to avoid interactions. The oscilloscope, a Dumont type 304-H, is the final detecting instrument, and is located in the same laboratory as the bridge. It is placed so that the screen is easily viewed by the observers who are performing the various bridge balancing operations.

6. MEASUREMENT OF INTERCAPACITANCES AND SELF-CAPACITANCES

The determination of intercapacitances is made by means of the Hartshorn bridge and its resistive equation. All terms in this equation are of the form $[K]x$, x being a residual capacitance, i.e. a small quantity. Thus, for the computation of $[K]$, medium precision values of components are sufficient. In particular, we can assume that for a certain position of the reversing switch,

$$M_1 = -m, \qquad M_2 = +m, \qquad R_1 = R_1',$$

and for reversed polarities

$$M_1 = +m, \qquad M_2 = -m, \qquad R_1 = R_1''.$$

Introducing these values into (14) we easily obtain

$$(19) \qquad (R_1'+R_1'')/2 = \omega^2(R_cL_g+R_gL_c)C_h+\omega^2(R_aL_f+R_fL_a)C_k,$$

so that the intercapacitance on any inductor (say C_k) can be deduced from the intercapacitance of one of them (C_h) considered as reference inductor.

The intercapacitance of the reference inductor itself can be obtained only by a comparison of two geometrically identical inductors, on which it is possible to assume that the intercapacitances are equal:

$$C_k = C_h = C_i.$$

Then

$$(20) \qquad C_i = \frac{R_1'+R_1''}{2\omega^2(R_cL_g+R_gL_c+R_aL_f+R_fL_a)}.$$

For self-capacitances, the procedure based on the identity of two secondaries would not be sufficiently accurate. The value of a self-capacitance is an order of magnitude larger than C_h and C_k and depends on many factors (such as dielectrics, spacing of turns, degree of humidity, etc. . . .) so that two apparently identical coils may have quite different self-capacitances.

By means of the formula (14) we can compare self-capacitances (the intercapacitances being considered as known) but the first self-capacitance (of a reference coil) has to be determined by the resonance method. The resonance of a secondary of Campbell's type inductor occurs at a frequency of several kilocycles per second, so that the question arises about the validity of the values obtained at this frequency, if the secondary is used at 100 c.p.s. It is a well-known fact that the properties of multilayer coils are very variable with frequency but, on the contrary, that single layer coils are quite independent of frequency, at least with the relatively narrow limits in which we operate.

A special inductor was built to serve as reference for self-capacitance determinations, Fig. 23. Its secondary is a single layer coil the self-capacitance of which is measured by the method represented in Fig. 18. The capacitance

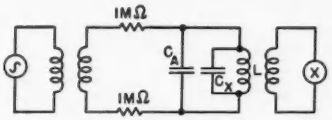

FIG. 18. Circuit for resonance measurement; L is the self-inductance and C_x the self-capacitance of the coil under test.

C_x represents the distributed self-capacitance of the coil; C_A is an added capacitance (not exceeding 1000 $\mu\mu$f.) by means of which the resonance fre-

quency can be adjusted to occur at a series of suitable values. At the resonance frequency f we have

$$C_x = 1/4\pi^2 f^2 L - C_A. \tag{21}$$

The self-capacitance was found to be very low (of the order of 30 $\mu\mu$f.). It plays only a small role with respect to the capacitances of leads connecting the measured inductors to one another.

The reference single layer secondary can be used with two different sections of the primary to give 10 or 20 mh.; it is designated as *Single Layer Inductor* (10 mh.) or (20 mh.).

So far as the self-capacitances of various primary windings are concerned we found that they are much smaller than the self-capacitance of the reference single layer secondary and as they are also accompanied by small coefficients, we finally had to conclude that they are practically negligible. Therefore the quantities designated by C_u or C_v represent only the capacitances of coaxial cables leading to the primaries. These can be measured with an ordinary capacitance bridge. It is to be noted that for the same reason the same conclusion was made concerning the primary of the Manganin Inductor.

By means of the formula (14) in which now the quantities C_h, C_k, C_u, C_v are considered as known and $C_q = C_0$, the self-capacitance of the single layer secondary, as given by the resonance method, we obtain

$$C_p = -\frac{R_1' - R_1''}{2m\omega^2 R_f} + \frac{R_c + R_g}{R_f} C_h - \frac{R_a + R_f}{R_f} C_k + \frac{R_g}{R_f} C_0 - \frac{R_a}{R_f} C_u + \frac{R_c}{R_f} C_v. \tag{22}$$

If the single layer inductor is on the side of M_1, i.e. if $C_p = C_0$, then

$$C_q = +\frac{R_1' - R_1''}{2m\omega^2 R_g} - \frac{R_c + R_g}{R_g} C_h + \frac{R_a + R_f}{R_g} C_k + \frac{R_f}{R_g} C_0 + \frac{R_a}{R_g} C_u - \frac{R_c}{R_g} C_v. \tag{23}$$

The order of intercomparison can be conveniently arranged so as to follow the sequence of computations necessary for the orderly extraction of all capacitance values.

7. MEASUREMENT OF RESIDUAL INDUCTANCES

The residual inductances λ_1 and λ_2 of the resistors R_1 and R_2' are measured by a substitution method. The substitution resistors consist of single loops of manganin wire with computed self-inductances nominally equal to λ_1 and λ_2. The bridge used for this measurement is shown in Fig. 19. The ratio arms are 96 Ω resistors constructed in the same manner as the 28.6 and 27.3 Ω resistors. The 100 c.p.s. voltage and detector circuit of the Hartshorn bridges are used without modification.

The arm Z_2 consists of three components:

(1) Resistance R with its self-inductance λ (R represents either R_1 or R_2' or the corresponding substitution resistor).

(2) Small variable resistance σ with a small and constant self-inductance l.

(3) Small variable inductance L with a small and constant resistance r.

The resistances σ and r are kept as small as possible so that the resistors

nominally equal to R_1 and R_2' used in other operations may be placed in arm Z_1.

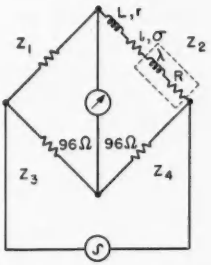

FIG. 19. Impedance bridge for residual inductance measurement.

The balance equation of the bridge is

$$Z_1Z_4 = Z_2Z_3. \tag{24}$$

If this equation is solved for λ, we have

$$\lambda = K - L. \tag{25}$$

K is a constant made up of the components of arms Z_1, Z_3, and Z_4, as well as the small inductance l of arm Z_2. The resistance $R+\sigma+r$ of arm Z_2 is eliminated. The differential form of eq. (25) is

$$\Delta\lambda = -\Delta L. \tag{26}$$

In general, the design of the substitution resistor is a trial and error operation, unless some prior knowledge of the approximate value of λ is available. Such knowledge may come from a previous lower precision measurement, or from a different method of higher precision, in which case the present method serves as a confirmation. If such experiments are lacking, then it will be necessary to turn to the general knowledge that resistors within a specified range of resistance, and of a certain type of construction, will have a residual inductance of a certain order of magnitude, e.g. 1 μh.

When the approximate value of λ is known, it is a relatively simple matter to choose the required diameter of the manganin loop and the size of wire. The difference between the inductance of the resistor and its substitute, i.e. $\Delta\lambda$, should be considerably smaller than λ if any precision is to be achieved. The same consideration does not apply to the resistance inasmuch as this is eliminated from the equation. However, ΔR should be kept small to avoid any change in l when σ is adjusted.

The manganin loop was mounted on the circumference of a bakelite disk and connected through a short twisted lead to a pair of copper blocks identical to those on the resistors. Any interaction between the blocks and loop is negligible. The following loops were made:

(1) R_1 substitution loop; diameter 16.1587 cm., No. 23 manganin wire. Computed inductance = 0.6036 μh.

(2) R_2' substitution loop; diameter 26.2474 cm., No. 36 manganin wire. Computed inductance = 1.3125 μh.

The variable resistance σ is a modified form of the Campbell constant inductance rheostat. Since σ is to be kept small, ordinary sliding contacts cannot be used. Two concentric grooves of $\frac{1}{4}$ sq. cm. cross section and about 20 cm. mean diameter were milled in a lucite disk and filled with mercury. A copper bar with amalgamated contacts, mounted on a rotating arm, bridges the two mercury-filled grooves. A copper compensating wire runs in a third concentric groove between the mercury grooves. The system is shown schematically in Fig. 20.

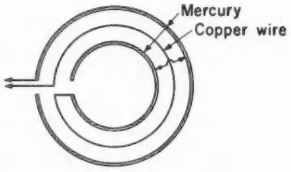

FIG. 20. Variable mercury resistor with constant inductance.

The range of variation of resistance can be chosen by adjusting the relative amounts of mercury in the grooves. The total resistance is a few hundredths of an ohm, depending on the amount of mercury used.

The variable inductance L is similar to the one used in the primary circuit of the 20 mh. manganin inductor. Two coils consisting of three turns of No. 22 copper wire are wound with 1 mm. pitch on the circumference of bakelite disks 10 cm. in diameter and about 5 mm. thick. One coil is fixed, and the other mounted on a lucite screw with 1 mm. pitch. The distance between coils is measured with a centimeter scale and a vernier dial mounted on the end of the screw.

The mutual inductance was computed for three distances, 4, 5, and 6 cm., as follows:

4 cm.	$M = 0.301$ μh.
5 cm.	0.223 μh.
6 cm.	0.168 μh.

Thus calibrated, the mutual inductance for any intermediate distance is easily obtained. Since the total inductance of the circuit is (series aiding)

$$L = l_1+l_2+2m,$$

and since l_1+l_2 is constant,

$$\Delta L = 2\Delta m.$$

Δm can be measured quite accurately by observing the change in distance between coils.

The procedure for measuring λ_1 and λ_2 is as follows:

(1) With resistor R_1 in arm Z_2, and with L and σ set at a convenient mid-position, the bridge is balanced by means of suitable shunt resistors and

condensers in either or both arms Z_3 and Z_4. This operation fixes the value of K.

(2) Replace R_1 with the substitution resistor and rebalance by adjusting σ and L, and use eq. (26) to obtain $\Delta\lambda$.

The procedure is repeated for R_2'.

The two operations can be carried out in the reverse order equally well.

The values of λ_1 and λ_2 are found to be

$$\lambda_1 = 0.6036\ \mu\text{h.},$$

$$\lambda_2 = 1.4450\ \mu\text{h.}$$

For correct operation, this bridge requires a Wagner ground similar to the one for the inductance bridge.

The residual mutual inductance between the leads of the slide wire was compensated by an appropriate mutual inductance between the primary and the secondary circuits (small additional loops of wire). The adjustment of the compensating inductances is made on the Hartshorn bridge in which all secondary windings are replaced by short circuits. This takes care also of all possible similar inductive effects. A Wagner ground balance plays an essential role in these small inductance compensations.

8. DETERMINATION OF THE OHM

The numerical evaluation of k_1, k_2, and κ requires (1) the calculation of coefficients, and (2) the measurement of capacitances and residual inductances.

The coefficients are functions of the large components of the bridges, and are readily measured with sufficient precision on good laboratory instruments.

The measurement of residual inductances λ_1 and λ_2 has been described in a previous section, and numerical values given.

The self-capacitances C_u and C_v of the primary circuits are taken as the capacitance of leads only. Here the coefficients are much smaller than for the secondary circuits, and the self-capacitances of the primary coils alone are small. Therefore the precision required in C_u and C_v is less than for the other capacitances.

The measurement of intercapacitance of an inductor and the self-capacitance of its secondary circuit (including lead) is made on the Hartshorn bridge, using both polarities. The evaluation of all the capacitances requires a series of Hartshorn bridge balances, performed in a certain sequence, as follows:

(*a*) Standard Inductor (10 mh. vertical) vs. Horizontal Inductor (10 mh. horizontal); these inductors are geometrically identical, so that $C_k = C_h$ follows immediately from eq. (20).

(*b*) Standard Inductor (10 mh. vertical) vs. Single Layer (10 mh. horizontal); the intercapacitance of the latter is calculated in terms of the Standard Inductor by eq. (19). The self-capacitance of the Standard Inductor secondary is then calculated in terms of the Single Layer Inductor according to eq. (22).

(*c*) Double Campbell Inductor with top or bottom secondary (10 mh.

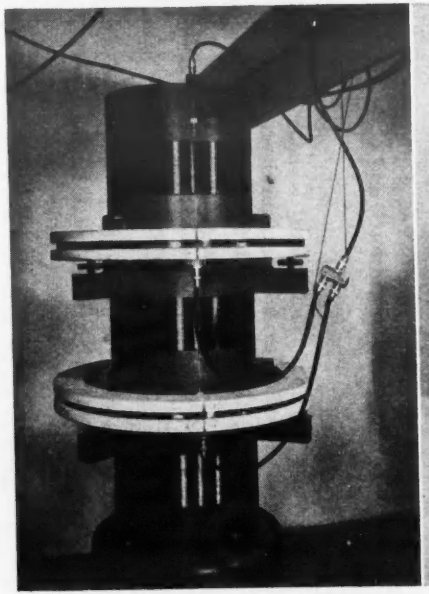

FIG. 21. Double Campbell Inductor.

FIG. 22. Replica of Manganin Inductor.

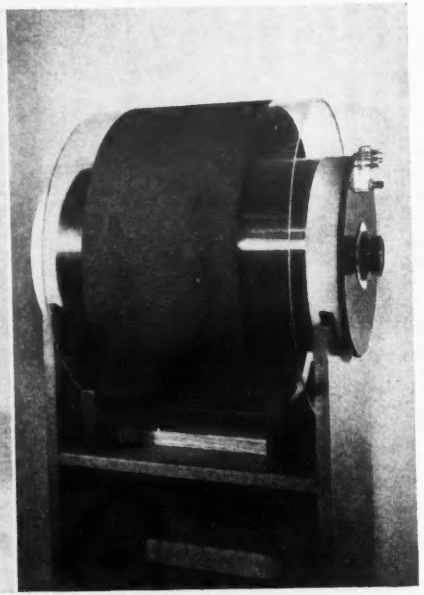

FIG. 23. Single Layer Inductor.

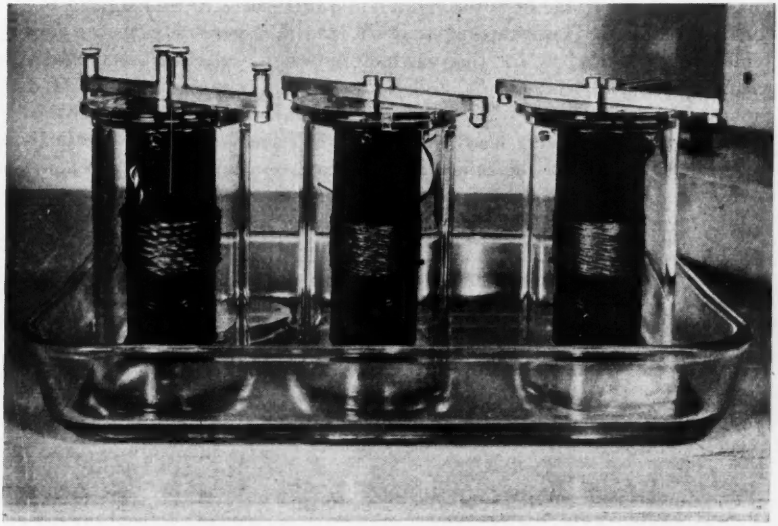

FIG. 24. Resistors R_1 (left), R_c', and R_2'.

vertical) vs. Single Layer Inductor (10 mh. horizontal); the intercapacitances are calculated from eq. (19) in terms of the Single Layer Inductor, and self-capacitances according to eq. (22) as before.

The preceding operations account for all the required intercapacitances and secondary self-capacitances of the 10 mh. inductors. The procedure is similar for the 20 mh. inductors.

(*d*) Manganin Inductor (20 mh. horizontal) vs. a replica of the Manganin Inductor (20 mh. vertical); the intercapacitances $C_k = C_h$ follow from eq. (20) as before.

(*e*) Manganin Inductor (20 mh. horizontal) vs. Single Layer Inductor (20 mh. vertical); the intercapacitance of the Single Layer Inductor is calculated from eq. (19), and the self-capacitance of the Manganin Inductor from eq. (23).

(*f*) Manganin Inductor replica (20 mh. vertical) vs. Single Layer Inductor (20 mh. horizontal); the intercapacitance of the Single Layer Inductor is calculated from eq. (19).

(*g*) Double Campbell Inductor with secondaries in series (20 mh. vertical) vs. Single Layer Inductor (20 mh. horizontal); the intercapacitance of the Double Campbell Inductor is calculated from eq. (19) and the self-capacitance of the secondary from eq. (22).

These capacitances were measured periodically during the course of the work, and were found to vary slightly. A set of typical values of the capacitances appearing in the equations of k_1, k_2, and κ is presented below. The values in parentheses represent the capacitances of the leads only. They have

to be subtracted from the total value if the intrinsic self-capacitances of the coils are required. These capacitances are identified here only by the general symbols C_k, C_p, and C_u for those inductors designated by M_1 and mounted with axes vertical, and C_h, C_q, and C_v for inductors designated by M_2 and mounted horizontally.

The capacitance (with lead) of the Single Layer secondary (vertical) is taken as 300 $\mu\mu$f., and the Single Layer secondary (horizontal) 290 $\mu\mu$f.

M_1	C_k, $\mu\mu$f.	C_p, $\mu\mu$f.	C_u, $\mu\mu$f.
Standard Inductor (10 mh.)	11.3	398.2 (266)	425
Double Campbell Inductor			
Top secondary (10 mh.)	14.3	505.4 (267)	426
Bottom secondary (10 mh.)	11.0	516.9 (267)	426
Series secondaries (20 mh.)	17.4	410.5 (267)	426
M_2	C_h	C_q	C_v
Manganin Inductor (20 mh.)	9.3	540.1 (254)	453

The numerical form of eq. (18) is

$$\begin{aligned}\kappa = {} & 2+2.6278\times10^{5}\times11.3\times10^{-12}+2.1950\times10^{5}\times398.2\times10^{-12}\\ & +0.0648\times10^{5}\times425\times10^{-12}-1.2964\times10^{5}\times14.3\times10^{-12}\\ & -0.8883\times10^{5}\times505.4\times10^{-12}-0.0497\times10^{5}\times426\times10^{-12}\\ & -1.2980\times10^{5}\times11.0\times10^{-12}-0.8883\times10^{5}\times516.9\times10^{-12}\\ & -0.0497\times10^{5}\times426\times10^{-12}+4.3763\times10^{5}\times17.4\times10^{-12}\\ & +3.8294\times10^{5}\times410.5\times10^{-12}+0.0995\times10^{5}\times426\times10^{-12}\\ & -2.2368\times10^{5}\times9.3\times10^{-12}-2.9135\times10^{5}\times540.1\times10^{-12}\\ & -0.1113\times10^{5}\times453\times10^{-12}\\ = {} & 2+5.2224\times10^{-6}-3.5672\times10^{-6}-2.2836\times10^{-6}\\ = {} & 2-0.6284\times10^{-6} = 1.99999937.\end{aligned}$$

In the same manner, using eqs. (9) and (10),

$$k_1 = -0.72693\times10^{-2},$$

$$k_2 = +1.76675\times10^{-5}.$$

During the month in which our final measurements were made, these three constants showed a slight but orderly evolution as a consequence of the observed variation of the capacitances. There was no difficulty interpolating to have the values of the constants for each day of observation. The numerical values of k_1, k_2, and κ quoted above are values measured on April 26, 1957.

On each day of observation it was generally possible to make several balances of the inductance bridge and auxiliary Wheatstone bridge, from which a set of values of R_2 and R_c was obtained. Here is a set of values obtained on April 26, 1957, the same day as the values of k_1, k_2, and κ quoted above were measured:

$$R_2' = 28.63382_{52}\ \Omega,$$
$$R_c' = 27.21491_{14}\ \Omega,$$
$$R_c'' = 27.3209\ \Omega.$$

These values were obtained on the d-c. resistance comparator.

(1) Inductance bridge balance,

$$S_2 = 5623.0\ \Omega;$$

therefore $R_2 = (R_2'S_2)/(R_2'+S_2) = 28.4887529\ \Omega$.

(2) Wheatstone bridge balances,

$$S = 3147.6\ \Omega,$$
$$S' = 7266.0\ \Omega;$$

therefore $R_c = R_c' \times (S/S') \times (R_c''+S')/R_c''+S) = 27.0821712\ \Omega$.

Substitute numerical values into eq. (13):

$$R_1 = -\frac{k_1}{2(R_2+R_c)}+\left[\frac{(\kappa-1)R_2-R_c}{R_2+R_c}\omega^2 M_1^2+\frac{k_2\omega^2 M_1}{R_2+R_c}\right]^{\frac{1}{2}}$$

$$= 0.0000654+\left[39.5356667\times\frac{0.99999937\times 28.4887529-27.0821712}{55.5709241}\right.$$
$$\left.-0.0012560\right]^{\frac{1}{2}}$$

$$= 0.9997839\ \Omega_A.$$

Ω_A designates the unit of resistance determined by our method. The value of R_1 measured on the resistance comparator in terms of the N.R.C. reference standards, i.e. the resistors that maintain the unit of our laboratory, designated here by Ω_L, is

$$R_1 = 0.9997898\ \Omega_L.$$

Equating both values of R_1 for this particular measurement, we find

$$\Omega_L = (1-5.9\times 10^{-6})\Omega_A.$$

A total of 102 such measurements were made, and the average result is

$$\Omega_L = (1-8.2\times 10^{-6})\Omega_A.*$$

If the deviations of individual observations were recorded from -8.2×10^{-6} taken as the origin, the distribution of points is found to be reasonably symmetrical, approximately following a gaussian curve, with a strong concentration in the region -5×10^{-6} to $+5\times 10^{-6}$. More than 80% of the points lie within the limits $\pm 20\times 10^{-6}$.

*In 1955 the comparison made in the International Bureau of Weights and Measures gave

$$\Omega_L = (1-5.2\times 10^{-6})\ \Omega_{B.I.P.M.},$$

$\Omega_{B.I.P.M.}$ being the unit maintained in the International Bureau. New B.I.P.M. intercomparisons will take place in the summer of 1957.

9. DISCUSSION OF ACCURACY

The accuracy of the final result is affected by (1) accidental errors, and (2) systematic errors.

So far as accidental errors are concerned our conclusion is, of course, similar to that of all previous experimenters, namely that the accidental errors are eliminated statistically by making a sufficiently large number of measurements. While it is obvious that the number of measurements of R_1 actually made (over 100) cannot be considered as being very large, nevertheless the conclusions reached in the foregoing pages probably would not have been altered appreciably by the doubling or tripling of that number.

Our main objective in this discussion is to examine the method from the point of view of systematic errors. By definition, a systematic error is a quantity that cannot be evaluated. Only its upper limit can be estimated.

The method possesses a number of important characteristics which tend to reduce the magnitude of systematic errors. The most notable feature is that the method uses essentially the same electrical network (Hartshorn Bridge) for all measurements at 100 c.p.s. (except λ_1 and λ_2). It possesses therefore certain of the qualities which we generally associate with the "substitution" method. It can be readily shown that the errors on the components which are common to the sequence of comparison bridges *and* the Inductance Bridge itself have little influence on the final result. Any systematic errors on the self-capacitance of the secondary coil of the Manganin Inductor M_2 (C_q^{IV}), for example, or the Standard Inductor M_1 (C_p'), will produce a change in κ that will be almost completely compensated by a change in k_2. The effect of such errors on R_1, through k_1, is always small compared to κ and k_2.

The error on the value of the self-capacitance of the single-layer reference coil affects all self-capacitances by the same amount, and can be shown to have only a small total effect on R_1.

The influence of errors on the Double Campbell Inductor is of a different nature, because this inductor is not a part of the Inductance Bridge. Nevertheless, there is partial compensation between its 10 mh. portions (secondaries taken individually) and the 20 mh. combination (secondaries in series). This is readily seen by examining the second, third, and fourth lines in the numerical equation of κ quoted in Section 8. The measurement of the self-capacitances of the secondaries of the Double Campbell Inductor, individually and in series, is the largest single source of error. Intercapacitances of the Double Campbell Inductor, as well as of all other inductors, are much less important. As for primary self-capacitances, knowledge of capacitance of the leads alone is sufficient.

The evaluation of the ratio $(R_2-R_c)/(R_2+R_c)$ has to be made with great care. All precautions were taken in the design of the switching board to ensure a good reproducibility of geometrical configurations of copper blocks and mercury contacts. The resistors R_2' and R_c' are identical in construction and have the same temperature coefficients. Their calibration benefits from

the fact that the portion of the "reference unit" corresponding to R_c' is common. The differential error can come only from the last two sections ($1\Omega+0.3\Omega$) and this is likely to be negligible.

The measurement of λ_1 and λ_2 (of which λ_1 is more critical) is made with an entirely different network, and brings some errors of its own. However, the extreme care with which the substitution resistors were adjusted and measured, and the repetition of measurements over several years, established confidence in the values of λ_1 and λ_2.

The formulae for all the derivatives of R_1 with respect to the C's, λ's, R_2, and R_c were established in order to examine the relative effects of these various parameters on the final result. The statements made above are based on relations clearly shown by these derivatives. A long series of measures and checks points out that the precision on the self-capacitances associated with the Double Campbell Inductor can, with reasonable care, be made sufficiently high to keep the error on R_1 below 5×10^{-6}. The total error on all the rest of the parameters contributes about the same amount. Thus we can assign a total probable error of $\pm10\times10^{-6}$ due to electrical measurements. The error on the frequency (100 c.p.s.) is considered to be negligible. In the paper on the Standard Mutual Inductor it is stated that the figure of 13 parts in a million is considered to be very definitely an upper limit rather than a probable error on the computed mutual inductance M_1. The total probable error on R_1 can thus be considered as not exceeding $\pm20\times10^{-6}$, half of electrical, and half of mechanical origin.

It is entirely possible that with further refinements in instruments and technique, this error could be somewhat reduced.

Several experiments are being carried on in various countries at the present time. When the results of all these become known it will be possible to estimate how well the unit of resistance is known.

APPENDIX I

An example of Kron's Matrix Mesh Method for the solution of electrical networks will be presented for the inductance bridge, Fig. 1, with one small component, e.g. C_p. Since the secondary terms in the equation are independent of one another, they may be conveniently obtained by solving the network with one small component at a time.

Subject to the condition that the relative directions of currents and e.m.f.'s in branches a and f, and c and g, must correspond to the convention for the sign of M adopted in Section 1, the positive directions of currents and e.m.f.'s in branches and meshes are arbitrarily chosen as shown by the arrows, Fig. 25.

Branch and mesh currents and e.m.f.'s are put in the form of single column matrices, represented by the symbols i and e for the branches, and i' and e' for the meshes. The relation between the branch and mesh currents is given by the matrix equation

$$i = Ci'. \tag{27}$$

Combining matrix C and its transpose C_t with the impedance matrix Z,

$$Z' = C_t Z C. \tag{28}$$

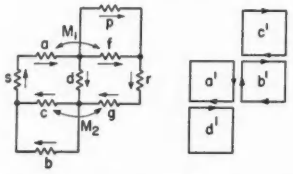

FIG. 25. Diagrams of branches and meshes related to the circuit of Fig. 1.

The complete general solution of the network may be written down as the matrix equation

$$i = C(Z')^{-1} C_t e \tag{29}$$

where $(Z')^{-1}$ is the inverse of Z', and its elements Y are defined in terms of the elements X and determinant Δ of Z' by the relation $Y_{tj} = \partial\Delta/\partial X_{jt}$. The special solution for the network, Fig. 25, is

$$i_r = \underset{\text{row 8, column 9}}{[C(Z')^{-1} C_t]} e_s = \frac{1}{\Delta} Y_{21} e_s = 0. \tag{30}$$

This condition requires that $Y_{21} = 0$. Solving for Y_{21}, we obtain finally

$$\begin{aligned} Y_{21} = {} & R_1(R_2+R_c)+\omega^2 L_c M_1 \\ & +[\omega^2(R_2M_2-R_1L_c)R_f-\omega^2R_1(R_2+R_c)L_f]C_p \\ & +j\omega\{R_1L_c-R_2(M_1+M_2)-R_cM_1 \\ & +[R_1(R_2+R_c)R_f+\omega^2(R_2M_2-R_1L_c)L_f]C_p\} = 0. \end{aligned}$$

This equation should be compared with eqs. (9) and (10).

APPENDIX 2

The Wagner Ground for the inductance bridge, or the Hartshorn bridge, is established by means of the circuit shown in Fig. 26.

The two impedances a and f are connected across the bridge voltage source and their junction grounded. To make the Wagner Ground, one side of the detector is connected to ground by means of a switch, from position 1 to 2. If this bridge can be balanced by a suitable adjustment of a and f, then when the inductance or Hartshorn bridge is re-established and balanced, the detector terminals will be at ground potential.

The symbols used in the network of Fig. 26 should not be confused with those used elsewhere. The network may be put into a more convenient form, Fig. 27.

The solution of this circuit can be put into the general form

$$i_d = \frac{1}{\Delta}[AR_a-BR_f-CX_a+DX_f+j(AX_a-BX_f+CR_a-DR_f)]e_k = 0,$$

or

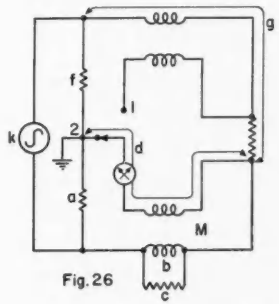

Fig. 26

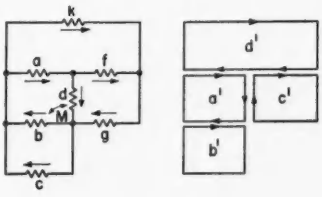

Fig. 27

FIG. 26. Wagner ground for inductance bridge.
FIG. 27. Diagrams of branches and meshes related to Fig. 26.

$$AR_a - BR_f = CX_a - DX_f, \tag{31}$$

$$CR_a - DR_f = -(AX_a - BX_f), \tag{32}$$

where (1) for the inductance bridge,

$$A = R_g(R_c+R_b) - \omega^2 L_b L_g, \qquad B = R_c R_b,$$
$$C = \omega[L_g(R_c+R_b) + R_g L_b - MR_c], \qquad D = \omega(R_c L_b + MR_c);$$

(2) for the Hartshorn bridge,

$$A = R_g, \qquad B = R_b,$$
$$C = \omega(L_g - M), \qquad D = \omega(L_b + M).$$

It is now possible to deduce the conditions for which eqs. (31) and (32) will be valid.

(1) Let $R_a/R_f = R$, R real and positive;

$$X_a/X_f = X, \quad X \text{ real.}$$

Substitute in eqs. (31) and (32), and divide one by the other:

$$(AR-B)/(CR-D) = -(CX-D)/(AX-B). \tag{33}$$

(2) Let $(AB+CD)/(A^2+C^2) = p$, p real;

$$(B^2+D^2)/(A^2+C^2) = q, \quad q \text{ real and positive.}$$

From eq. (33), it follows that

$$RX - p(R+X) + q = 0. \tag{34}$$

(3) Let $X = \lambda R$, λ real.

Substituting in eq. (34),

$$\lambda R^2 - p(\lambda+1)R + q = 0. \tag{35}$$

Solve for R:

$$R = \frac{p(\lambda+1)}{2\lambda} \pm \left[\frac{p^2(\lambda+1)^2}{4\lambda^2} - \frac{q}{\lambda}\right]^{\frac{1}{2}}. \tag{36}$$

For the condition that R is real, $p^2(\lambda+1)^2/4\lambda^2 \geqslant q/\lambda$.

(4) Let $\delta = (p^2-2q)/p^2$, δ real.

Therefore from the above condition,

$$\lambda^2+2\delta\lambda+1 \geqslant 0. \tag{37}$$

The limiting values of λ are given by the equation $\lambda^2+2\delta\lambda+1 = 0$. Therefore

$$\lambda_{\text{limit}} = -\delta \pm \sqrt{(\delta^2-1)}. \tag{38}$$

Since λ is real, it follows that $\delta^2 \geqslant 1$ or $-1 \geqslant \delta \geqslant +1$.

From the equation $\delta = (p^2-2q)/p^2$, we see that δ cannot be greater than $+1$. Therefore $\delta \leqslant -1$ are the only possible values of δ; and λ and X are consequently positive.

Finally, from eq. (36), p is positive; and from $\delta = (p^2-2q)/p^2 \leqslant -1$, $p^2 \leqslant q$.

(5) Given the values of A, B, C, and D, compute p and q. These must be real and positive, and $p^2 \leqslant q$. If these conditions are satisfied, then $\delta = (p^2-2q)/p^2$ is a possible value. The value of δ so obtained defines two sets of positive values of λ whose limits are given by eq. (38), i.e.

$$0 \leqslant \lambda \leqslant -\delta - \sqrt{(\delta^2-1)},$$
$$-\delta+\sqrt{(\delta^2-1)} \leqslant \lambda \leqslant +\infty.$$

If $\delta = -1$, λ can take any value between 0 and $+\infty$.

(6) In principle, the choice of λ is arbitrary, subject only to the limits given above. In practice, the choice of λ is restricted by the physical realization of the ratios R and X in a network. These ratios should not be excessively large or small.

Substituting the values of p, q, and λ into eq. (36), obtain the ratio $R = R_a/R_f$. The ratio of reactances is then $X = X_a/X_f = \lambda R$.

(7) We may now proceed in one of two ways:

(*a*) Choose R_a and R_f, and solve for X_a and X_f, using eqs. (31) and (32).

$$X_a = \alpha R_a - \beta R_f,$$
$$X_f = \gamma R_a - \alpha R_f.$$

(*b*) Choose X_a and X_f, and solve for R_a and R_f:

$$R_a = -\alpha X_a + \beta X_f,$$
$$R_f = -\gamma X_a + \alpha X_f,$$

where $\alpha = (AB+CD)/(BC-AD)$, $\beta = (B^2+D^2)/(BC-AD)$, $\gamma = (A^2+C^2)/(BC-AD)$.

REFERENCES

DAUPHINEE, T. 1953. Electronics, **26**, 254.
HARTSHORN, L. 1925. J. Sci. Instr. **2**, 145.
HENDERSON, J. T. and ROMANOWSKI, M. 1955. Can. J. Phys. **33**, 871.
ROMANOWSKI, M. 1952. Can. J. Phys. **30**, 631.

Under this heading brief reports of important discoveries in physics may be published. These reports should not exceed 600 words and, for any issue, should be submitted not later than six weeks previous to the first day of the month of issue. No proof will be sent to the authors.

The Velocity of Sound in a 2.7% He^3–He^4 Mixture

Although many thermodynamic properties of liquid mixtures of He^3 and He^4 have been measured, no measurements of the velocity of sound in such mixtures have been reported in the literature. This letter reports the results which we have obtained for a 2.7% He^3 concentration; the measurements are currently being extended to other concentrations.

The apparatus used was similar to that described by Guptill *et al.* (1955) and consisted of a cylindrical tube of piezoelectric material (barium titanate) filled with the liquid under study. By introducing acoustic energy of the correct frequency, standing waves were set up in the liquid corresponding to radial modes of propagation, and the velocity of these acoustic waves could be calculated from a knowledge of the internal radius of the cylinder and the difference in frequency required to produce successive resonances.

The barium titanate tube was mounted with its axis vertical in a brass chamber immersed in a bath of He^4. It was filled with liquid He^3–He^4 by condensation of a gaseous mixture fed into the chamber through a fine tube provided for that purpose. The frequencies employed in this experiment lay in the range 1.7 Mc./s. to 2.0 Mc./s.

Because the barium titanate contracts by an unknown amount on cooling to liquid helium temperatures, it was decided to use the results obtained in pure He^4 by van Itterbeek and Forrez (1954) using an acoustic interferometer, to calibrate the apparatus. Accepting their value for the velocity of sound and our determinations of the frequency difference between successive resonances at 2.74° K., an effective low temperature value for the diameter of the barium titanate tube was calculated and used to determine all the other velocities reported here. The upper curve in Fig. 1 was drawn from the results of van Itterbeek and Forrez (1954) and the closed circles on this curve represent values obtained with the present apparatus. It can be seen that good agreement is obtained.

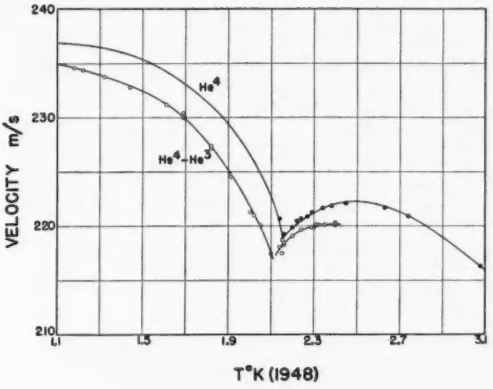

FIG. 1.

The temperature variation of velocity in the 2.7% mixture is shown by the lower curve in the figure. The curve resembles that for pure He^4 except for a displacement of the whole curve to lower temperatures by an amount equal to the depression of the λ-point (0.07° K.), and to lower velocities by between 2 and 3%. The resemblance is not, however, exact, since it can be seen from the figure that slight differences in shape do exist.

An interesting feature of the results is that resonances in the liquid could not be observed above 2.4° K. because of an apparent high attenuation. By contrast, measurements were readily made in pure He^4 up to 4.2° K., and up to 2.75° K. in another mixture containing 2.4%

He^3. The attenuation in the 2.7% mixture on either side of the λ-point and at the lowest temperatures appeared to be somewhat less than in pure He^4.

The figure of 2.7% given for the concentration of He^3 in the mixture is a mass spectrographic determination in terms of the relative atomic abundances. A calculation using the observed λ-point depression and the "two-thirds power law" (Daunt 1952) gave a value of 3.4%. The difference between these two figures is not felt to be significant because there was some uncertainty in the absolute calibration of the mass spectrometer.

The authors would like to express their thanks to Mr. J. R. Keyston for his assistance in making these velocity measurements, and to Drs. R. M. Farquhar and R. D. Russell for their mass spectrographic determination of the He^3 concentration. They are also indebted to the National Research Council of Canada and to the Ontario Research Foundation for grants in aid of research.

Daunt, J. G. 1952. Advances in Phys. **1**, 254, Equation (31).
Guptill, E. W., Hoyt, C. K., and Robinson, D. K. 1955. Can. J. Phys. **33**, 397.
van Itterbeek, A. and Forrez, G. 1954. Physica, **20**, 133.

Received September 19, 1957.
Department of Physics,
University of Toronto,
Toronto, Ontario,
and
Department of Physics,
Dalhousie University,
Halifax, Nova Scotia.

C. C. Lim*
A. C. Hollis Hallett*
E. W. Guptill†

*University of Toronto.
†Dalhousie University.

Nuclear Quadrupole Resonance at Low Frequency

Nuclear quadrupole resonances have been observed in spodumene ($LiAl(SiO_3)_2$) and in sodium thiosulphate ($Na_2S_2O_3.5H_2O$). For both materials, the resonance frequencies at zero magnetic field were in agreement with those predicted from high magnetic field measurements. The measurements to be reported here were obtained using single crystals of about 4 g. weight. A nuclear induction spectrometer was used, with magnetic modulation at 228 cycles per second, and with steady magnetic fields ranging from 0 to 30 gauss.

A quadrupole resonance, roughly 10 kc./sec. wide, was observed in sodium thiosulphate at a frequency of 1137±2 kc./sec. This result is in fair agreement with the measurements at high magnetic field reported by Itoh, Kusaka, and Yamagata (1954). The values of the nuclear quadrupole interaction constants obtained by these workers would lead to a nuclear quadrupole transition frequency of 1150±10 kc./sec. for Na^{23} in sodium thiosulphate.

Resonances in spodumene were observed at 751.5±2 kc./sec. and at 793.5±2 kc./sec., with zero applied d-c. magnetic field. These frequencies are in agreement with the nuclear quadrupole transition frequencies predicted for Al^{27} in spodumene (Lamarche and Volkoff 1953) from measurements at high magnetic fields (Petch, Cranna, and Volkoff 1953).

TABLE I

Comparison of measurements of the nuclear quadrupole coupling constants of Al^{27} in spodumene

	e^2qQ (Mc./sec.)	η
This work	2.965±0.010	0.933±0.008
Petch *et al.*	2.950±0.020	0.94 ±0.01

Using the measured pure quadrupole frequencies for spodumene, and the exact expression for the quadrupole energy levels of a spin 5/2 nucleus (Cohen 1954), it is possible to calculate values for the quadrupole coupling constant e^2qQ of Al^{27} in spodumene, and for η, the asymmetry parameter of the electrostatic field gradient, at the Al^{27} nucleus. In Table I, the values so calculated are compared with the results obtained from measurements at high magnetic field by Petch, Cranna, and Volkoff (1953).

The measurements in spodumene form part of an experimental study of nuclear resonances over a sufficiently wide range of magnetic field to link the pure quadrupole resonance spectrum with the Zeeman line split by quadrupole interactions. This work will be reported in greater detail at a later date.

Thanks are due to R. R. Haering, who suggested searching for the Na^{23} resonance in sodium thiosulphate. Support from the National Research Council, in the form of grants to Dr. G. M. Volkoff and studentships to the author in the years 1955–57, is gratefully acknowledged.

COHEN, M. H. 1954. Phys. Rev. **96**, 1278.
ITOH, J., KUSAKA, R., and YAMAGATA, Y. 1954. J. Phys. Soc. Japan, **9**, 209.
LAMARCHE, G. and VOLKOFF, G. M. 1953. Can. J. Phys. **31**, 1010.
PETCH, H. E., CRANNA, N. G., and VOLKOFF, G. M. 1953. Can. J. Phys. **31**, 837.

L. B. ROBINSON*

RECEIVED SEPTEMBER 9, 1957.
DEPARTMENT OF PHYSICS,
UNIVERSITY OF BRITISH COLUMBIA,
VANCOUVER, B.C.

*Now at Atomic Energy of Canada Ltd., Chalk River, Ont.

THE PHYSICAL SOCIETY

MEMBERSHIP of the Society is open to all who are interested in Physics.

FELLOWS pay an Entrance fee of £1 1*s*. ($3.00) and an Annual Subscription of £2 2*s*. ($6.00).

STUDENTS: A candidate for Studentship must be between the ages of 18 and 26, and pays an Annual Subscription of 5*s*. ($0.75).

MEETINGS: Fellows and Students may attend all Meetings of the Society including the annual Exhibition of Scientific Instruments and Apparatus.

PUBLICATIONS include the *Proceedings of the Physical Society*, published monthly in two sections, and *Reports on Progress in Physics*, published annually. Volume XIX, 1956, is now available (price 50*s*. ($7.15)). Members are entitled to receive any of the Publications at a reduced rate.

Further information can be obtained from:

THE PHYSICAL SOCIETY

1, LOWTHER GARDENS, PRINCE CONSORT ROAD

LONDON, S.W.7, ENGLAND

CANADIAN JOURNAL OF PHYSICS

Notes to Contributors

Manuscripts

(i) General. Manuscripts, in English or French, should be typewritten, double spaced, on paper 8½×11 in. **The original and one copy are to be submitted.** Tables and captions for the figures should be placed at the end of the manuscript. Every sheet of the manuscript should be numbered.

Style, arrangement, spelling, and abbreviations should conform to the usage of this journal. Names of all simple compounds, rather than their formulas, should be used in the text. Greek letters or unusual signs should be written plainly or explained by marginal notes. Superscripts and subscripts must be legible and carefully placed.

Manuscripts and illustrations should be carefully checked before they are submitted. Authors will be charged for unnecessary deviations from the usual format and for changes made in the proof that are considered excessive or unnecessary.

(ii) Abstract. An abstract of not more than about 200 words, indicating the scope of the work and the principal findings, is required, except in Notes.

(iii) References. References should be listed **alphabetically by authors' names,** unnumbered, and typed after the text. The form of the citations should be that used in current issues of this journal; in references to papers in periodicals, titles should not be given and only initial page numbers are required. The names of periodicals should be abbreviated in the form given in the most recent *List of Periodicals Abstracted by Chemical Abstracts*. All citations should be checked with the original articles and each one referred to in the text by the authors' names and the year.

(iv) Tables. Tables should be numbered in roman numerals and each table referred to in the text. Titles should always be given but should be brief; column headings should be brief and descriptive matter in the tables confined to a minimum. Vertical rules should be used only when they are essential. Numerous small tables should be avoided.

Illustrations

(i) General. All figures (including each figure of the plates) should be numbered consecutively from 1 up, in arabic numerals, and each figure referred to in the text. The author's name, title of the paper, and figure number should be written in the lower left corner of the sheets on which the illustrations appear. Captions should not be written on the illustrations (see Manuscripts (i)).

(ii) Line Drawings. Drawings should be carefully made with India ink on white drawing paper, blue tracing linen, or co-ordinate paper ruled in blue only; any co-ordinate lines that are to appear in the reproduction should be ruled in black ink. Paper ruled in green, yellow, or red should not be used unless it is desired to have all the co-ordinate lines show. All lines should be of sufficient thickness to reproduce well. Decimal points, periods, and stippled dots should be solid black circles large enough to be reduced if necessary. Letters and numerals should be neatly made, preferably with a stencil (**do NOT use typewriting**) and be of such size that the smallest lettering will be not less than 1 mm. high when reproduced in a cut 3 in. wide.

Many drawings are made too large; originals should not be more than 2 or 3 times the size of the desired reproduction. In large drawings or groups of drawings the ratio of height to width should conform to that of a journal page but the height should be adjusted to make allowance for the caption.

The original drawings and one set of clear copies (e.g. small photographs) are to be submitted.

(iii) Photographs. Prints should be made on glossy paper, with strong contrasts. They should be trimmed so that essential features only are shown and mounted carefully, with rubber cement, on white cardboard with no space or only a **very** small space (less than 1 mm.) between them. In mounting, full use of the space available should be made (to reduce the number of cuts required) and the ratio of height to width should correspond to that of a journal page (4⅜×7½ in.); however, allowance must be made for the captions. Photographs or groups of photographs should not be more than 2 or 3 times the size of the desired reproduction.

Photographs are to be submitted in duplicate; if they are to be reproduced in groups one set should be mounted, the duplicate set unmounted.

Reprints

A total of 50 reprints of each paper, without covers, are supplied free. Additional reprints, with or without covers, may be purchased.

Charges for reprints are based on the number of printed pages, which may be calculated approximately by multiplying by 0.6 the number of manuscript pages (double-spaced typewritten sheets, 8½×11 in.) and including the space occupied by illustrations. An additional charge is made for illustrations that appear as coated inserts. The cost per page is given on the reprint requisition which accompanies the galley.

Any reprints required in addition to those requested on the author's reprint requisition form must be ordered officially as soon as the paper has been accepted for publication.

Contents

Printed in Canada *by* University of Toronto Press